Geochemical and Petrological Interpretation of Mantle Structure Beneath the Southwest Slave Province, NWT

by

Gary Brent Carbno
B.Sc., Concordia University, 1997

A Thesis Submitted in Partial Fulfillment of the
Requirements for the Degree of

MASTER OF SCIENCE

In the School of Earth and Ocean Sciences

We accept this thesis as conforming
to the required standard

[redacted]

Dr. D. Canil, Supervisor (School of Earth and Ocean Sciences)

[redacted]

Dr. K. Gillis, Internal Member (School of Earth and Ocean Sciences)

[redacted]

Dr. S.T. Johnston, Internal Member (School of Earth and Ocean Sciences)

[redacted]

Dr. A. Irving, External Examiner (Department of Geological Sciences, University of Washington)

© Gary Brent Carbno, 2000

University of Victoria

All rights reserved. This thesis may not be reproduced in whole or in part, by photocopy or other means, without the permission of the author.

Supervisor: Dr. Dante Canil

ABSTRACT

The Drybones Bay kimberlite has offered an opportunity to compare geophysical observations of the mantle lithosphere beneath the southwest Slave craton with geochemical and petrological interpretations through mantle xenoliths and xenocrysts. Coarse-textured garnet and spinel-garnet peridotite xenoliths, and garnet and garnet-clinopyroxene xenocrysts were analyzed for a suite of trace elements. The Ni-in-garnet geothermometer (Canil, 1999) yielded equilibration temperatures between 850-1200 °C, and corresponding depths of 90-160 km, assuming a 41mWm^{-2} paleogeotherm. This method estimates the thickness of the southwest Slave craton in the Ordovician at approximately 160 km, within the stability field of diamond. Trace element analysis revealed a distinct geochemical anomaly at a depth of approximately 120 km, which marks the transition from wehrlite to metasomatized wehrlite and lherzolite. This anomalous depth has been observed in geophysical studies, and has been interpreted as a structural discontinuity.

Examiners:

[redacted]

Dr. D. Canil, Supervisor (School of Earth and Ocean Sciences)

[redacted]

Dr. K. Gillis, Internal Member (School of Earth and Ocean Sciences)

[redacted]

Dr. S.T. Johnston, Internal Member (School of Earth and Ocean Sciences)

[redacted]

Dr. A. Irving, External Examiner (Department of Geological Sciences, University of Washington)

TABLE OF CONTENTS

ABSTRACT ..... **II**

LIST OF FIGURES ..... **VI**

ACKNOWLEDGEMENTS ..... **VII**

CHAPTER 1 ..... **1**

1.1 The Mantle 1
1.2 Kimberlites 2
1.2.1 Textural Genetic Classification *4*
1.2.2 Kimberlite Origin and Emplacement *7*
1.3 Xenoliths 9
1.4 Indicator Minerals and Diamond Exploration 12
1.5 Thesis Outline 16

CHAPTER 2 ..... **17**

2.1 The Slave Province 17
2.2 Slave Kimberlites 20
2.3 The Drybones Bay Kimberlite 21

CHAPTER 3 ..... **23**

3.1 Samples 23
3.2 Xenolith Petrography 24
3.2.1 Garnet Peridotites *26*
3.2.2 Spinel-Garnet Peridotites *30*
3.2.3 Spinel Peridotite *31*
3.3 Modal Mineralogy 31
3.4 Heavy Mineral Concentrate 35
3.5 Summary 39

CHAPTER 4 ..... **40**

4.1 Major Element Geochemistry 40
4.1.1 Garnet *40*
4.2 Trace Element Geochemistry 44
4.2.1 Garnet *44*
4.2.2 Clinopyroxene *46*
4.3 Summary 46

CHAPTER 5 ..... **48**

5.1 Geothermobarometers 48
5.2 Temperature Calculations 51

5.4 Depth Estimates 55
5.5 Independent Pressure Estimates 59
5.6 Summary 61

CHAPTER 6 62

6.1 Cratonic Evolution 62
6.2 Lithospheric Geometry and Thickness 63
6.3 Trace Element Systematics In Garnet 65
6.4 Carbonatite Metasomatism 71
6.5 Mantle Lithosphere Structure 74
6.6 Summary 84

CHAPTER 7 86

7.1 Lithosphere Thickness 86
7.2 Lithospheric Mantle Structure 87
7.3 Future Work 88

REFERENCES 89

APPENDIX A 96

APPENDIX B 97

APPENDIX C 98

APPENDIX D 106

APPENDIX E 112

APPENDIX F 114

APPENDIX G 116

LIST OF FIGURES

FIGURE 1.1 IDEALIZED SECTION THROUGH A KIMBERLITE. 5
FIGURE 1.2 IMPORTANT LOCATIONS IN THE SLAVE PROVINCE. 11
FIGURE 1.3 $CaO - Cr_2O_3$ CLASSIFICATION OF GARNET 14

FIGURE 2.1 GEOLOGICAL AND TECTONIC MAP OF THE SLAVE PROVINCE. 18

FIGURE 3.1 PHOTOMICROGRAPH OF COURSE TEXTURED PERIDOTITE 25
FIGURE 3.2 PHOTOMICROGRAPH OF SPINEL-GARNET PERIDOTITE 27
FIGURE 3.3 PHOTOMICROGRAPH OF INTENSELY ALTERED PERIDOTITE. 28
FIGURE 3.4 PHOTOMICROGRAPH OF GARNET GRAINS WITH KELYPHITE. 29
FIGURE 3.5 PLOT OF XENOLITH SIZE AGAINST MODAL ABUNDANCES. 32
FIGURE 3.6 PHOTOGRAPH OF PERIDOTITE XENOLITH WITH SPATIAL ASSOCIATION. 33
FIGURE 3.7 PHOTOGRAPH SHOWING DEGREES OF SPHERICITY. 36
FIGURE 3.8 PHOTOGRAPH SHOWING RANGE IN GARNET COLOURS. 37
FIGURE 3.9 PHOTOGRAPH OF GARNET-CLINOPYROXENE PAIR. 38

FIGURE 4.1 PLOT OF CaO AND Cr_2O_3 COMPOSITIONS IN GARNETS. 41
FIGURE 4.2 PLOT OF COLOUR NUMBER AGAINST OXIDE WEIGHT PERCENT 43
FIGURE 4.3 CHONDRITE NORMALIZED GARNET PATTERNS. 45
FIGURE 4.4 PRIMITIVE MANTLE NORMALIZED CLINOPYROXENE PATTERNS. 47

FIGURE 5.1 Ni-IN-GARNET GEOTHERMOMETER CALIBRATIONS. 52
FIGURE 5.2 P-T ARRAY FOR DRYBONES GARNETS 54
FIGURE 5.3 CENTRAL SLAVE GEOTHERMS. 56
FIGURE 5.4 TEMPERATURE RANGE FOR T_{Ni} CALIBRATIONS 58
FIGURE 5. 5 PLOT OF T_{Ni} IN VS P_{Ca} 60

FIGURE 6.1 $D^{GT/CPX}$ VALUES FOR DRYBONES BAY GARNETS 67
FIGURE 6.2 RANGE OF CHONDRITE NORMALIZED REE PATTERNS. 69
FIGURE 6. 3 TRACE ELEMENT RATIOS AGAINST DEPTH. 75
FIGURE 6. 4 TRACE ELEMENT RATIOS USING EMPIRICAL TEMPERATURE CALCULATION. . 76
FIGURE 6. 5. GEOPHYSICAL SECTION OF SOUTHWEST SLAVE PROVINCE. 77
FIGURE 6. 6 PLOT OF YB/GA RATIO AGAINST GARNET/CLINOPYROXENE RATIO. 80
FIGURE 6. 7 PLOT OF CA VERSUS CR CATIONS. 82

FIGURE G.1 SAMPLE OUTPUT OF LAM-ICP-MS 120
FIGURE G.2 DETECTION LIMITS FOR NIST 613 121
FIGURE G.3 NI CONCENTRATIONS OVER TIME FOR NIST 613 124
FIGURE G.4 MEASURED AND KNOWN ELEMENT VALUES FOR NIST 613. 125

ACKNOWLEDGEMENTS

I would like to thank Dr. Dante Canil for his patience and guidance on an academic level, and for all of this and more on a personal level. It was a rough road at times, but I made it – maybe someday I'll truly understand thermodynamics. I must also thank U. Kretschmar and D. Smith for access to drill core, and M. Raudsepp (University of British Columbia) and L. Shi (University of Alberta) for providing assistance with microprobe work. Thanks also to X. Chen for his many hours of help with the LAM-ICP-MS analyses, Michelle for help with sample preparation, and Roberta for sample analysis. Thanks to Kendrick for his humor and many free meals in Sudbury, to Lisa for her help with Word, and to Jason and Neil for continually reminding me not to give up – Neil, remember to keep your stick down. I must thank my parents for their limitless support and for believing whatever decision I make is always the right one. Lastly, I would like to give special thanks to Joanne for her love and confidence in me. Through everything that has happened, you still think I am one of the smartest people you know.

CHAPTER 1
INTRODUCTION

1.1 The Mantle

The Earth's major chemical reservoirs can be divided into the atmosphere, hydrosphere, crust, mantle (upper and lower) and core. The mantle is the largest single reservoir and constitutes over 99% of the mass of the silicate Earth, with the remaining 1% of the silicate mass being found in the crust. Most of our knowledge of the mantle has been deduced indirectly from geophysical properties such as heat flow, density and seismic velocity. However, large pieces of the mantle do appear at the surface in alpine massifs and ophiolites that include samples from the lithospheric mantle. Smaller pieces of the mantle lithosphere can also be brought to the surface as xenoliths by the ascent of volcanic rocks such as basalts and kimberlites. These "pieces" of the mantle allow for the geochemical study of lithosphere that could not otherwise be attained by mechanical (i.e. drill holes) or remote methods. Kimberlite xenoliths are of particular interest because they sometimes sample the mantle from mantle lithosphere that may contain diamonds.

Geochemical and geophysical studies of the lithosphere have led to the conclusion that the upper mantle is chemically homogeneous. Processes of

differentiation and partial melting have led to heterogeneity on more local scales. Events such as crust formation have not greatly affected major element compositions of the mantle because the crust is volumetrically small, even though local small-scale changes can be seen due to partial melting. This heterogeneity and local variability is best indicated in the upper mantle (lithospheric mantle) by trace elements that show a much larger variation than major elements due to extreme variations in compatibility in partial melting processes. On average the lithospheric mantle is believed to be peridotitic in composition, with lherzolite being dominant. Meteorites (chondrites) are also used to restrict the composition of the mantle since they are believed to represent the overall composition of the primitive mantle before differentiation.

Cratonic lithosphere is that which underlies cratons, and includes mantle that is relatively cold and thick in comparison to mantle lithosphere beneath ocean basins or orogenic belts. This mantle 'root' or 'keel' extends to depths as great as 200 km. The presence of a mantle root makes cratons unique, and is also required for the formation and stable storage of diamonds.

1.2 Kimberlites

Kimberlites are a major source of crustal and mantle xenoliths, especially in Archean cratons where major volcanic activity has been extinct for billions of years. Kimberlites are a unique type of volcanic igneous rock that originate from great depths in the mantle. The petrologic description of a kimberlite is not straightforward because they have such complex mineralogy and chemistry (Woolley et al, 1996), and because the exact origin and mechanism of kimberlite emplacement is not well understood.

However, because of their complexity, kimberlites have been classified into two separate types, Group I and Group II kimberlites (Mitchell, 1995; Mitchell, 1986). Group I kimberlites correspond to a description by Wagner (1914) of archetypal rocks from Kimberley, South Africa, which were formerly termed "basaltic kimberlites", and Group II kimberlites correspond to "micaceous" or "lamprophyric kimberlites" (Woolley et al, 1996).

Group I kimberlites are described as "volatile-rich (dominantly CO_2) potassic ultrabasic rocks commonly exhibiting a distinctive inequigranular texture resulting from the presence of macrocrysts and, in some cases, megacrysts set in a fine-grained matrix" (Mitchell, 1995). Macrocrysts and megacrysts, some of which are xenocrystic, typically include anhedral olivine, a characteristic and dominant constituent, as well as ilmenite, pyrope, diopside, phlogopite, enstatite and Ti-poor chromite (Woolley et al, 1996). The matrix contains a second generation of primary olivine, which can occur with all or some of the following primary minerals: monticellite, phlogopite, perovskite, spinel (magnesian ulvöspinel – magnesiochromite – ulvöspinel – magnetite), apatite, carbonate and serpentine (Woolley et al, 1996). The replacement of earlier-formed olivine, phlogopite, monticellite and apatite by deuteric serpentine and calcite is common, along with Ni-sulfides and rutile as accessory minerals (Woolley et al, 1996). Of course diamonds should be included in this category as they can occur as macrocrysts in the kimberlite, as well as inclusions in xenoliths.

Group II kimberlites, sometimes termed orangeites, belong to " a clan of ultrapotassic, peralkaline rocks rich in volatiles (dominantly H_2O), characterized by phlogopite macrocrysts and microphenocrysts, together with groundmass micas that

vary in composition from phlogopite to tetraferriphlogopite" (Mitchell, 1995). The macrocrysts consist of rounded olivine grains and euhedral primary crystals of olivine, but these are not invariably major constituents (Woolley et al, 1996). Primary phases include diopside, spinel (Mg-chromite to Ti-magnetite), perovskite, apatite and other phosphates, rutile and ilmenite (Woolley et al, 1996). The matrix may contain calcite, dolomite, ancylite, witherite, norsethite and serpentine. The groundmass may also contain sanadine and K-richterite, with barite as a common deuteric secondary mineral (Woolley et al, 1996).

1.2.1 Textural Genetic Classification

Kimberlites are also classified based on their genetic relationship during pipe emplacement. This classification recognizes three different kimberlite *facies*, which reflect the formation of the rocks under differing magmatic or volcanic conditions according to a model of a kimberlite magmatic system described by Mitchell (1986). These three facies are termed crater facies, diatreme facies, and hypabyssal facies kimberlites (Figure 1.1).

Crater facies kimberlites occur near the surface of a kimberlitic eruption (subaerial), where the higher levels of emplacement are quite explosive (Figure 1.1) and surface materials are often incorporated. Crater facies rocks are divided into lavas, epiclastic and pyroclastic types, with further subdivisions made according to sedimentological or volcanological particle size terminology (Mitchell, 1986). Unfortunately a record of subaerial effusive activity has only been preserved in a few areas where erosion has been minor (Mitchell, 1986), and therefore many deposits

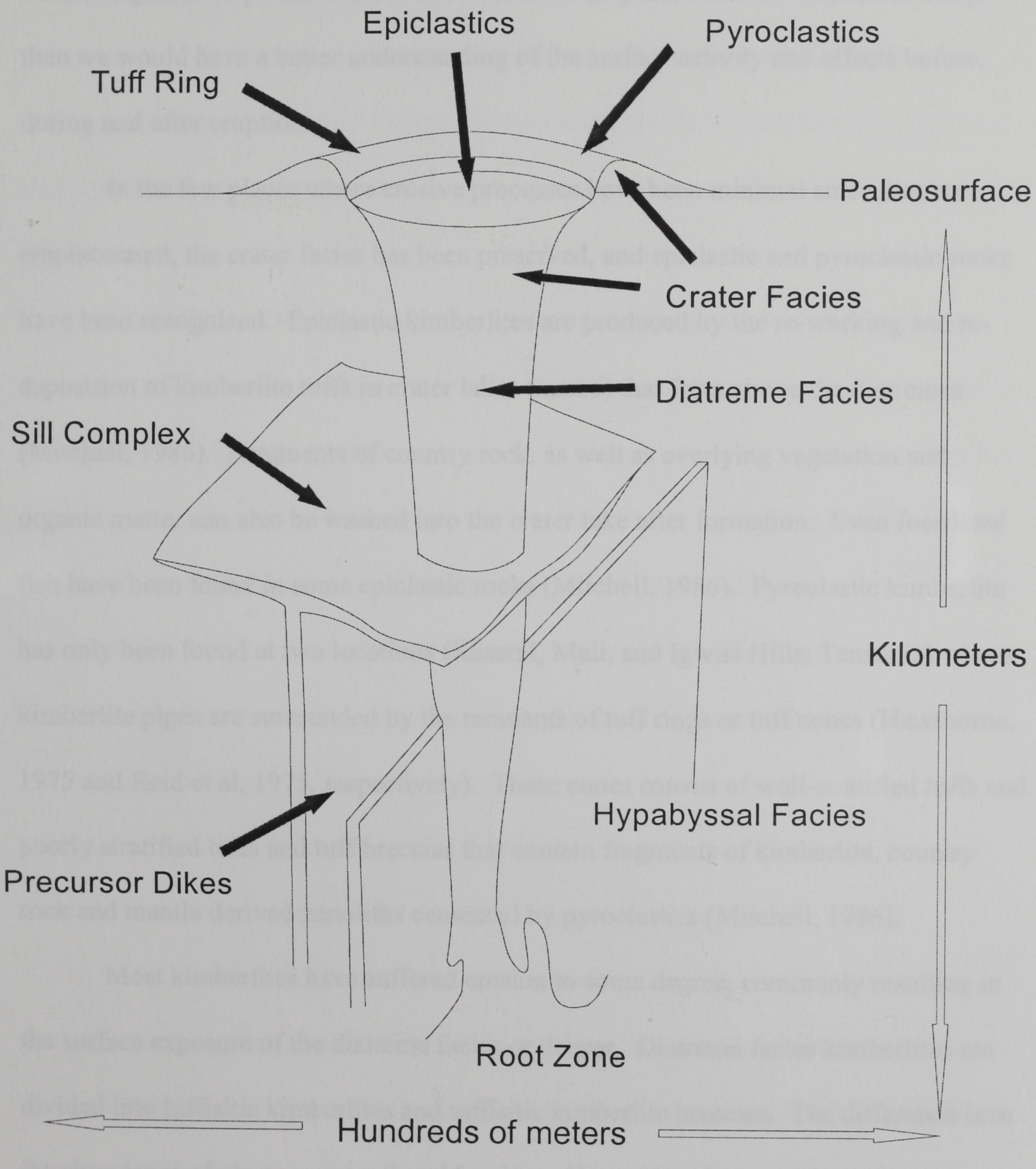

Figure 1.1: Idealized section through a kimberlite prior to surficial erosional processes (adapted from Mitchell, 1986).

cannot be adequately studied for crater facies rocks. For this reason no true lava has been recognized or preserved, and if a kimberlite eruption could be witnessed today, then we would have a better understanding of the surface activity and effects before, during and after eruption.

In the few places where erosive processes have been minimal since diatreme emplacement, the crater facies has been preserved, and epiclastic and pyroclastic rocks have been recognized. Epiclastic kimberlites are produced by the re-working and re-deposition of kimberlite tuffs in crater lakes (maars) that form above the diatremes (Mitchell, 1986). Fragments of country rock, as well as overlying vegetation and organic matter can also be washed into the crater lake after formation. Even fossilized fish have been found in some epiclastic rocks (Mitchell, 1986). Pyroclastic kimberlite has only been found at two locations (Kasami, Mali, and Igwisi Hills, Tanzania) where kimberlite pipes are surrounded by the remnants of tuff rings or tuff cones (Hawthorne, 1975 and Reid et al, 1975, respectively). These cones consist of well-stratified tuffs and poorly stratified tuffs and tuff breccias that contain fragments of kimberlite, country rock and mantle derived xenoliths cemented by pyroclastics (Mitchell, 1986).

Most kimberlites have suffered erosion to some degree, commonly resulting in the surface exposure of the diatreme facies or deeper. Diatreme facies kimberlites are divided into tuffisitic kimberlites and tuffisitic kimberlite breccias. The difference is in the abundance of clasts, greater than 15 volume % marking the transition to breccia (Mitchell, 1986). The term tuffisitic is used because these rocks are considered to consist of intrusive pyroclastics, but are perhaps better termed volcanoclastic. Tuffisitic kimberlite breccias are the most common rocks in kimberlite diatremes and contain

abundant angular to rounded country rock inclusions, autolithic clasts of earlier hypabyssal kimberlite, and discrete and fractured grains of olivine, garnet and ilmenite (Mitchell, 1986). The primary matrix material consists of microcrystalline diopside, serpentine, and rarely primary calcite. However, the matrix is extremely susceptible to alteration and is typically replaced by clay minerals and secondary calcite (Mitchell, 1986).

Hypabyssal kimberlites have formed by the crystallization of a volatile-rich kimberlite magma, and consequently, they exhibit igneous textures and show the effects of magmatic differentiation (Mitchell, 1986). In the instance of hypabyssal kimberlites, a significant quantity of country rock xenoliths warrants the use of the term kimberlite breccia for this type. However, the mineralogical definitions of kimberlite mentioned previously in this section would best describe the host hypabyssal kimberlite. Finally, hypabyssal kimberlite forms the root zones of diatremes and occurs as dikes and sills. The root zones of kimberlites comprise the bulk of occurrences in many kimberlite provinces because of the depth of erosion and the removal of the diatreme and crater facies kimberlite (Mitchell, 1986).

1.2.2 Kimberlite Origin and Emplacement

There is, at present, still much debate over the origin of kimberlites beneath the lithosphere. Ringwood et al (1992) believe that the source of kimberlite magma lies in the transition zone, in a boundary layer composed of subducted harzburgite and aesthenospheric pyrolite. Furthermore, they believe there is a genetic relationship between kimberlites and Ocean Island Basalts (OIB), both interpreted to result from a

small degree of partial melting of the source region caused by the subduction of oceanic lithosphere. The notion that the source region for kimberlite magma is located around the transition zone seems well accepted.

An alternative theory is that there is a connection between and among the core, geomagnetism, plumes and diamonds (Haggerty, 1994). Haggerty (1994) believes that kimberlites are recorders of plumes, and the kimberlite source region is also close to the transition zone. Furthermore, Haggerty (1994) states that deep-focus volcanism with a core-mantle boundary source may be triggered on a global scale, which results in distinct aberrations in the geomagnetic field.

Controversy in theory revolves more around the "driving force" of the kimberlite magmatism rather than its source region. Therefore a geologically sound explanation for why a kimberlite will erupt from such depths, and in the middle of a tectonically stable craton, is not easy to produce. Girnis et al (1995) state that Group 1A (magnesian basaltic) kimberlites are formed through the interaction of deep-seated melts from the aesthenosphere or transition zone with strongly depleted harzburgites at the base of the continental lithosphere. This results in the enrichment in CO_2 to a saturation level, and upon reaching saturation, the separation of a CO_2-rich fluid triggers kimberlite eruption before complete equilibration with the enclosing peridotite (Girnis et al, 1995). This can explain properties of kimberlites such as their rapid ascent, small volume, and isotopic signatures similar to OIB, while others may not sufficiently address all of these concerns.

1.3 Xenoliths

Xenoliths are pieces or fragments of wall rock that are accidentally incorporated into an ascending magma. As was mentioned previously, mantle xenoliths allow us the opportunity to study the geochemistry of the mantle by analyzing mantle samples rather than interpreting geophysical properties. If these xenoliths remain intact during their journey to the surface they can reveal characteristics of the region from which they were derived before being transported. The mineralogy of the xenoliths can tell us about the composition of the mantle from which they originated, and the chemistry of individual phases can reveal the temperature and pressure conditions under which the assemblage equilibrated.

An ascending magma may pass through numerous lithologies on its path to the surface, but the magma may not necessarily incorporate xenoliths from every lithology that is traversed. For example, xenoliths determined to be from the deepest region of the mantle that the ascending magma has traversed can only be interpreted as a minimum depth of sampling. The lithosphere could likely exist to greater depths, but the samples may not have survived the ascent, or were never incorporated in the ascending magma.

If magma, such as kimberlite, originates below and passes through a portion of the mantle that contains diamonds, then these diamonds can become entrained in the kimberlite as xenoliths or xenocrysts and brought to the surface. The prospect of diamonds reaching the surface via an ascending magma has made available many xenolith samples worldwide since exploration for diamonds involves the analysis of associated xenoliths found in rocks such as kimberlites.

Information gained from xenoliths can be directly compared to geophysical results in order to verify and explain interpretations that could not otherwise be "ground-truthed". There are few localities where deep lithosphere geophysical studies have direct geochemical evidence with which to compare results, and the Drybones Bay kimberlite is one of them. With this comparison the geophysically interpreted lithological and seismic properties can be attached to a real lithological unit, and then possibly discontinuities and other mantle features can be better defined. All of this can be assembled in a much bigger picture to better understand lithospheric evolution beneath cratons, as well as the development of younger crustal and mantle features.

Kimberlite-hosted xenoliths have been studied from cratons worldwide, with a vast number of studies concentrated in traditional diamond producing cratons such as South Africa (Kaapvaal craton) and Siberia. Until recently, kimberlite provinces in North America have had less attention because there are few economically significant kimberlite pipes. The discovery of significant diamondiferous kimberlites in the Lac de Gras region of the Slave craton (see Figure 1.2) in 1991 resulted in the availability of many more xenoliths for study in this region. Xenolith studies undertaken in the central portion of the Slave craton (Kopylova et al, 1998; MacKenzie and Canil, 1999; Boyd and Canil, 1997) have resulted in a better understanding of the characteristics and evolution of the Slave lithosphere. These localities are, however, far removed from seismic and electromagnetic studies on the Slave craton, with which petrological evidence can be compared. Seismic reflection surveys from LITHOPROBE Transect 1 (Cook et al, 1998), detailed electromagnetic surveys (Jones

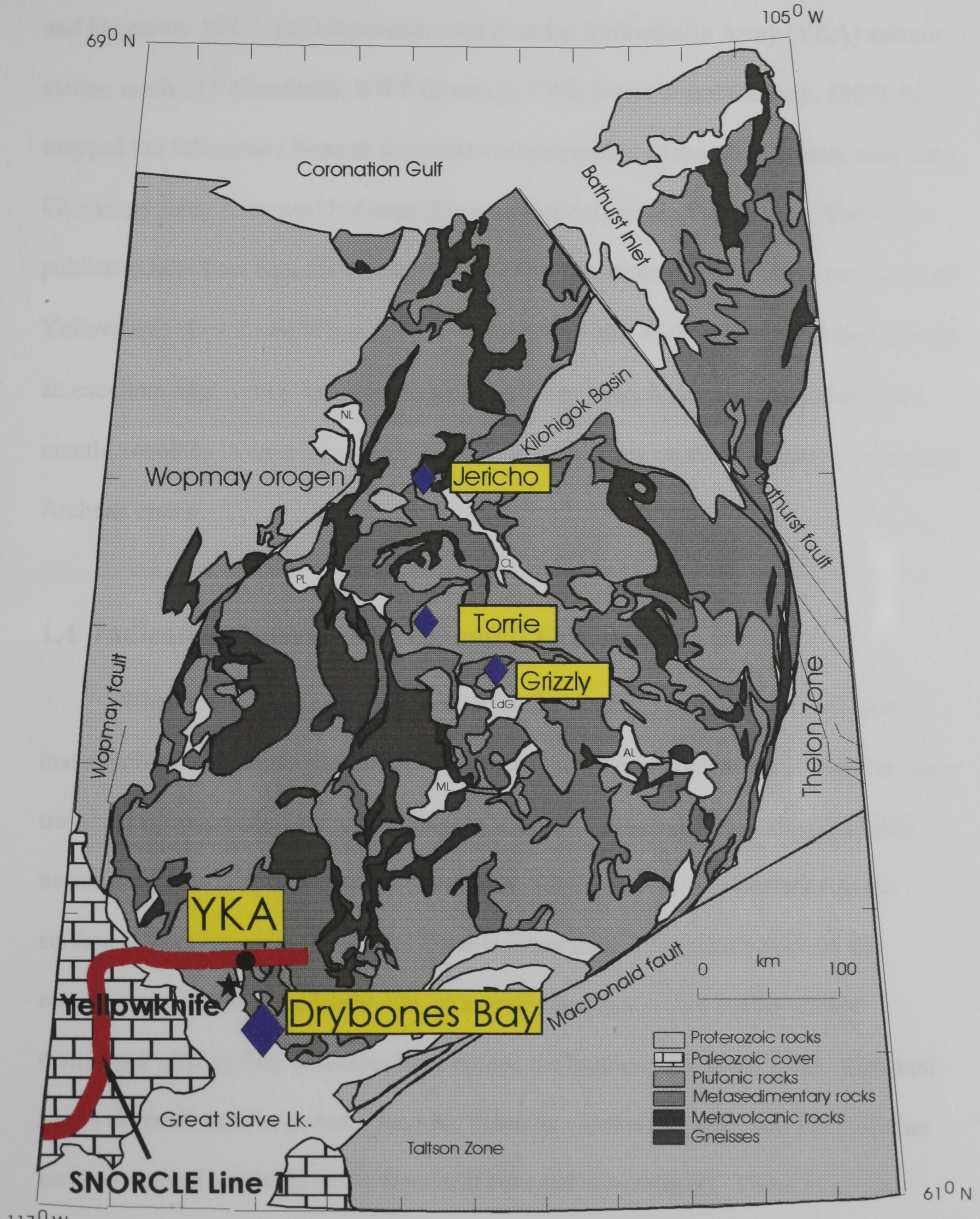

Figure 1.2: Map of the Slave Province, NWT, Canada showing the location of the Drybones Bay kimberlite, as well as the YKA seismic station, SNORCLE Transect Line 1, and other kimberlite study locations in the central Slave Province (adapted from Pell, 1997).

and Ferguson, 1997), and teleseismic studies at the Yellowknife Array (YKA) seismic station north of Yellowknife, NWT (Bostock, 1998; Bostock and Cassidy, 1997), have mapped the lithosphere beneath the southwestern portion of the Slave craton, only fifty kilometers away from the Drybones Bay kimberlite pipe (see Figure 1.2). The only published heat flow data for the Slave province was measured sixty kilometers north of Yellowknife (Lewis and Wang, 1992). Unique locations such as Drybones Bay provide an excellent opportunity to compare petrological and geochemical information from mantle xenoliths to an array of geophysical measurements on the lithosphere beneath an Archean craton.

1.4 Indicator Minerals and Diamond Exploration

When kimberlites are being prospected for diamond potential, the information that xenoliths and xenocrysts can provide about the lithosphere that the kimberlites have traversed is invaluable. Frequently there is a paucity of valuable xenoliths, possibly because of alteration, or because the xenoliths did not survive transportation to the surface. However, more resistant or durable minerals will frequently survive and remain intact either in the kimberlite, or as individual grains that can be widely distributed after surface processes have eroded the kimberlite to some level. Resistant heavy minerals such as garnet, chromite, ilmenite, chrome diopside, and often olivine can be removed relatively easily from drill core and concentrated. These minerals, being more resistant, can also be found at some distance from their source kimberlite on the surface. Surface sampling techniques include media from stream sediments, eskers, basal tills, and soils or deflation surfaces (loaming). Fipke et al (1995) incorporated

such exploration techniques with outstanding success – the discovery of a world class kimberlite province in Canada's Northwest Territories, and the subsequent opening of the Ekati Diamond Mine (operated by BHP Diamonds Inc.).

Of the resistant heavy minerals mentioned, garnet is the most common and abundant mineral that is found in drill concentrate or surface sample concentrates. These garnets can be xenocrysts or fragments from xenoliths, sometimes possessing kelyphite rims. Garnets are very useful as indicator minerals for diamond exploration because their major element chemistry can give information about their provenance.

Lherzolitic garnets are the most common type of garnet found in kimberlite. Since statistically garnet lherzolite is not a major component of a diamond inclusion suite (garnets or other minerals found as inclusions in the actual diamonds) at any locality yet described, they must be distinguished from those garnets which are more prospective for diamonds, such as harzburgitic garnets (Fipke et al, 1995). A plot of CaO versus Cr_2O_3 for peridotitic garnets can be used to distinguish less prospective lherzolitic garnets from more prospective harzburgitic garnets (Figure 1.3). A line has been drawn on this plot (Figure 1.3) that distinguishes 85 % of diamond inclusion garnets (harzburgitic) from lherzolitic garnets (Gurney, 1984). Diamond inclusion garnets plot on the sub-calcic side (G10) of the line, while lherzolitic garnets plot in the calcic (G9) field, after the classification scheme of Dawson and Stephens (1975).

Therefore, on the basis of the Ca and Cr content of individual garnet grains, one can make an early stage determination whether a given kimberlite has high diamond potential.

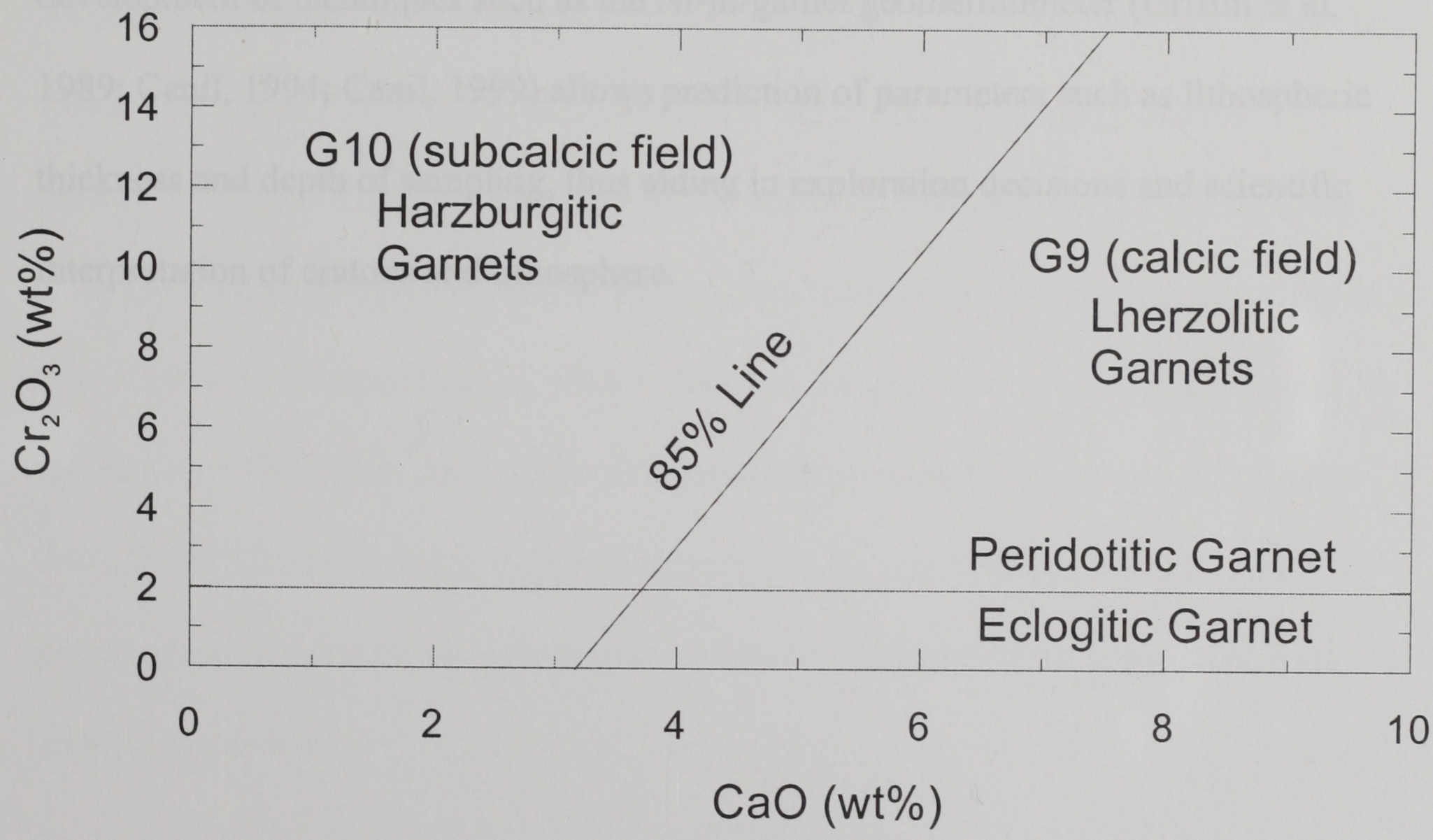

Figure 1.3. Field plot showing the classification of garnet based on the CaO-Cr_2O_3 composition of peridotitic garnets (after Gurney, 1984). The 85% Line distinguishes subcalcic (G10) garnet from calcic (G9) garnet. The horizontal line drawn at 2 wt% Cr_2O_3 is used as an arbitrary division between eclogitic and peridotitic garnets.

Garnets are major hosts for trace elements. Therefore they can give us information regarding events in their source region that is not recorded by major elements which are less sensitive in recording such events. Trace element concentrations in garnet can be used to distinguish metasomatic events and to distinguish subtle lithological changes in the mantle source region. Furthermore, the development of techniques such as the Ni-in-garnet geothermometer (Griffin et al, 1989; Canil, 1994; Canil, 1999) allows prediction of parameters such as lithospheric thickness and depth of sampling, thus aiding in exploration decisions and scientific interpretation of cratons and lithosphere.

1.5 Thesis Outline

In this thesis the textures and modal mineralogy of peridotite xenoliths from the Drybones Bay kimberlite are described. The major and trace element geochemistry of peridotitic garnets in xenoliths and heavy mineral concentrate. Garnets were chosen as a focus of this study because pristine garnet is present in the Drybones Bay kimberlite, unlike other primary phases that have been carbonatized and serpentinized. From the garnet chemistry, lithospheric thickness and a "structure/stratigraphy" can be determined, and compared with teleseismic, seismic reflection and geothermal data from the southwest Slave Province. In addition, the protolith and processes involved in the formation of lithosphere are made evident in the geochemical patterns recorded by the garnets. These data furnish robust constraints on models of cratonic lithosphere beneath the Slave Province, and provide the basis for one of the first comparisons of geophysical interpretations with petrological interpretations of the lithosphere beneath an Archean craton.

CHAPTER 2

GEOLOGY

2.1 The Slave Province

The Slave Province is an Archean craton in the Northwest Territories, Canada with a surface area of ~ 213 000 km^2, consisting of granite, gneiss and supracrustal rocks (Figure 2.1). The western part of the Slave Province contains some of the oldest rocks in the world – the 3.96 Ga Acasta gneiss (Bowring et al, 1990). The supracrustal sequences are dominated by 2.71-2.61 Ga metasedimentary and lesser metavolcanic rocks of the Yellowknife Supergroup (Pell, 1995). This high proportion of metasedimentary rocks distinguishes the Slave craton from most other cratons worldwide. All of the supracrustal rocks in the Slave craton, which make it unique, have been metamorphosed at greenschist to lower amphibolite facies (Isachsen and Bowring, 1994).

The oldest sedimentary rocks found in the Slave are quartz arenites occurring only in the western part of the craton. These old sediments were derived from, and deposited on, a stable shelf (Padgham and Fyson, 1992) in association with banded iron formations, and overlain by felsic volcanics. The most widespread unit,

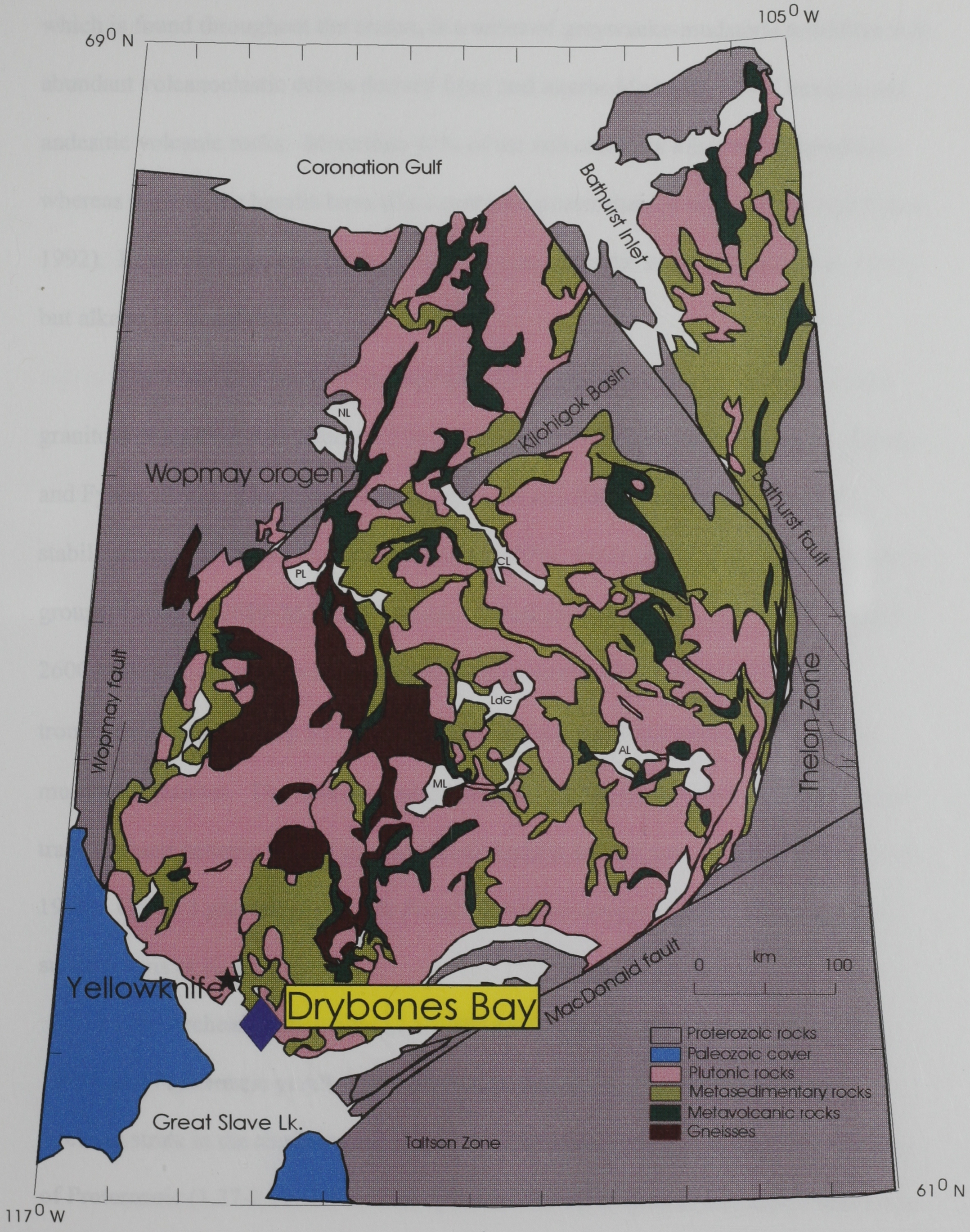

Figure 2.1: Geological and tectonic map of the Slave Province, NWT, Canada. The location of the Drybones Bay kimberlite is designated by the blue diamond. (Adapted from Pell, 1997)

which is found throughout the craton, is a series of greywacke-mudstone turbidites with abundant volcanoclastic debris derived from and interbedded with felsic, basaltic and andesitic volcanic rocks. More than 45% of the volcanics are felsic to intermediate, whereas most of the basalts have silica contents greater than 50% (Padgham and Fyson, 1992). Komatiites can also be found and are present in the south (Bleeker et al, 1999), but alkalic lavas are rare.

The Slave Province also contains several generations of syn- to post volcanic granitoid complexes and plutons (2.58-2.7 Ga) that cover 65% of the craton (Padgham and Fyson, 1992). The intrusion of voluminous plutonic rocks marked the final stabilization of the Slave craton. Davis et al (1994) divide the plutonic rocks into three groups; Group 1 (2689-2650 Ma) includes trondhjemites and diorites; Group 2 (2610-2600 Ma) includes syn- to late deformational monzodiorite-granodiorite and trondhjemites; and Group 3 (2599-2580 Ma) includes post-deformational biotite ± muscovite granites. The Group 1 and 2 plutonics are generally calc-alkaline and have trace element patterns similar to modern subduction related igneous suites (Davis et al, 1994). Group 3 plutonics resemble Phanerozoic post-orogenic K-U-Th rich granite suites (Davis et al, 1994).

Late Archean carbonatites (2.6-2.59 Ga) are known from two localities (Pell, 1997), and Proterozoic peralkaline carbonatite-related complexes have intruded Archean strata in the southwestern part of the Slave (Pell, 1997). At least five swarms of Proterozoic (1.27-2.23 Ga) diabase dykes cut the older units in the central Slave near Lac de Gras. Other dyke swarms, not yet dated, intrude the southwest part of the Slave, and two younger sets of dykes associated with the 0.78 Ga Gunbarrel and 0.72 Ga

Franklin magmatic events penetrate the northern and western margin of the craton (Pell, 1997).

The Slave Structural Province is a small Archean nucleus within the larger North American craton. The Slave is bounded on the east by the Thelon Orogen (2.2 Ga), and on the west by the Wopmay Orogen (1.9-2.1 Ga), a series of magmatic arcs and accreted terranes (Figure 2.1). The overlapping Proterozoic and younger supracrustal rocks of the Bear Province and the Arctic Platform define the northern boundary of the Slave. Proterozoic sediments also overlap the craton along its northeast side along the Bathurst Fault, and extend partway across the craton in a narrow northeast trending belt (Padgham and Fyson, 1992). The southern boundary of the Slave is the Great Slave Lake Shear Zone, which is an ancient (1.8-2.0 Ga) continental transform that juxtaposes Archean rocks of the Slave against Proterozoic rocks of the Churchill Province (Figure 2.1).

2.2 Slave Kimberlites

The recent "diamond rush" in the Canadian North has resulted in the discovery of more than 150 kimberlites in the Archean Slave Province since 1991 (Fipke et al. 1995). There are several generations of kimberlites located in the Slave ranging in age from Cambrian to Tertiary (Pell, 1997), and many of the kimberlites host mantle xenoliths. Xenolith studies from kimberlites in the Slave Province (Figure 1.2) have been published mainly from kimberlites within the central part of the province (MacKenzie and Canil, 1999; Kopylova et al. 1999; Boyd and Canil, 1997; Griffin et al, 1999a), and confirm the existence of a deep mantle root beneath this area of the craton.

2.3 The Drybones Bay Kimberlite

The Drybones Bay kimberlite pipe is located beneath Drybones Bay on the north shore of Great Slave Lake at the southwestern edge of the Slave Craton (Figure 1.2, 62°15'N, 114°00'W). The Drybones Bay kimberlite pipe (900m by 400m) is the largest kimberlite pipe found to date in the Northwest Territories (Kretschmar, 1997). This pipe has been dated at 442-485 Ma (Pell, 1997) using U-Pb in zircons (Heaman et al, 1997). The Drybones Bay kimberlite intrudes plutons of the Archean (2620 Ma) Defeat Plutonic Suite. The Defeat Plutonic Suite consists predominantly of biotite tonalite and granodiorite, with minor inclusions of the Yellowknife Supergroup metasediments (Kretschmar, 1997). In the locality of Drybones Bay it is interesting to note that there is no obvious local structure that appears to have controlled pipe emplacement (Power, 1997).

The kimberlite is oval in plan and includes crater, reworked crater (epiclastic) and diatreme facies. The extent and geometry of the pipe is defined by limited delineation drilling (Kretschmar, 1997). The geological relations within the pipe are quite complex, but at present, the information suggests three major genetically related phases, consisting of perhaps three separate intrusions (Kretschmar, 1997). Kretschmar (1997) has divided the three phases into the western (youngest), central (oldest), and eastern phases or intrusions.

The western phase consists of crater facies, a probable diatreme facies, and hypabyssal facies. The crater facies includes volcaniclastic kimberlite tuff and minor breccia with abundant pelletal lapilli and scarce lower crustal or mantle xenoliths. Within the kimberlite, macrocryst olivine and groundmass serpentinization is complete.

The diatreme facies consists of dark green, dense and unaltered olivine-rich kimberlite, while the hypabyssal facies rocks show talc-altered olivine and more abundant mantle and lower crustal xenoliths. In cross section this phase of the Drybones Bay kimberlite is champagne glass shaped, and no root zone has been encountered in drilling (Kretschmar, 1997).

The kimberlite in the central phase or intrusion is a massive, and essentially structureless diatreme facies kimberlite. In this phase, chrome-diopside megacrysts, mantle and crustal nodules are more abundant than in other lithotypes. Both micro- and macrodiamond counts are highest in this part of the kimberlite (Kretschmar, 1997).

The eastern phase resembles a dyke in cross-section and is characterized by diatreme facies kimberlite intruded into an epiclastic quartz-grain rich unit (Kretschmar, 1997).

CHAPTER 3

PETROGRAPHY

3.1 Samples

A variety of xenoliths, typical of kimberlites, are found in abundance in the Drybones Bay kimberlite, including samples of mantle rocks. Of particular interest to this study are the peridotite xenoliths that include spinel, spinel-garnet and garnet peridotites. A total of 35 xenoliths (7 garnet peridotites; 3 spinel peridotites; 2 spinel-garnet peridotites; 1 pyroxenite; 13 granulites; 2 granitic; 1 Mica-Amphibole-Rutile-Ilmenite-Diopside (MARID); 3 eclogites; 2 clastic sedimentary) were recovered from approximately 100 m of 8-cm drill core, and (in thin section) range in area from 65 to 800 mm^2. Of these xenoliths only 4 (1 spinel-garnet and 3 garnet peridotites) were used in the study because of alteration or poor Laser Ablation Microprobe (LAM) results.

Garnet grains were also recovered from kimberlite in the form of a heavy mineral coarse concentrate derived from the crushing of kimberlite drill core. Drill core from several locations within the kimberlite pipe was crushed and picked for pyrope garnet (n=65) and pyrope/chrome diopside pairs (n=9). Heavy mineral concentrates

yielded several grain size fractions, with the 1.0-2.0 mm size fraction yielding the most individual garnet grains.

3.2 Xenolith Petrography

The peridotite xenoliths have a coarse texture (Figure 3.1) with an average grain size >2mm (Harte, 1977), and grain boundaries that are smoothly curved to somewhat less regular. All of the xenoliths are altered, making the determination of the primary mineralogy challenging (Figure 3.1). Serpentine is the most common alteration product and is found pseudomorphing both pyroxene and olivine, as well as infilling cracks and fissures around garnet. Carbonate is a less frequent alteration product found pseudomorphing pyroxene, and more rarely olivine, in some of the xenoliths. Garnet and spinel are largely unaffected by the alteration in both serpentinized and carbonatized samples (Figure 3.2). Grain boundaries in the carbonatized samples are not as well preserved as in samples that have suffered serpentinization. The development of secondary phlogopite found in fractures, fissures and mantling garnet grains signifies interaction with the host kimberlite. The alteration varies in intensity, and in some samples it appears as if more than one secondary alteration process was operative. Water-rock interactions likely occurred during late stages of pipe emplacement, and are likely responsible for the formation of secondary serpentine, calcite, dolomite, chlorite and clay minerals (Pell, 1997).

The determination of the primary phases in altered xenoliths was based on the following assumptions. Serpentinized grains that have a coarse grain size, fractures and no cleavage are assumed to originally be olivine, whereas grains with relict cleavage



Figure 3.1. Photomicrograph of peridotite xenolith in thin section through cross-polarized light. Original grains have been carbonatized and/or serpentinized. Photo shows coarse texture and grain boundaries typical of xenolith samples from Drybones Bay.

and coarse grain size are assumed to be pyroxene (Figure 3.2). This distinguishing characteristic is most evident in plane-polarized light. In cases where both pyroxene and olivine are intensely altered by carbonate, differentiating the two minerals was impossible. In some samples, the carbonate replaces small grains (Figure 3.3), implying that clinopyroxene was the original primary phase, if it is assumed that in most xenoliths orthopyroxene is coarse and clinopyroxene is typically smaller in grain size (Boyd and Mertzman, 1987). However, there was little confidence in differentiating orthopyroxene from clinopyroxene based on grain size, and thus both minerals were recorded simply as pyroxene. Full petrographic descriptions of each of the xenoliths samples can be found in Appendix A.

3.2.1 Garnet Peridotites

The garnet peridotite xenoliths consist of subhedral to anhedral olivine (0.5-2 mm), pyroxene (1-4 mm) and garnet (1-7 mm). Secondary subhedral to euhedral spinel (< 1mm) is also present in most samples within relict olivine and pyroxene grains. Minor phases such as ilmenite and sulfide (sphalerite and chalcopyrite) are found in varying amounts.

The garnets commonly have a reaction rim (or corona) of optically unresolvable kelyphite (Figure 3.4). The garnets have straight to round grain boundaries in contact with kelyphite, and roundness increases with the size of the reaction rim. This reaction rim may be produced from the interaction of the kimberlite melt with the garnet. These rim vary in thickness (<0.1-0.25mm) and are usually largest in those garnets close to the edges of the xenolith, supporting the notion that the rims formed from a reaction with

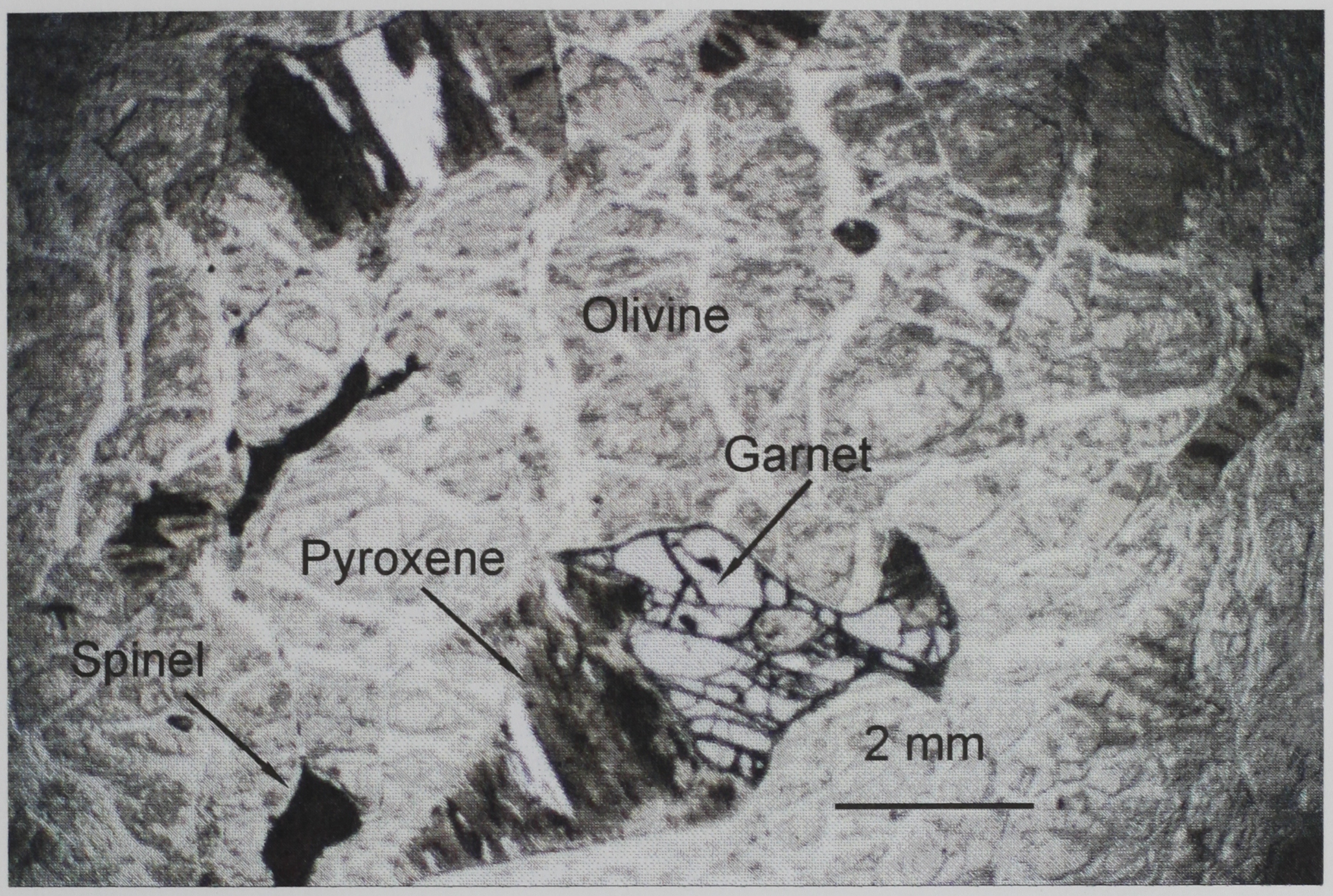

Figure 3.2. Photomicrograph of garnet peridotite xenolith from Drybones Bay in plane polarized light. Note that garnet and spinel are the only phases that remain unaltered.

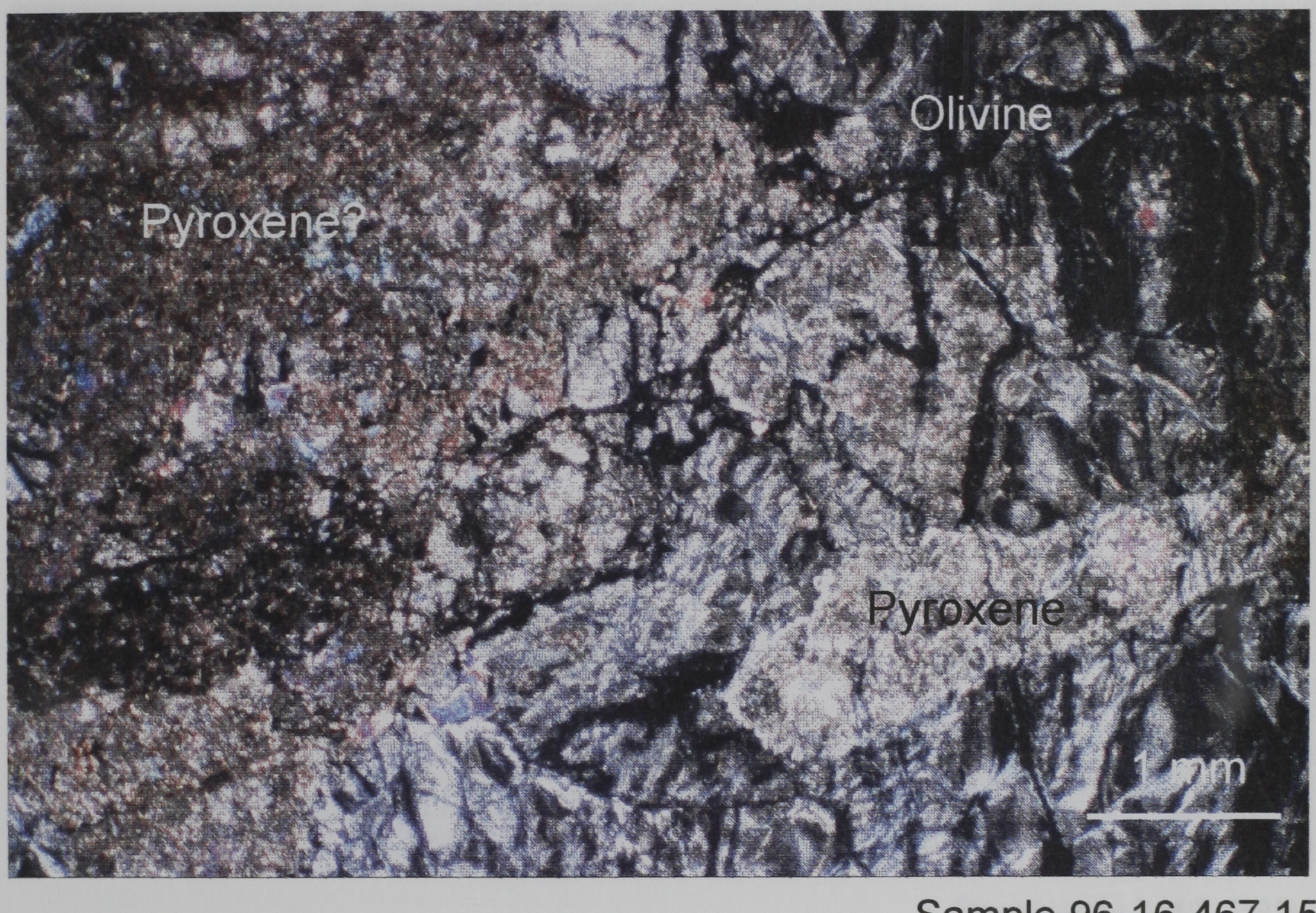

Figure 3.3. Photomicrograph of coarse grained peridotite in cross-polarized light. Olivine has been serpentinized and pyroxene carbonatized. Smaller pyroxene grains possibly indicates that the original phase was clinopyroxene rather than orthopyroxene (Boyd and Mertzman, 1987).

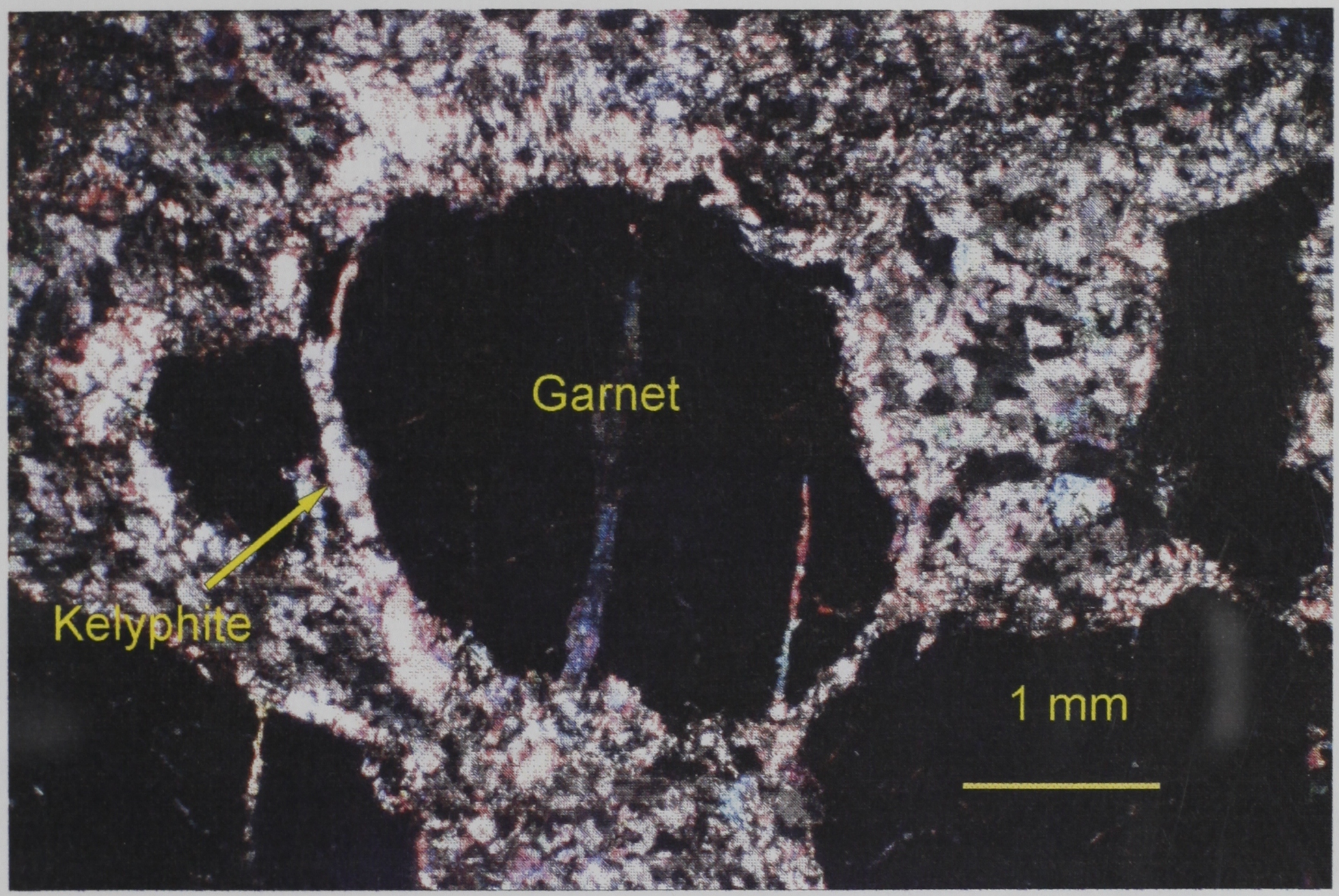

Figure 3.4. Photomicrograph of garnet peridotite in thin section in cross-polarized light. Kelyphite is seen mantling some garnets, and in this case, it is also seen invading the garnet grain due to interaction with the kimberlite.

kimberlite. The kelyphite is pleochroic green to brown in plane-polarized light. Carbonate and serpentine invade some of the garnets along fractures. Phlogopite mantles some of the garnets (mantle thickness <0.1mm), as well as invading other grains along existing fractures. This texture is also present in mantle xenoliths from the Torrie (Mackenzie and Canil, 1999) and Jericho (Kopylova et al, 1999) pipes in the Slave Province, and in many South African mantle xenoliths (Boyd and Mertzman, 1987). One sample has phlogopite filling fractures that are aligned in a preferred orientation, suggesting secondary phlogopite alteration by the introduction of the kimberlite.

3.2.2 Spinel-Garnet Peridotites

The xenolith of spinel-garnet peridotite is composed of subhedral to anhedral olivine (0.5-2mm), pyroxene (1-4mm), garnet (2-3mm) and primary subhedral to anhedral spinel (< 1mm). Minor secondary ilmenite is less abundant in these samples.

Petrographically this rock is similar to those described for the garnet peridotite suite, with a few exceptions. Garnet grains have a smaller corona of kelyphite (<1mm), and the grain size in general is somewhat smaller. Spinel in some cases possesses an alteration corona as well, indicating that spinel had interaction with the kimberlite. When spinel and garnet are found in contact, the spinel is encompassed by garnet. This would indicate that spinel was the first phase to form, followed by garnet.

3.2.3 Spinel Peridotite

Anhedral olivine and pyroxene, with an average grain size of 2-3 mm, dominates the only spinel peridotite xenolith examined. Anhedral spinel is present and averages <1 mm in size, with a few grains slightly larger than 1mm. This sample has a larger grain size than seen in other peridotites in this study. The grain boundaries are straight to slightly curved between the olivine and pyroxene, whereas with the spinel, the boundaries are more irregular as they usually are bounded by larger grains.

3.3 Modal Mineralogy

Modal data were obtained by point counting 1500 to 7500 points per sample, depending upon sample size. Appropriate grid spacing was chosen in order to minimize counting errors (Solomon, 1963). Relative errors derived from theoretical variance calculations (Solomon, 1963) are at the 95% confidence level (see Appendix B).

The modal data reveals a correlation between sample size and the amount of garnet, pyroxene and olivine in the sample. There are positive and negative correlations between modal olivine and garnet respectively, with increasing xenolith size or grid area (Figure 3.5). Similar observations have been noted by Cox et al. (1987) in garnet lherzolites from the Kaapvaal craton. The correlation signifies a spatial relationship between garnet, olivine, orthopyroxene and clinopyroxene – garnet and pyroxene being more closely spatially associated in an olivine-rich matrix (see Figure 3.6). Cox et al. (1987) use the spatial relationship to suggest that most garnet lherzolites represent former harzburgites, where clinopyroxene and garnet have formed as a result of

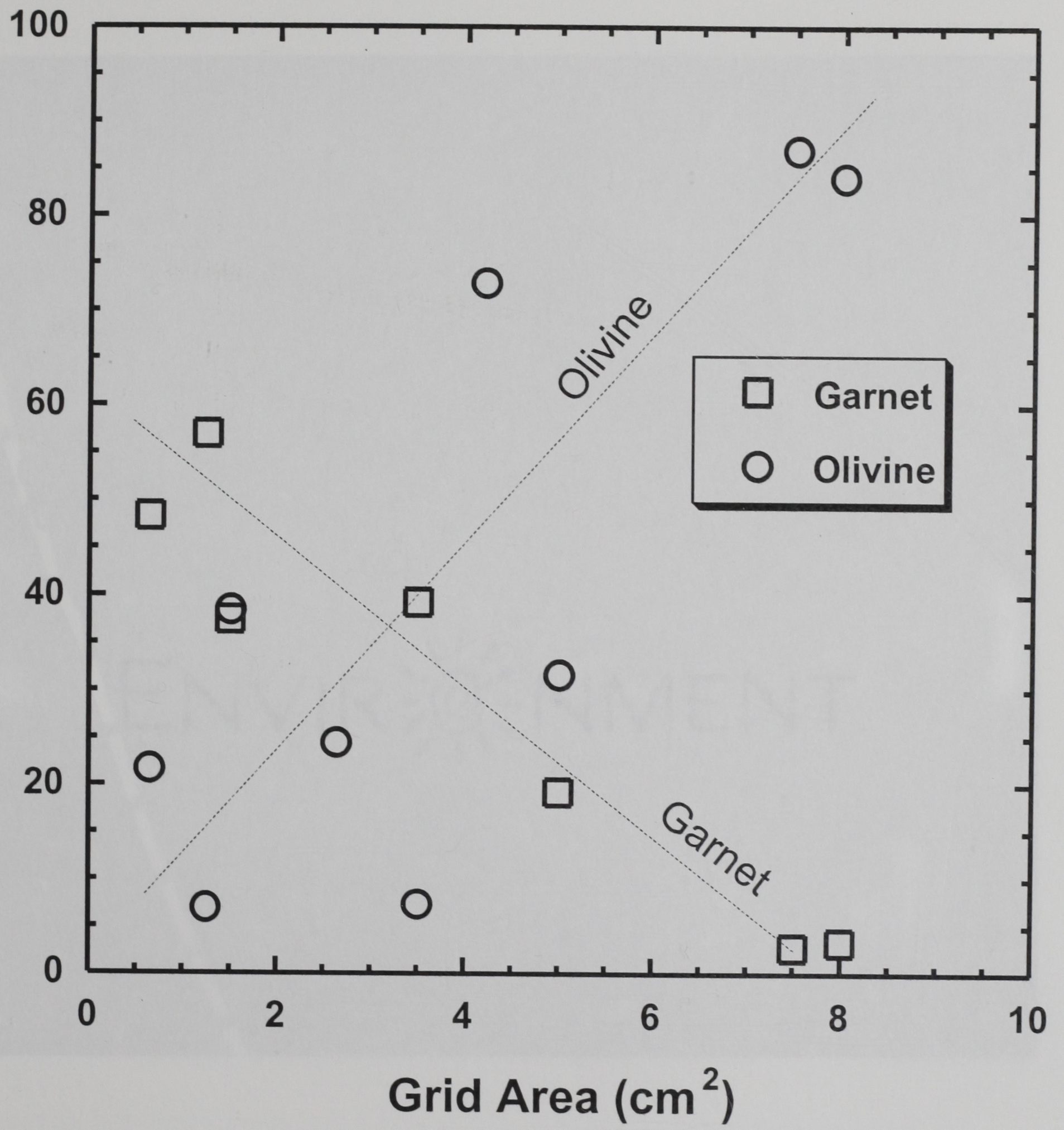

Figure 3.5. Plot of grid area (xenolith size) against modal percentages of olivine and garnet. There is an increase in modal olivine and a decrease in modal garnet with an increase in the area or size of the xenolith sample. A larger sample better represents the mineralogy of the source region because of a spatial association between garnet, pyroxene and olivine in smaller samples (Cox et al, 1987).

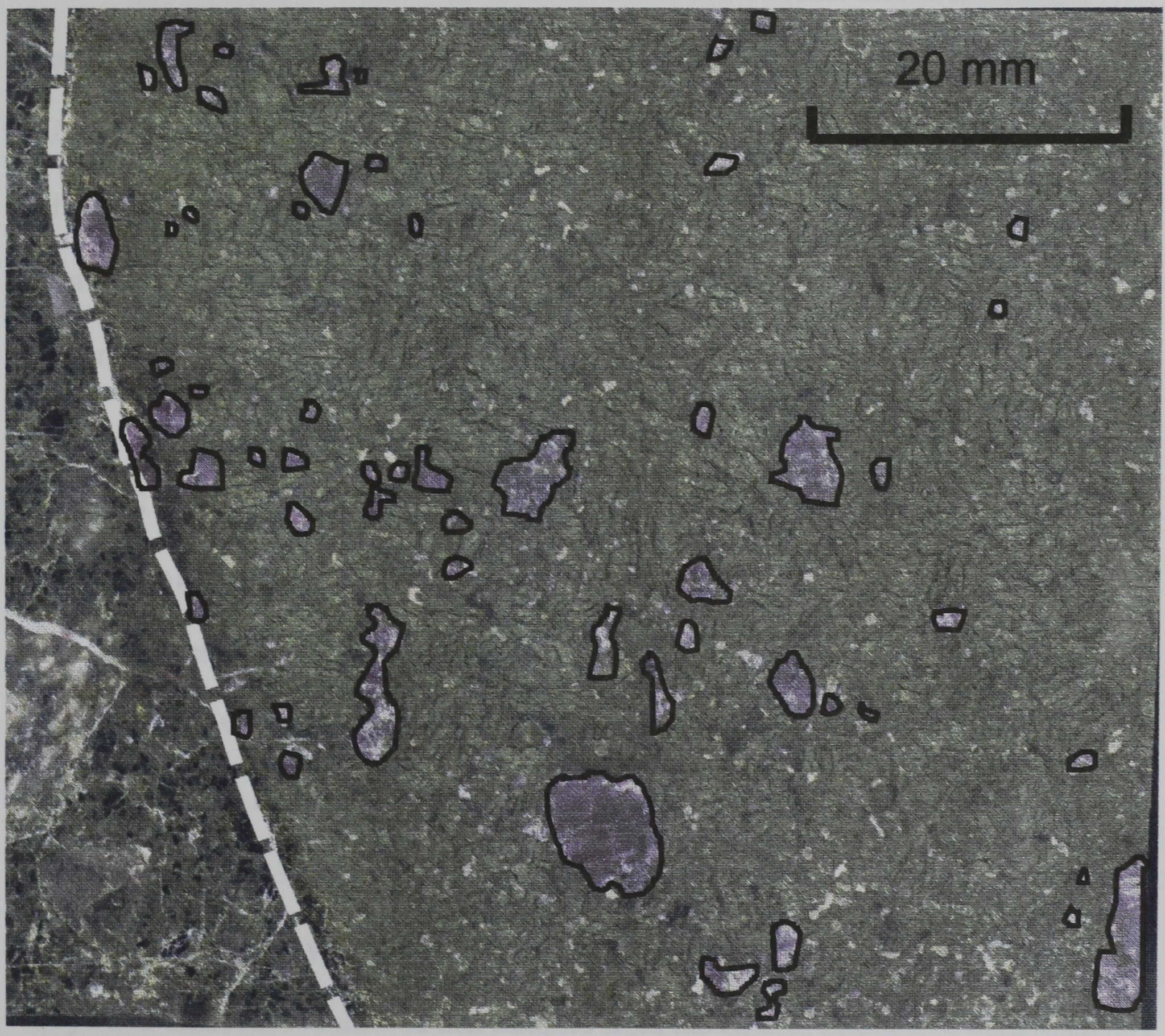

Figure 3.6. Photograph of polished slab of a kimberlite and peridotite xenolith from Drybones Bay. The photo shows a clustering of garnet grains in an olivine-rich "matrix" which explains the correlations of mode with sample area seen in Figure 3.5. The kimberlite-xenolith boundary is marked by the white dashed line. The garnet grains are outlined in black for clarity, and the remainder of the area consists mostly of olivine, with minor, small pyroxene grains.

exsolution of high Ca-orthopyroxene. Smaller samples from this study are relatively olivine-poor, therefore suggesting that there is a definite spatial bias in sampling for garnet and/or pyroxene-rich xenoliths. The bias could possibly be due to the rhealogy of the xenoliths themselves during kimberlite emplacement, with more olivine rich parts of xenoliths possibly being more prone to disaggregation. Whatever the source of this spatial relationship, the larger samples are more likely a true representation of mantle mineralogy.

Extrapolation to the minimum scale of approximately 7-8 cm^2 recommended by Cox et al (1987) to eliminate the spatial bias would suggest a mantle mineralogy with ~70-90% olivine beneath Drybones Bay. This is relatively olivine-rich compared to the mantle beneath other Archean cratons such as the Kaapvaal and Siberia (Boyd et al, 1997). This olivine content is also higher than that recognized for mantle lithosphere in the central Slave Province by MacKenzie and Canil (1999), but their samples were relatively small (< 3 cm^2) and may have suffered a similar spatial association of pyroxene and garnet, which obscures the true mineralogy of the lithospheric mantle. Boyd and Canil (1997) showed that samples from the Grizzly kimberlite were relatively olivine-rich, but their samples were also small. The more olivine-rich nature of the large sample (Figure 3.6) from Drybones may be due to either proximity to craton edge, or a unique petrogenetic history for these samples. At this point in time, there is insufficient modal data from mantle xenoliths from the Slave craton to make any further generalizations about its modal mineralogy.

3.4 Heavy Mineral Concentrate

Garnet grains (n=34) from heavy mineral concentrate were studied under a stereomicroscope. The garnet grains show little to no signs of alteration, with most grains having good clarity and few kelyphite reaction rims (Figure 3.7). A large range in colour from light red to deep purple is apparent (Figure 3.8). Garnets with a light red to deep purple-violet colour were chosen for analysis because they were predicted to represent the most peridotitic (pyropic) of the garnets in the concentrate. These garnets were classified visually based upon their colour, and were given a colour number from 1 to 5, 1 representing light red, and 5 representing deep purple (Figure 3.8). These colour numbers are used to compare garnet chemistry with the range in colours noted in the garnets.

The garnet grains are sub-rounded to angular with poor to moderate sphericity (Figure 3.7). Grains that show poor sphericity and high angularity are produced as a consequence of the core crushing process from which the heavy mineral concentrates are extracted. These grains also have higher clarity and show obvious conchoidal fracturing, and were evidently once part of a larger garnet grain or xenolith. Grains that are more rounded with higher sphericity have a surface that appears frosted (Figure 3.7), this frosting possibly being the result of existing separately (as a xenocryst?) while entrained in the rising kimberlite melt. Kelyphite reaction rims, when present, are more abundant on the rounded, spherical grains.

Nine (physically attached) Cr-diopside/garnet pairs were recognized in the coarse concentrate. The diopside grains have a distinctive bright emerald green colour and show no sign of alteration (Figure 3.9). It is not clear why some clinopyroxene



Figure 3.7. Photograph of garnet grains from heavy mineral coarse concentrate. Grain A is rounded with high sphericity, and grain B is angular with low sphericity. Also note how grain A appears frosted, while grain B has no frosting with more obvious conchoidal fracturing.



Figure 3.8. Photograph of garnet grains from heavy mineral coarse concentrates. The photo shows the range in colours of selected garnets; 1 representing light red and 5 representing deep purple. Deep purple (5) garnet grains are more Cr-rich pyrope garnets.

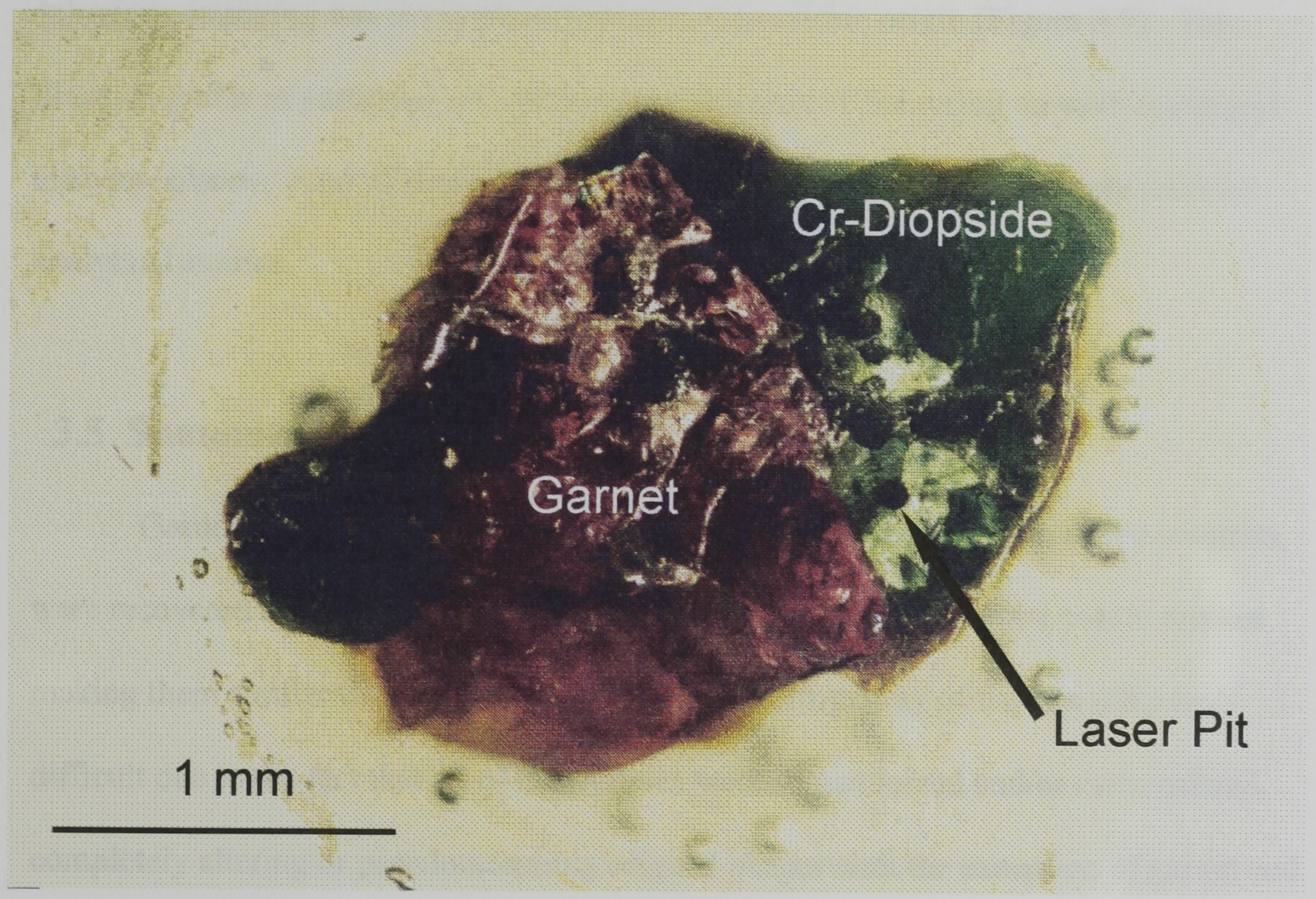

Figure 3.9. Photograph of garnet/clinopyroxene pair from heavy mineral coarse concentrate mounted in epoxy and polished. Garnet/clinopyroxene grains showed low sphericity and were generally angular. Note the laser pits in both the garnet and clinopyroxene. These pits are approximately 100 μm in diameter.

in concentrate were not carbonatized and/or serpentinized, while those in xenoliths consistently were. The garnet/diopside pairs are angular with poor to moderate sphericity implying that these grain pairs are of xenolithic origin (Figure 3.9). The diopside grains in particular are more angular because of fracturing on well-developed cleavage planes. Four of these grain pairs gave good LAM results and were used in analytical studies.

3.5 Summary

Garnet samples from peridotite xenoliths and heavy mineral coarse concentrate were recovered from drill core (n=42). The peridotite xenoliths have a coarse texture making them similar to other cratons worldwide. Petrography of the xenoliths is difficult due to the fact that all of the samples were serpentinized and/or carbonatized, completely altering or pseudomorphing original phases with the exception of garnet and spinel. The xenolith samples from Drybones Bay included spinel peridotites and garnet peridotites, indicating the host kimberlite sampled at least two "facies" of peridotite. Modal analyses were done based on reasonable assumptions using the presence of cleavage to estimate the original mineralogy of the peridotite xenoliths. Garnet xenocrysts and garnet/clinopyroxene pairs were studied using a stereomicroscope, however determining the other original xenolith minerals that coexisted with these individual grains was not possible. Garnet xenocryst morphology ranged from well rounded with high sphericity to poorly rounded with low sphericity, the latter likely originating from a larger xenolith before the concentrating process.

CHAPTER 4

MINERAL CHEMISTRY

4.1 Major Element Geochemistry

A total of 80 garnets were analyzed (6 from garnet peridotite xenoliths, 74 from concentrate) for both major and trace elements. Of these 80 garnets originally analyzed, only 42 garnet grains were incorporated because analytical results for these 42 grains contained most, if not all, of the suite of elements of interest in the study. The remaining grains were omitted because of LAM ICP-MS detection limits, or because the grains were too fractured or small to give useable results. A description of the analytical methods are provided in Appendix G.

4.1.1 Garnet

Garnets from Drybones Bay peridotite xenoliths and heavy mineral concentrates are typical Cr-pyropes (Appendix C). These garnets are further subdivided based on a plot of their CaO vs Cr_2O_3 compositions (Figure 4.1), which shows that the garnet suite from Drybones Bay is dominated by wehrlite and lherzolite, with possibly minor harzburgite (Dawson and Stephens, 1975; Sobolev, 1973). The line distinguishing between lherzolite and harzburgite in this plot is equivalent to the 85% line introduced

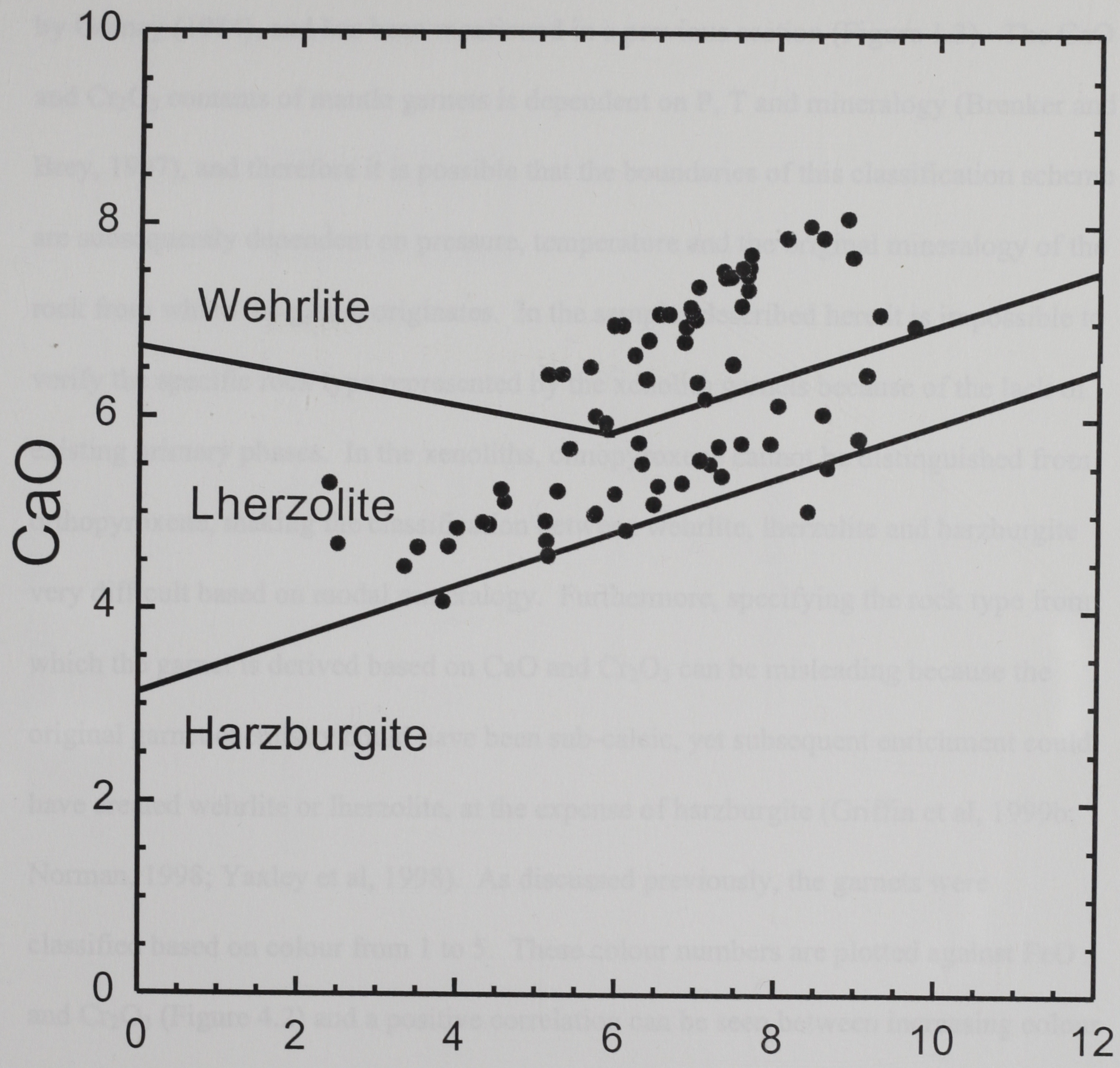

Figure 4.1. Plot of CaO and Cr_2O_3 compositions for Drybones Bay garnets. The plot shows that the garnet population is dominated by wehrlite and lherzolite, with minor harzburgite (Dawson and Stephens, 1975; Sobolev, 1973).

by Gurney (1984), and has been mentioned in a previous section (Figure 1.3). The CaO and Cr_2O_3 contents of mantle garnets is dependent on P, T and mineralogy (Brenker and Brey, 1997), and therefore it is possible that the boundaries of this classification scheme are subsequently dependent on pressure, temperature and the original mineralogy of the rock from which the garnet originates. In the samples described here it is impossible to verify the specific rock type represented by the xenolith garnets because of the lack of existing primary phases. In the xenoliths, clinopyroxene cannot be distinguished from orthopyroxene, making the classification between wehrlite, lherzolite and harzburgite very difficult based on modal mineralogy. Furthermore, specifying the rock type from which the garnet is derived based on CaO and Cr_2O_3 can be misleading because the original garnet chemistry could have been sub-calcic, yet subsequent enrichment could have created wehrlite or lherzolite, at the expense of harzburgite (Griffin et al, 1999b; Norman, 1998; Yaxley et al, 1998). As discussed previously, the garnets were classified based on colour from 1 to 5. These colour numbers are plotted against FeO and Cr_2O_3 (Figure 4.2) and a positive correlation can be seen between increasing colour number and increasing Cr_2O_3 content. For cations such as Fe^{3+} and Cr^{3+}, the absorption band will extend into the visible part of the spectrum, causing absorption strongest in the violet range (Rossman, 1988), explaining why an increase in Cr_2O_3 within the garnet population will result in the garnets becoming darker purple in colour.

4.1.2 Clinopyroxene

The average composition of the clinopyroxene in the garnet/clinopyroxene pairs from heavy mineral concentrate is $Wo_{45}En_{51}Fs_4$, they have a high Cr content of 0.8618-4.231 wt% Cr_2O_3, and are classified as Cr-diopside (Appendix C). The diopsides have

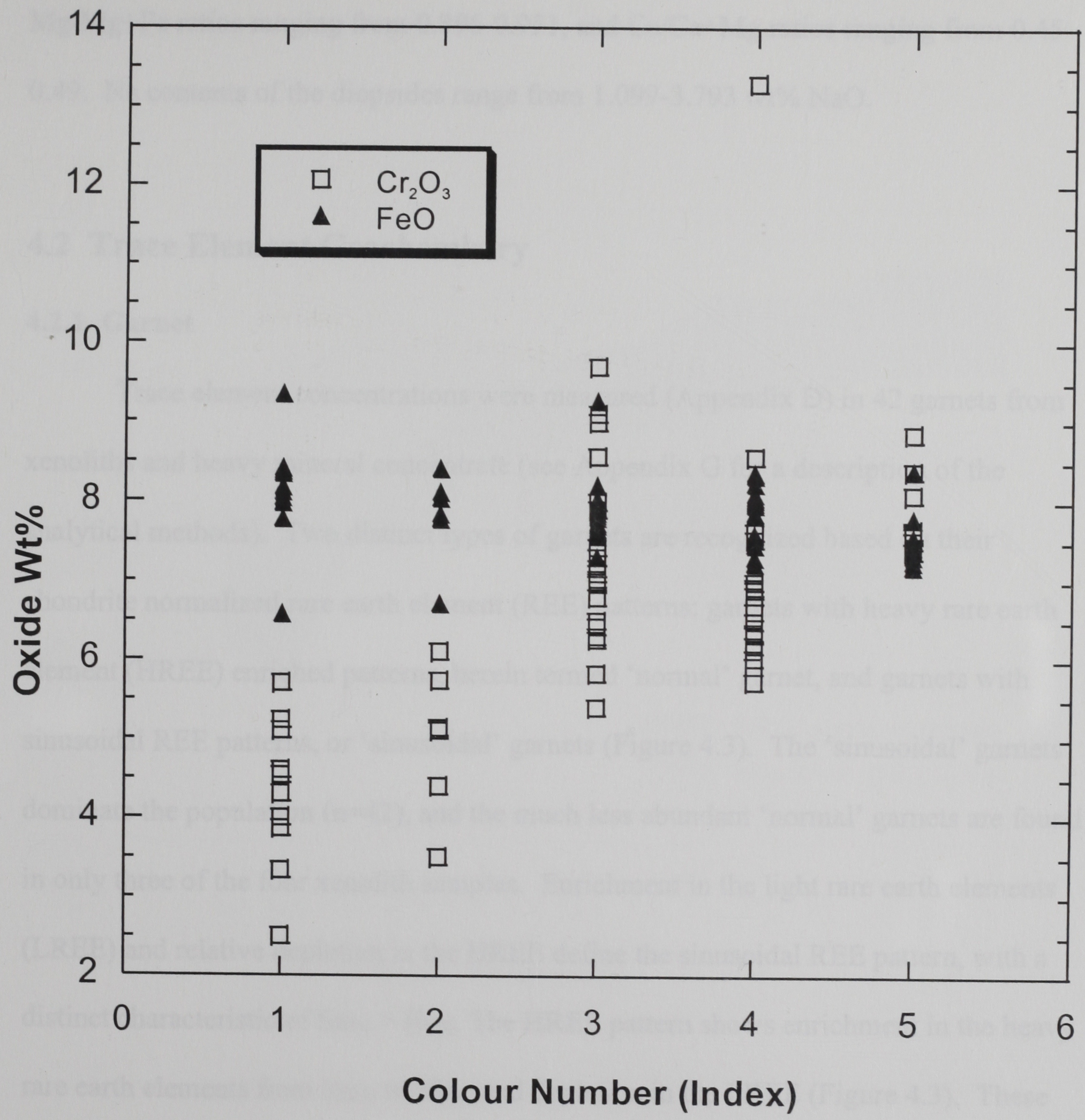

Figure 4.2. Plot of colour number (index) against oxide weight percent for both FeO and Cr_2O_3. Colour number 1 represents a light red garnet, and colour number 5 represents a deep purple garnet. With increasing colour number the amount of FeO decreases, while Cr_2O_3 increases.

Mg/Mg+Fe ratios ranging from 0.896-0.951, and Ca/Ca+Mg ratios ranging from 0.45-0.49. Na contents of the diopsides range from 1.099-3.793 wt% NaO.

4.2 Trace Element Geochemistry

4.2.1 Garnet

Trace element concentrations were measured (Appendix D) in 42 garnets from xenoliths and heavy mineral concentrate (see Appendix G for a description of the analytical methods). Two distinct types of garnets are recognized based on their chondrite normalized rare earth element (REE) patterns: garnets with heavy rare earth element (HREE) enriched patterns, herein termed 'normal' garnet, and garnets with sinusoidal REE patterns, or 'sinusoidal' garnets (Figure 4.3). The 'sinusoidal' garnets dominate the population (n=42), and the much less abundant 'normal' garnets are found in only three of the four xenolith samples. Enrichment in the light rare earth elements (LREE) and relative depletion in the HREE define the sinusoidal REE pattern, with a distinct characteristic of $Sm_N > Ho_N$. The HREE pattern shows enrichment in the heavy rare earth elements from Sm_N to Yb_N, and depletion in the LREE (Figure 4.3). These patterns can be represented by the ratio of La_N over Yb_N. The 'sinusoidal' garnets have $La_N/Yb_N = 0.10\text{-}4.4$, whereas the 'normal' garnets have $La_N/Yb_N = 0.01\text{-}0.07$. Intermediate patterns can also be seen with La_N/Yb_N ratios between the given values above. Both of the REE patterns have been recognized in garnets from xenoliths and as inclusions in diamonds from southern Africa and Siberia (Stachel et al, 1998; Hoal et al, 1994; Shimizu and Richardson, 1987; Shimizu, 1975; Nixon et al, 1987; Griffin et al, 1999b).

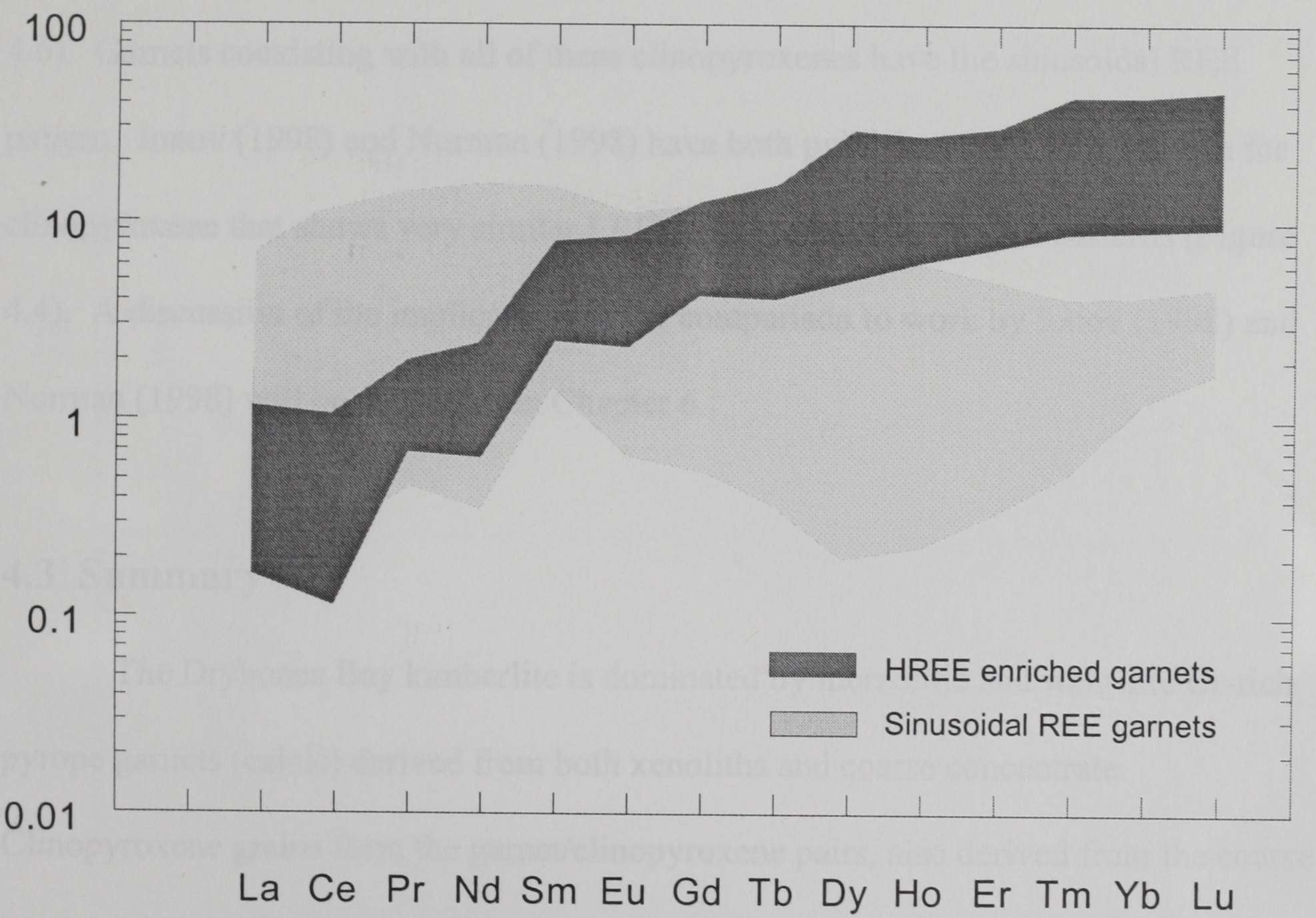

Figure 4.3. Chondrite normalized REE patterns from the Drybones Bay kimberlite with representative fields for all garnet results. The light gray represents HREE-enriched or 'normal' garnets (n = 4), and the dark gray represents 'sinusoidal' or S-shaped garnets (n = 42). Plots of each individual garnet REE pattern can be seen in Appendix F.

4.2.2 Clinopyroxene

Clinopyroxene analyses can also be found in Appendix D. Grains found in direct contact with garnet have a distinct LREE-enriched trace element pattern (Figure 4.6). Garnets coexisting with all of these clinopyroxenes have the sinusoidal REE pattern. Ionov (1998) and Norman (1998) have both published trace element data for clinopyroxene that shows very similar LREE-enriched clinopyroxene patterns (Figure 4.4). A discussion of the implications of the comparison to work by Ionov (1998) and Norman (1998) will be addressed in Chapter 6.

4.3 Summary

The Drybones Bay kimberlite is dominated by lherzolitic and wehrlitic Cr-rich pyrope garnets (calcic) derived from both xenoliths and coarse concentrate.

Clinopyroxene grains form the garnet/clinopyroxene pairs, also derived from the coarse concentrate, are Cr-rich diopside. Trace element data acquired using the LAM ICP-MS reveals two different types of garnet in the population according to their chondrite normalized trace element pattern. One garnet type has a sinusoidal chondrite normalized trace element pattern, whereas the other type has a heavy rare earth element enriched pattern. Diopside coexisting with garnet has a distinct LREE-enriched pattern matching the 'sinusoidal' HREE-enriched coexisting garnet.

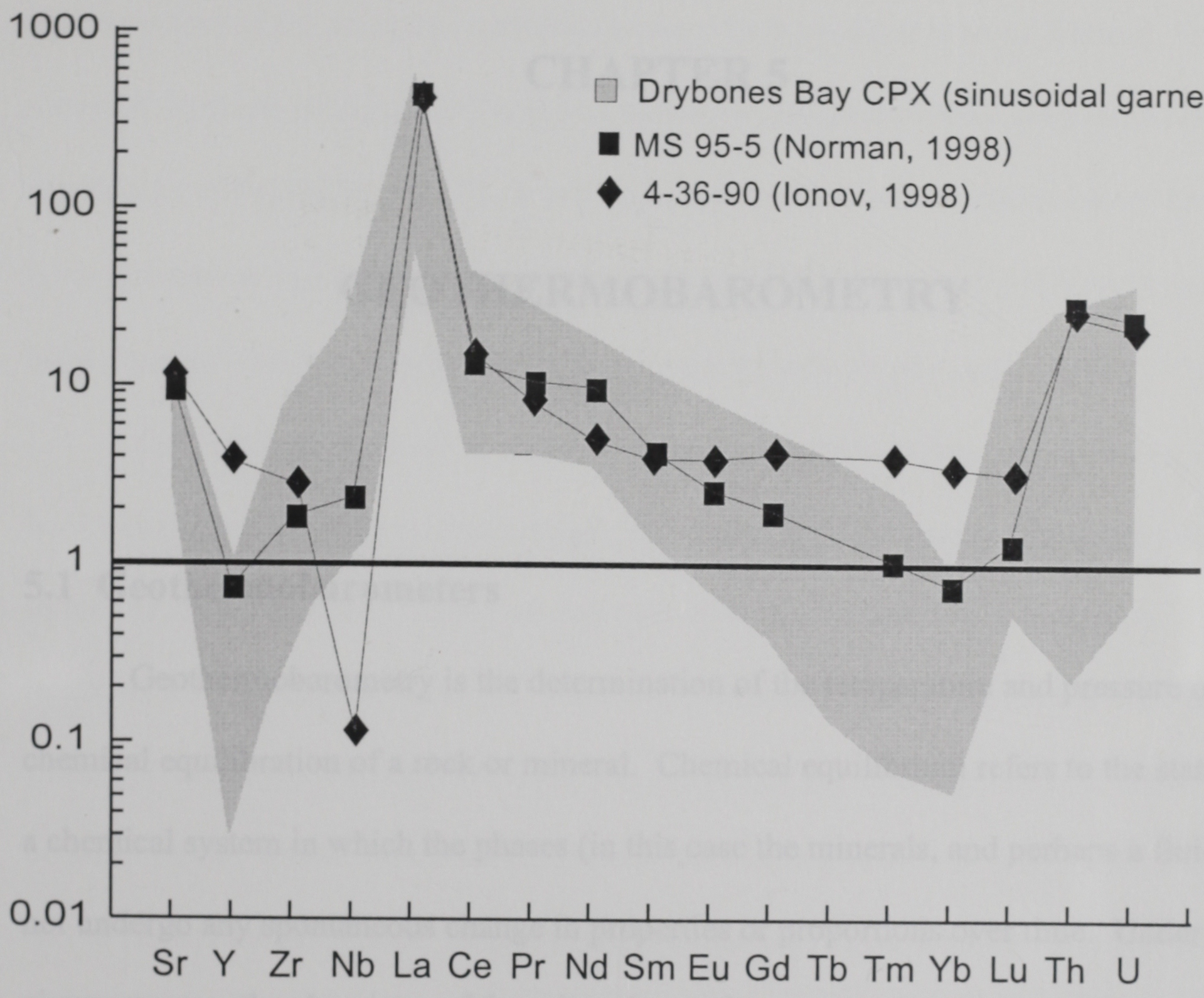

Figure 4.4. Primitive mantle normalized clinopyroxene trace element abundances for garnet/clinopyroxene pairs (n = 4). Light gray field represents range of data from this study. For comparison, clinopyroxene data has been included from Norman (1998) and Ionov (1998).

CHAPTER 5

GEOTHERMOBAROMETRY

5.1 Geothermobarometers

Geothermobarometry is the determination of the temperature and pressure of chemical equilibration of a rock or mineral. Chemical equilibrium refers to the state of a chemical system in which the phases (in this case the minerals, and perhaps a fluid) do not undergo any spontaneous change in properties or proportions over time. Under such circumstances, the chemistry of the minerals, or phases present, will record the conditions (i.e. pressure, temperature and fO_2) of equilibrium. Pressure and temperature estimates for mantle rocks can tell us much about the past and present thermal states of the mantle. Xenoliths from parts of the mantle that are sampled by kimberlites reveal information about lithospheric evolution and craton formation according to their pressure-temperature (P-T) history.

Geothermobarometry is usually considered separately in terms of geothermometry and geobarometry. Geothermometry records the temperature of chemical equilibration under particular conditions of pressure and composition based on

the temperature dependence of the equilibria. Geobarometry involves the interpretation of pressure-sensitive chemical or mineral reactions for the direct or indirect determination of the pressure conditions under which a rock or mineral formed. In terms of thermodynamics, equilibria best suited for geothermometry have large changes in enthalpy in the reaction ($\Delta H°_{rxn}$), and equilibria best suited for geobarometry have large changes in volume ($\Delta V°_{rxn}$), and where the equilibrium constant (K) undergoes large changes with temperature and pressure respectively (Wood and Fraser, 1977).

Conventional methods of thermobarometry incorporate reactions between at least two phases in a mineral assemblage, and these reactions are usually either pressure or temperature dependent. There are typically two types of reactions; exchange reactions and net-transfer reactions. Exchange reactions involve a balanced reaction among phases where cations exchange sites according to a distribution coefficient between phases, and in which the progress of the reaction results in no change in the modal amount of the phases. Cation exchange reactions occur where two or more minerals in a rock can exhibit the same ionic substitution – a good example is the exchange of ferrous iron and magnesium between ferromagnesian silicates. Conversely, a net-transfer reaction is a balanced reaction among phases in which the progress of the reaction results in a change in the modal amounts of the phases.

When dealing with mantle rocks, the most applicable geothermobarometers are based on equilibria between some combination of coexisting olivine, orthopyroxene, clinopyroxene, garnet and spinel – all common mantle minerals. One example of an exchange geothermometer used with mantle assemblages is the exchange of Fe and Mg

between olivine and garnet (O'Neill and Wood, 1979):

$$Fe_2SiO_4 + Mg_3Al_2Si_3O_{12} \Leftrightarrow Mg_2SiO_4 + Fe_3Al_2Si_3O_{12} \quad (5.1)$$

(Fa) (Py) (Fo) (Alm)

where Fa and Fo represent the fayalite and forsterite components in olivine, and Py and Alm are the pyrope and almandine components in garnet, respectively. Another example of an exchange thermometer involving Fe and Mg is their exchange between clinopyroxene and garnet (Krogh, 1988). Additionally, an example of an exchange geobarometer would be the Ca exchange between coexisting olivine and clinopyroxene (Köhler and Brey, 1990).

Net-transfer reactions are also used as geothermobarometers, and an example involving such a reaction would be an exchange geobarometer that uses the Al content of orthopyroxene, and is based on the following reaction:

$$Mg_2Si_2O_6 + MgAl_2SiO_6 \Leftrightarrow Mg_3Al_2Si_3O_{12} \quad (5.2)$$

(En) (Mg-Ts) (Py)

where (Mg-Ts) is the Mg-Tschermaks component in orthopyroxene (En) and garnet (Py) (Carswell, 1991).

Another useful geothermometer for mantle-derived rocks is the partitioning of Ni between coexisting garnet and olivine since Ni shows a strong partition between garnet and olivine. This thermometer was developed empirically (Griffin et al, 1989;

Ryan et al, 1996) and experimentally in two studies (Canil, 1994; Canil, 1999). However, there has been some discrepancy between the empirical and experimental calibrations of the Ni-in-garnet geothermometer (see Canil, 1996; Griffin and Ryan, 1996).

The empirical calibration has a slope on a graph of ln $D_{Ni}^{gt/ol}$ versus 1000/T that is much lower than the slope calibrated experimentally, and this slope difference can be seen when both calibrations are plotted (Figure 5.1). This slope difference results in a large variation in temperatures above 1400 °C and below 900 °C (Canil, 1999). The discrepancy mostly stems from problems in the empirical calibration. The empirical calibration relies on the use of an 'independent' temperature, which is estimated by another geothermometer. The independent temperatures that were used as input in the empirical calibration are erroneous because of significant pressure dependence (Canil, 1999). These pressure effects are not accounted for in the empirical calibration, and because of this, higher-pressure samples will always provide a higher independent temperature (Canil, 1999). For the purposes of this study it is assumed that the experimental calibration of T_{Ni} (Canil, 1999) at natural abundances is deemed a more reliable estimation of the equilibration temperatures of mantle garnets from Drybones Bay.

5.2 Temperature Calculations

As discussed previously, garnet, and in a few cases spinel, are the only phases that are unaltered in xenolith samples. Garnet is found in abundance in drill core from the Drybones Bay kimberlite. The absence of coexisting phases with garnet, the

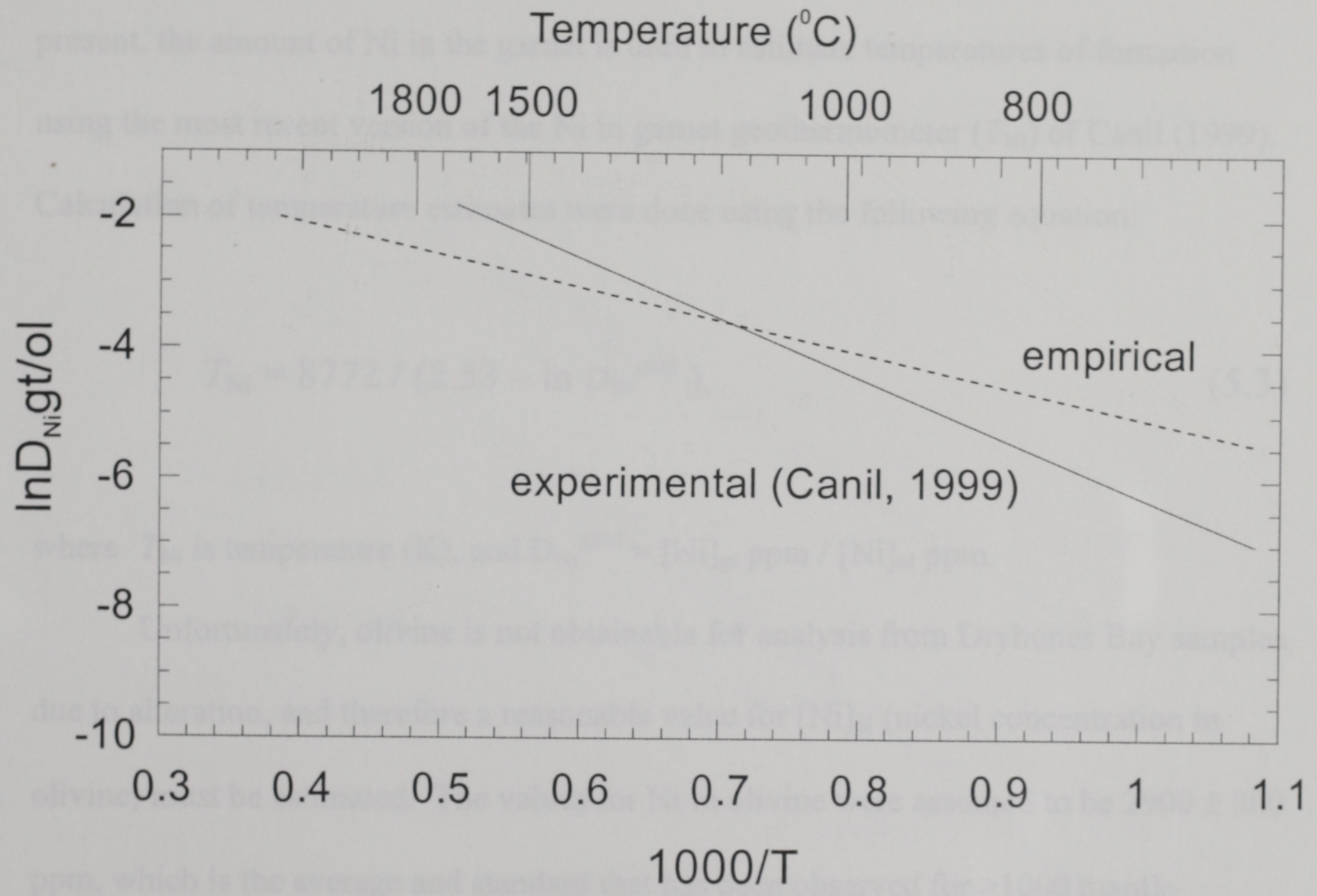

Figure 5.1. Comparison of experimental and empirical calibrations of the Ni-in-garnet geothermometer. The slope of the empirical calibration (Ryan et al, 1996) is much lower than that of the experimental calibration (Canil, 1999) which results in significantly different calculated temperatures above 1400°C and below 900°C.

exception being a few grains of garnet and clinopyroxene in contact, made it impossible to use conventional peridotite geothermobarometers in this study to estimate the pressure and temperature of origin of these samples. Since garnet is the only phase present, the amount of Ni in the garnet is used to estimate temperatures of formation using the most recent version of the Ni in garnet geothermometer (T_{Ni}) of Canil (1999). Calculation of temperature estimates were done using the following equation:

$$T_{Ni} = 8772 / (2.53 - \ln D_{Ni}^{gt/ol}), \qquad (5.3)$$

where T_{Ni} is temperature (K), and $D_{Ni}^{gt/ol} = [Ni]_{gt}$ ppm / $[Ni]_{ol}$ ppm.

Unfortunately, olivine is not obtainable for analysis from Drybones Bay samples due to alteration, and therefore a reasonable value for $[Ni]_{ol}$ (nickel concentration in olivine) must be estimated. The values for Ni in olivine were assumed to be 2900 ± 300 ppm, which is the average and standard that has been observed for >1000 mantle analyses (Griffin and Ryan, 1995; Ryan et al, 1996). The uncertainty in Ni concentration in olivine and the experimental uncertainty give a conservative error of ± 70 °C in estimated temperatures (Figure 5.2). Values for the concentration of Ni in garnet ($[Ni]_{gt}$) for the Drybones Bay garnets ranged from 13 - 62 ppm. These Ni values in garnet give results using the Ni-in-garnet geothermometer (Canil, 1999) of temperatures of equilibration (T_{Ni}) between 849 °C and 1212 °C for Drybones Bay garnets.

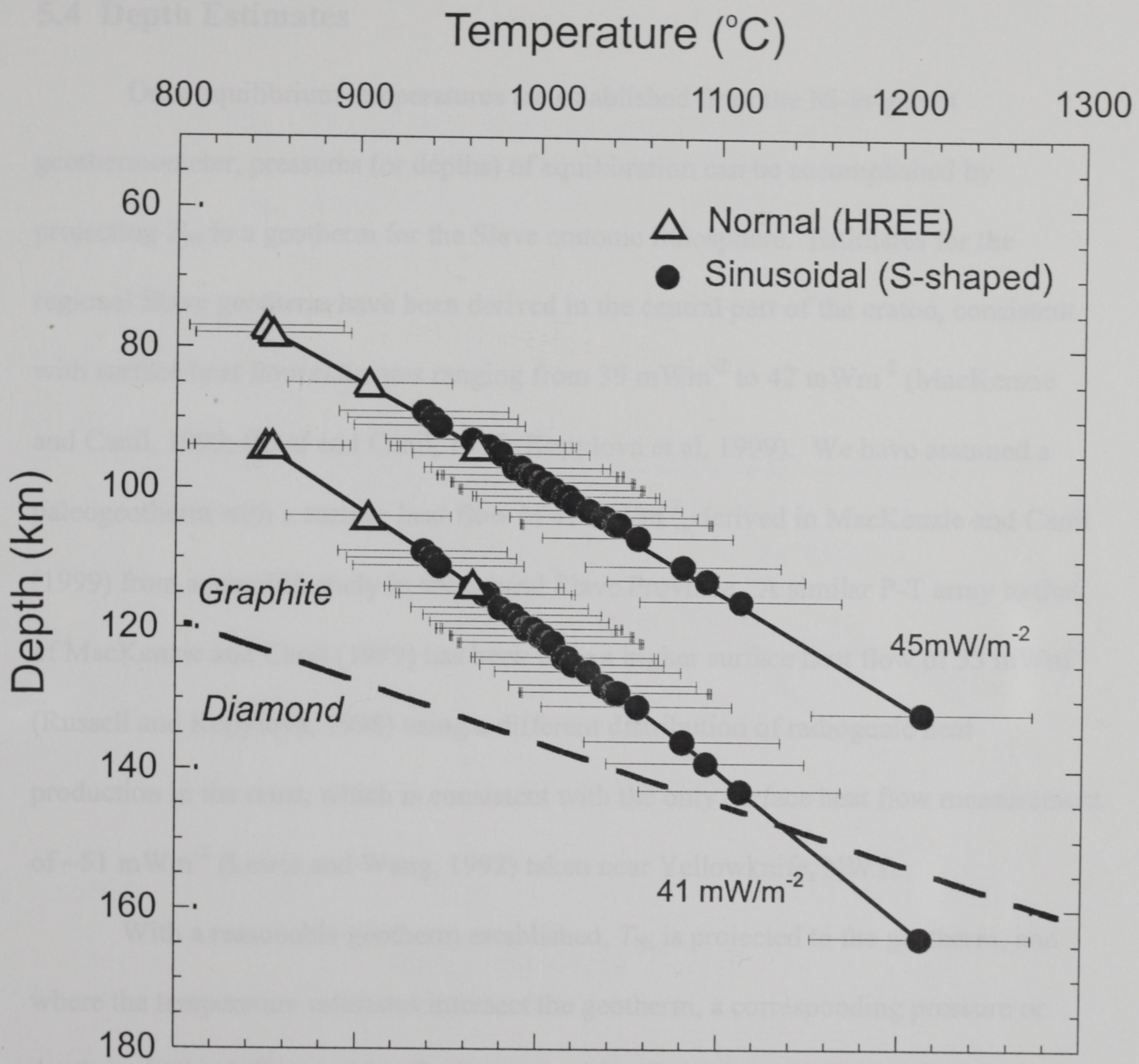

Figure 5.2. Temperature and depth estimates plotted on 41 mW/m^2 and 45 mW/m^2 geotherms for comparison. The temperature estimates give an error of +/- 70 ° C using the Ni-in-garnet geothermometer (Canil, 1999). The triangles represent those garnets with a HREE-enriched trace element pattern, and the circles represent garnets with a sinusoidal trace element pattern.

5.4 Depth Estimates

Once equilibrium temperatures are established from the Ni-in-garnet geothermometer, pressures (or depths) of equilibration can be accomplished by projecting T_{Ni} to a geotherm for the Slave cratonic lithosphere. Estimates for the regional Slave geotherm have been derived in the central part of the craton, consistent with surface heat flow estimates ranging from 39 mWm^{-2} to 42 mWm^{-2} (MacKenzie and Canil, 1999; Boyd and Canil, 1997; Kopylova et al, 1999). We have assumed a paleogeotherm with a surface heat flow of 41 mWm^{-2}, derived in MacKenzie and Canil (1999) from a xenolith study in the central Slave Province. A similar P-T array to that of MacKenzie and Canil (1999) has been fit to a higher surface heat flow of 53 mWm^{-2} (Russell and Kopylova, 1998) using a different distribution of radiogenic heat production in the crust, which is consistent with the only surface heat flow measurement of ~51 mWm^{-2} (Lewis and Wang, 1992) taken near Yellowknife, NWT.

With a reasonable geotherm established, T_{Ni} is projected to the geotherm, and where the temperature estimates intersect the geotherm, a corresponding pressure or depth is obtained (Figure 5.3). Each garnet with a T_{Ni} and a related depth is then plotted to give a depth-temperature (or pressure-temperature) array for the suite of garnets (Figure 5.2). Plotted as well in Figure 5.2 is a slightly higher geotherm for a surface heat flow value of 45 mWm^{-2} to illustrate how drastically the geotherm estimate can alter the depth estimates.

Projections of T_{Ni} to a 41 mWm^{-2} geotherm estimates the minimum lithospheric thickness sampled by the Drybones Bay kimberlite to be approximately 165 km. The Drybones Bay kimberlite is diamondiferous (Kretschmar, 1997), making this depth

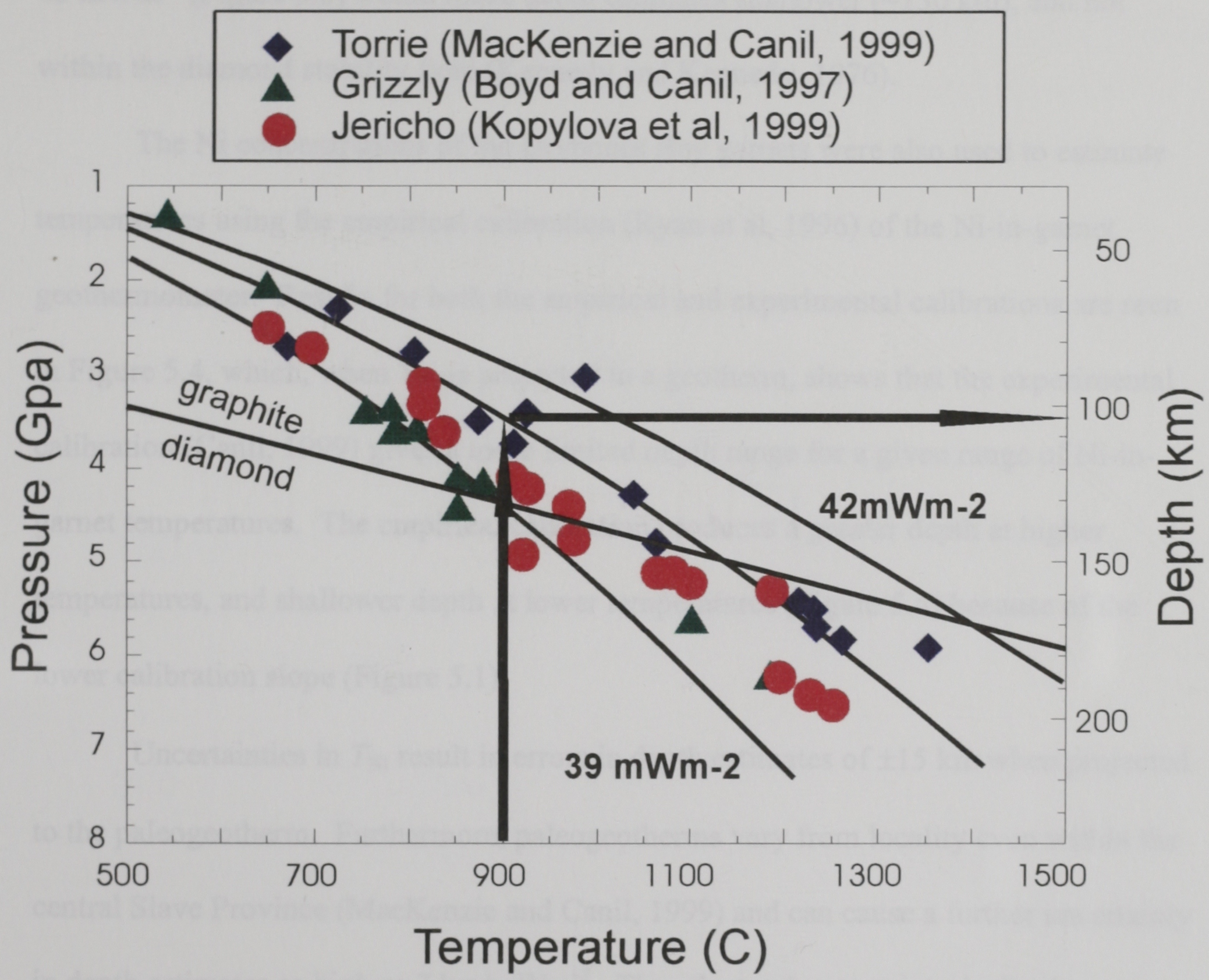

Figure 5.3. Slave geotherms estimated by three separate studies in the central part of the Slave Province, NWT (MacKenzie and Canil, 1999; Kopylova et al, 1999; Boyd and Canil, 1997). The arrows demonstrate how a given temperature can be projected to a geotherm resulting in a corresponding depth estimate . The studies from the central Slave all use independent geobarometers for pressure.

estimate from T_{Ni} with this geotherm reasonable. Assuming a higher geotherm, such as 45 mWm^{-2} (Figure 5.2) would make depth estimates shallower (~130 km), and not within the diamond stability field (Kennedy and Kennedy, 1976).

The Ni concentrations of the Drybones Bay garnets were also used to estimate temperatures using the empirical calibration (Ryan et al, 1996) of the Ni-in-garnet geothermometer. Results for both the empirical and experimental calibrations are seen in Figure 5.4, which, when T_{Ni} is projected to a geotherm, shows that the experimental calibration (Canil, 1999) gives a more limited depth range for a given range of Ni-in-garnet temperatures. The empirical calibration produces a greater depth at higher temperatures, and shallower depth at lower temperatures (Figure 5.4) because of the lower calibration slope (Figure 5.1).

Uncertainties in T_{Ni} result in errors in depth estimates of ±15 km when projected to the paleogeotherm. Furthermore, paleogeotherms vary from locality even within the central Slave Province (MacKenzie and Canil, 1999) and can cause a further uncertainty in depth estimates as high as 7 km/mWm^{-2}. Thus the total uncertainty in depth estimates could be as large as ±22 km with only a 1 mWm^{-2} change in the paleogeotherm. For the purposes of our study, however, we use the depth estimates principally to look at a "relative" stratigraphy of the garnets. In only one case in our interpretations below do we rely on absolute depths to compare with regional seismic observations.

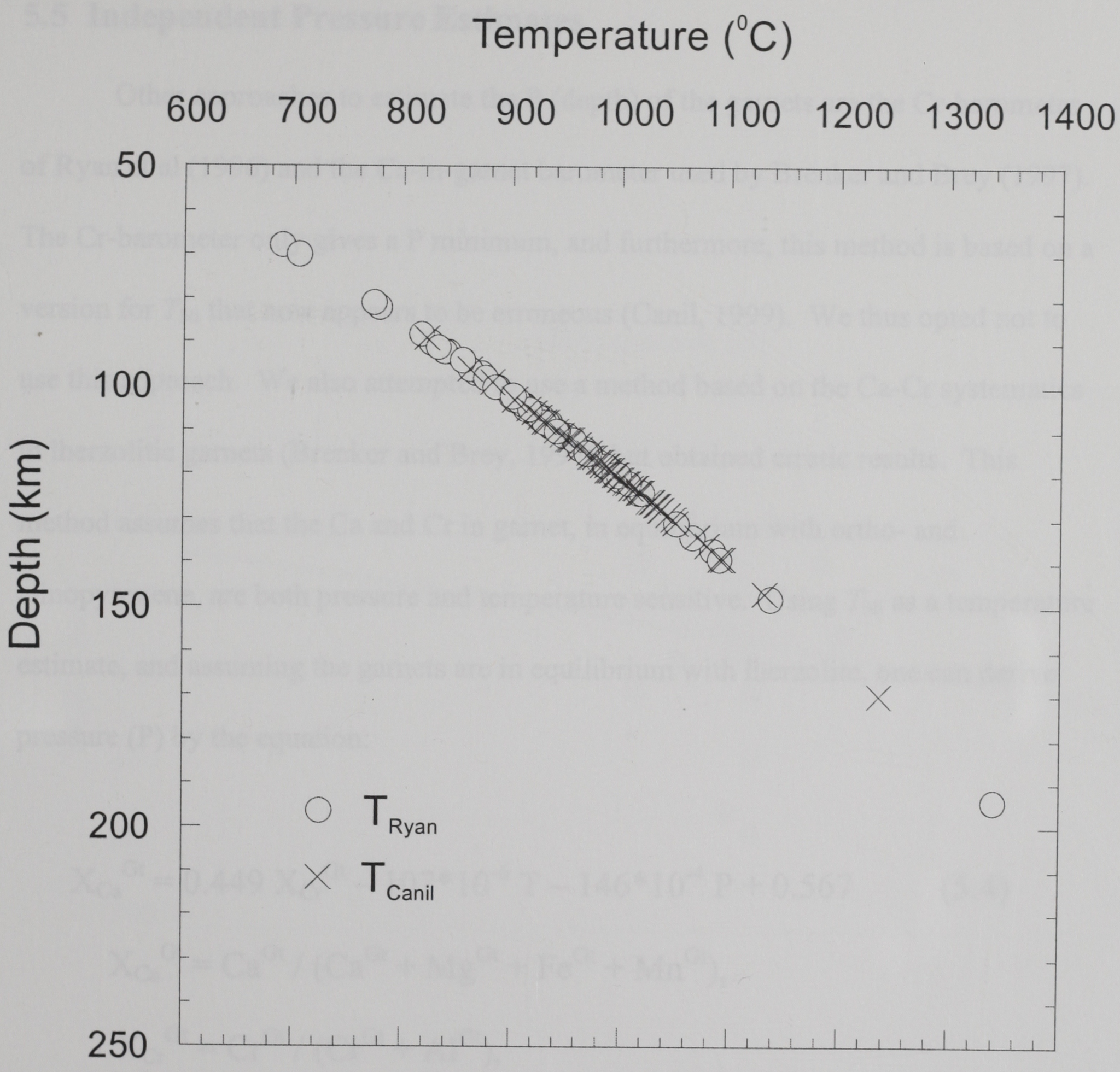

Figure 5.4. Plot of temperature against depth for the empirical calibration (T_{ryan}) and the experimental calibration (T_{Canil}) after Ryan et al (1996) and Canil (1999), respectively. The experimental calibration (Canil, 1999) gives a more limited depth range for a given range of temperatures derived by the Ni-in-garnet geothermometer.

5.5 Independent Pressure Estimates

Other approaches to estimate the P (depth) of the garnets are the Cr-barometer of Ryan et al (1996) and the Ca-in-garnet barometer used by Brenker and Brey (1997). The Cr-barometer only gives a P minimum, and furthermore, this method is based on a version for T_{Ni} that now appears to be erroneous (Canil, 1999). We thus opted not to use this approach. We also attempted to use a method based on the Ca-Cr systematics in lherzolitic garnets (Brenker and Brey, 1997), but obtained erratic results. This method assumes that the Ca and Cr in garnet, in equilibrium with ortho- and clinopyroxene, are both pressure and temperature sensitive. Using T_{Ni} as a temperature estimate, and assuming the garnets are in equilibrium with lherzolite, one can derive pressure (P) by the equation:

$$X_{Ca}^{Gt} = 0.449\, X_{Cr}^{Gt} - 107*10^{-6}\, T - 146*10^{-4}\, P + 0.567 \qquad (5.4)$$

$$X_{Ca}^{Gt} = Ca^{Gt} / (Ca^{Gt} + Mg^{Gt} + Fe^{Gt} + Mn^{Gt}),$$

$$X_{Cr}^{Gt} = Cr^{Gt} / (Cr^{Gt} + Al^{Gt}),$$

where T = temperature (°K), derived from T_{Ni}, P = pressure in GPa, and Fe = Fe^{2+}.

Using this approach very inconsistent P values were obtained based on the Ca-Cr in these garnets, with some garnets projecting near a reasonable geotherm, but most far removed (Figure 5.5). One possible reason for the erratic P_{Ca} results is that, as will be shown below, most of our garnets were not in equilibrium with a lherzolitic assemblage containing coexisting orthopyroxene and clinopyroxene. In this case, Ca

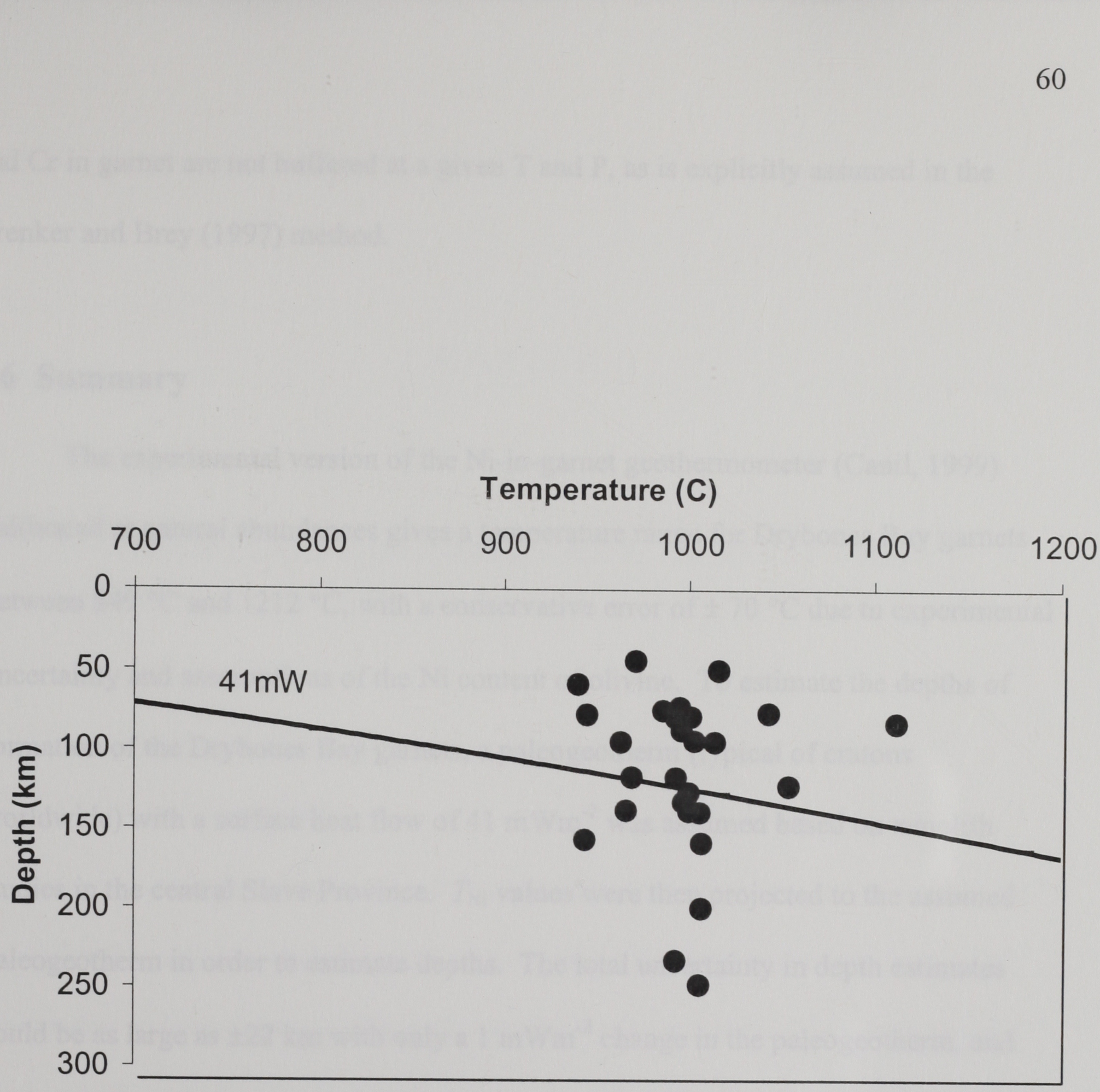

Figure 5. 5 Plot of T_{Ni} in garnet (Canil, 1999) against P_{Ca} in garnet (Brenker and Brey, 1997). The 41 mW geotherm is included (solid line). Most of the garnets give erratic results, far removed from the geotherm.

and Cr in garnet are not buffered at a given T and P, as is explicitly assumed in the Brenker and Brey (1997) method.

5.6 Summary

The experimental version of the Ni-in-garnet geothermometer (Canil, 1999) calibrated at natural abundances gives a temperature range for Drybones Bay garnets between 849 °C and 1212 °C, with a conservative error of ± 70 °C due to experimental uncertainty and assumptions of the Ni content of olivine. To estimate the depths of formation of the Drybones Bay garnets, a paleogeotherm (typical of cratons worldwide) with a surface heat flow of 41 mWm^{-2} was assumed based on xenolith studies in the central Slave Province. T_{Ni} values were then projected to the assumed paleogeotherm in order to estimate depths. The total uncertainty in depth estimates could be as large as ±22 km with only a 1 mWm^{-2} change in the paleogeotherm, and hence the depth estimates are principally used to look at a "relative" stratigraphy of the garnets. Attempts at deriving independent pressures (or depths) of formation of the Drybones Bay garnets, based on their Ca-Cr contents, gave results that were inconsistent and erratic.

CHAPTER 6

MANTLE PROCESSES AND STRUCTURE

6.1 Cratonic Evolution

Research regarding the origin and nature of the deep-seated rocks that exist in the lithosphere beneath cratons has helped us to understand the process of craton stabilization and the existence of mantle roots beneath continents. Two prevalent theories for the origins of these deep-seated rocks exist. The first school of thought involves the peridotitic component of the mantle forming as a high-pressure residue after extraction of komatiitic and basaltic lavas from the primitive Archean mantle (Boyd, 1989). This process is thought to have occurred above mantle plumes with resultant extrusive rocks exposed in greenstone belts (Hart et al, 1997). The second proposes that the peridotites and eclogites found in continental lithosphere are contemporaneous and both are Archean oceanic lithosphere that has been recycled (de Wit et al, 1992) and underthrust beneath cratons (Helmstaedt and Schulze, 1989). Evidence from the Kaapvaal craton, South Africa shows that processes similar to modern plate tectonics may have been operating in the Archean (de Wit et al, 1992), but

this is a contentious issue. Therefore the rocks found beneath cratons could be the result of the subduction and stacking of oceanic lithosphere beneath these early continental nuclei (Helmstaedt and Schulze, 1989).

Many recent geophysical and geochemical studies have attempted to constrain the origins of the lithospheric mantle beneath the Slave craton (MacKenzie and Canil, 1999; Bostock, 1997; Bostock, 1998; Kopylova et al, 1998; Cook et al, 1998; Bostock and Cassidy, 1997; Griffin et al, 1999a; Hoffman, 1990). From this work there seems to be a consensus that the origin of the mantle lithosphere beneath the Slave craton shows broad scale layering, possibly as a result of the subduction and subsequent stacking of oceanic lithosphere. Both geophysical and petrological studies in the central part of the Slave confirm the existences of unique rheological layers in the mantle lithosphere at these locations (Bostock, 1998; Kopylova et al, 1998). The results from this study on the craton edge can be used to confirm that such a structure could possibly extend outward from the central craton. The interpretations represented here can also be used to ground truth observations from a plethora of nearby geophysical investigations on the Slave lithosphere at the craton edge.

6.2 Lithospheric Geometry and Thickness

Electrical (Jones and Ferguson, 1997) and seismic studies (Bostock, 1998) verify that the electrical and seismic lithosphere at the southwest edge of the Slave craton is as much as 200 km thick. Our petrologic estimate is less, with a lithospheric thickness of 164 km. This is, however, a minimum estimate, and could be much more because the lithosphere is likely not less than 160 km since diamonds are present in

Drybones Bay kimberlite. If the assumed paleogeotherm is changed by only 1 mWm^{-2}, the depth estimates that were derived previously in Chapter 5 could be changed by as much as 4-7 km (Figure 5.2). Therefore, if a 39 mWm^{-2} geotherm were assumed, the petrologic lithospheric thickness would be closer to electrical and teleseismic estimates. Petrological estimates would also be closer if the empirical calibration of T_{Ni} (Ryan et al, 1996) is used since this calibration gives a larger depth range for the same samples, although this calibration is thought to be erroneous (Canil, 1999).

In addition to uncertainties from temperature and depth estimates, there is also the added difficulty of comparing geophysical estimates of the lithosphere against petrologic estimates. The seismic lithosphere is based on seismic wave velocities, and hence interprets rock densities as a function of temperature or composition. Electrical methods locate the lithosphere-aesthenosphere boundary based on a transition in transport properties. Petrological estimates of the extent of the lithosphere are provided by mantle samples that impart limits based on the depths of origin of the deepest samples.

Furthermore, assuming that petrologic, electrical and teleseismic methods are all giving depth estimates for the same lithosphere, we are comparing lithosphere thickness at the time of kimberlite emplacement at 450 Ma to the lithosphere today beneath Drybones Bay. The geometry and nature of the cratonic lithosphere beneath the southwest Slave could have changed drastically since the Ordovician, which would make the entire comparison invalid. However, if we assume cratons in general are stable since the Archean, combined with surface geology on and surrounding the Slave craton which indicates stability since before the Ordovician (Isachsen and Bowring,

1994), it is possible to assume that the Slave craton was stable during the time of eruption of the Drybones Bay kimberlite. The youngest supracrustal rocks in the Slave Province are a 2.59 Ga deformed conglomerate from the Anialik River greenstone belt (Villeneuve et al, 1993), and post-tectonic granites dated at 2.59-2.56 Ga are the youngest plutonic rocks found (King et al, 1992). This implies that no substantial thickening or thinning of the craton has occurred since that time (Isachsen and Bowring, 1994), so it is not unreasonable to compare our results from the Ordovician with those found today since there is no evidence for Ordovician sedimentary sequences anywhere in or around the Slave from rifting and/or denudation of the Slave lithosphere.

Considering the largest possible errors in our depth estimates, it is apparent that the lithosphere beneath Drybones Bay was at least 160 km thick in the Ordovician. If we assume the Slave craton was stable since the time of eruption of the Drybones Bay kimberlite and there has been no apparent thinning of the mantle lithosphere beneath the Slave craton since, the geometry of the craton does not thin from the center of the craton (MacKenzie and Canil, 1999; Boyd and Canil, 1997; Kopylova et al, 1999) towards the edge.

6.3 Trace Element Systematics In Garnet

Trace element systematics in garnet are used as a proxy to estimate the geochemistry and mineralogy of the mantle lithosphere as a function of depth beneath Drybones Bay. In order to use the geochemistry of single garnet grains as a means to characterize the lithosphere, it is first instrumental to establish how other peridotite minerals partition trace elements with garnet. The partitioning of trace elements

between garnet and other mantle phases can then be used as a framework to interpret the geochemistry of single garnets, and to separate out the mineralogical control on trace element systematics from temperature and pressure effects. Limited published work on $D^{gt/cpx}$ (Zack et al, 1997; Stachel et al, 1998) and the garnet-clinopyroxene pairs from this study afford an opportunity to examine $D^{gt/cpx}$ for many trace elements, and to refine interpretations based on the trace element systematics recorded in the Drybones Bay garnets.

Both garnet and clinopyroxene are the major hosts for incompatible trace elements in peridotites, and the partitioning of trace elements between these two phases will therefore be most important. The partitioning of trace elements between garnet and clinopyroxene is dependent on temperature, pressure and modal abundance (Zack et al, 1997). For the purposes of this study, garnet and clinopyroxene are assumed to be the only phases that contain trace elements in any significant quantity, and the partitioning of trace elements will be considered only between theses two phases.

Distribution coefficients ($D^{gt/cpx}$) have been calculated for several trace elements in four garnet-clinopyroxene pairs from this study. These four pairs from a total of nine in the study were chosen because they have values above detection for most of the trace elements under consideration (Figure 6.1). These samples show that Ni and Nb through to Sm preferentially partition into clinopyroxene, whereas Zr, Y, the HREE and Sc partition preferentially into garnet. Both Hf and Ga partition about equally. Garnet preferentially partitions U relative to Th and Nb, and Sc relative to V. These results are similar to those of Zack et al (1997), albeit at slightly lower $D^{gt/cpx}$ values (Figure 6.1).

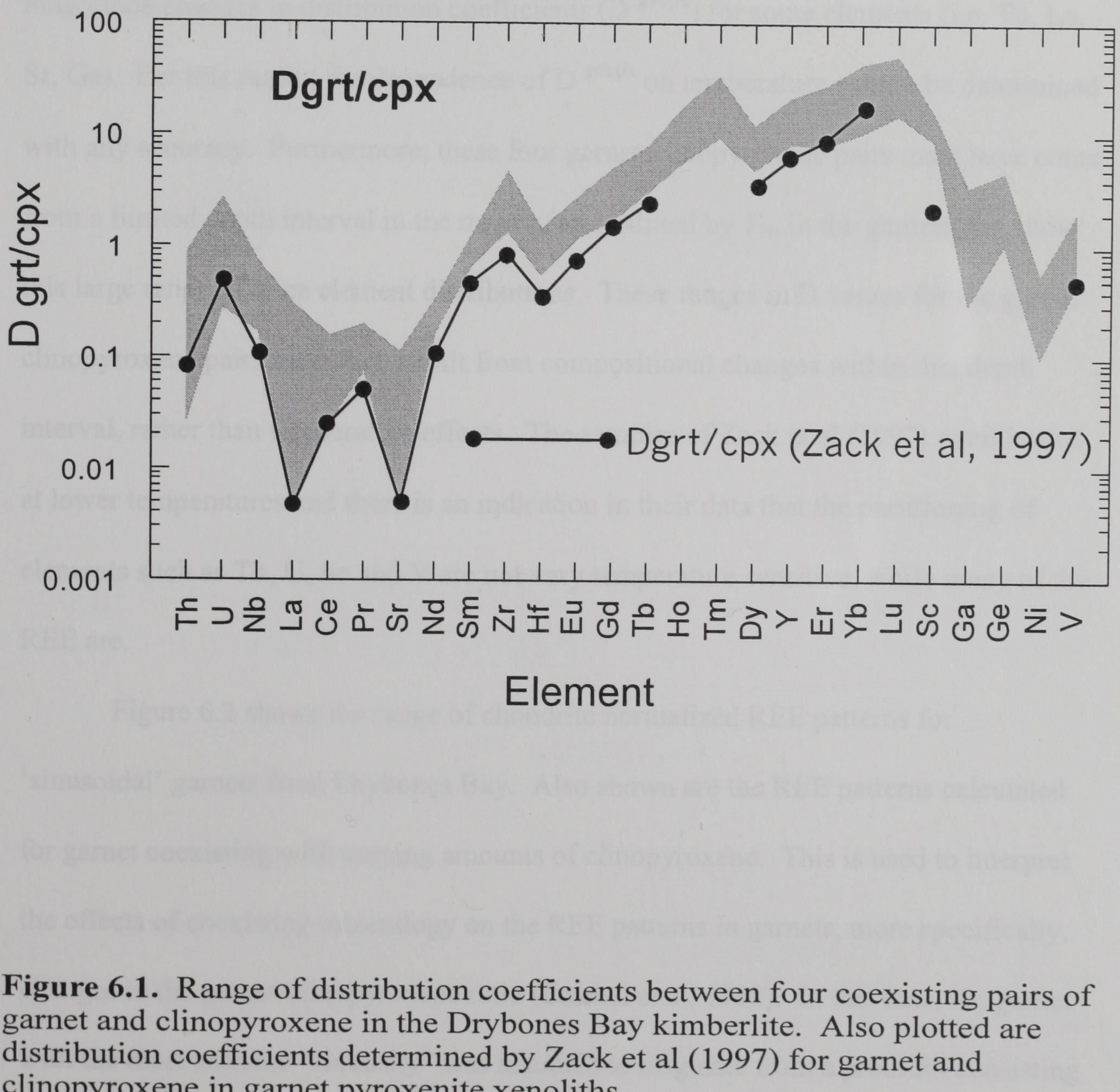

Figure 6.1. Range of distribution coefficients between four coexisting pairs of garnet and clinopyroxene in the Drybones Bay kimberlite. Also plotted are distribution coefficients determined by Zack et al (1997) for garnet and clinopyroxene in garnet pyroxenite xenoliths.

It is important to note that $D^{gt/cpx}$ is likely dependent upon pressure, temperature and bulk composition, and the relationship between these variables and the trace element patterns seen in both the garnets and clinopyroxenes must be established. The four garnet-clinopyroxene pairs have a limited range in temperatures of only 30°C, so temperature effects cannot be significant and they cannot explain the order of magnitude changes in distribution coefficients ($D^{gt/cpx}$) for some elements (i.e. Th, La, Sr, Ga). For this reason the dependence of $D^{gt/cpx}$ on temperature cannot be determined with any accuracy. Furthermore, these four garnet-clinopyroxene pairs must have come from a limited depth interval in the mantle, as confined by T_{Ni} in the garnets, yet show this large range of trace element distributions. These ranges in D values for the garnet-clinopyroxene pairs must then result from compositional changes within this depth interval, rather than temperature effects. The samples of Zack et al (1997) equilibrated at lower temperatures and there is an indication in their data that the partitioning of elements such as Th, U, Sc and V are not very temperature sensitive, while many of the REE are.

Figure 6.2 shows the range of chondrite normalized REE patterns for 'sinusoidal' garnets from Drybones Bay. Also shown are the REE patterns calculated for garnet coexisting with varying amounts of clinopyroxene. This is used to interpret the effects of coexisting mineralogy on the REE patterns in garnets, more specifically, changes in the garnet-clinopyroxene ratio (Stachel et al, 1998). In this case, the garnet with the most extreme "sinuosity" was assumed to originate from a protolith consisting exclusively of garnet, and is plotted as the 1:0 (garnet/clinopyroxene ratio) line in Figure 6.2. Using $D^{gt/cpx}$ values from Zack et al (1997), lines are drawn representing

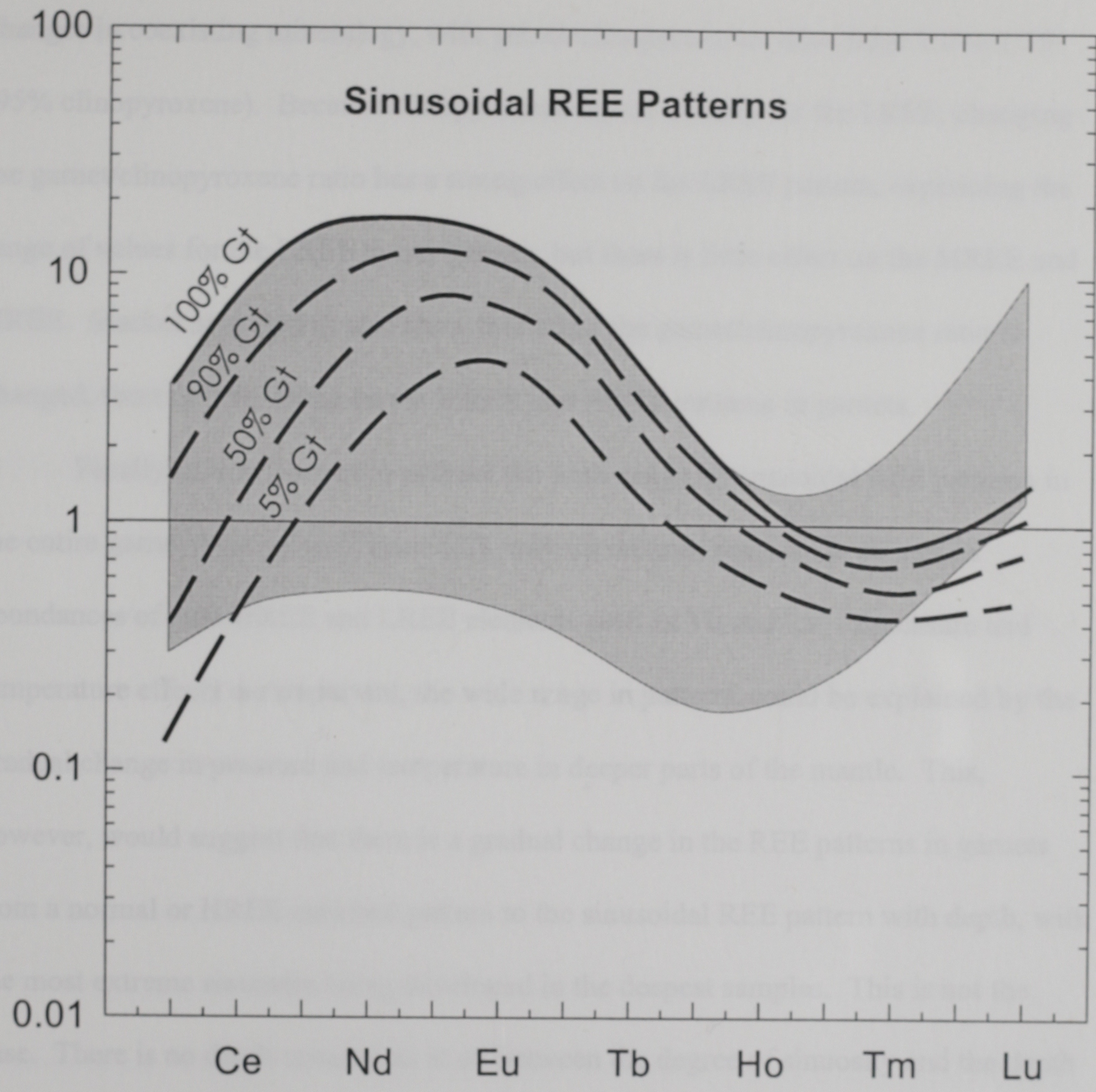

Figure 6.2. Plotted is the range of chondrite normalized REE patterns for sinusoidal garnets. Also shown are the REE patterns calculated for garnet coexisting with varying amounts of clinopyroxene. The amount of clinopyroxene that coexists with garnet will have an effect on the distribution of trace elements between these two phases, and will hence affect the sinusoidal trace element pattern.

changes in coexisting mineralogy, with garnet/clinopyroxene ratios from 1:0 to 1:19 (95% clinopyroxene). Because clinopyroxene has an affinity for the LREE, changing the garnet/clinopyroxene ratio has a strong effect on the LREE pattern, explaining the range of values for the LREE in our garnets, but there is little effect on the MREE and HREE. Stachel et al (1998) also show that when the garnet/clinopyroxene ratio is changed, there is little effect on the MREE and HREE patterns in garnets.

Finally, it is important to address the wide range in sinusoidal REE patterns in the entire garnet population (Figure 6.2), with an order of magnitude change in abundances of both HREE and LREE elements such as Yb and La. If pressure and temperature effects are important, the wide range in patterns could be explained by the gradual change in pressure and temperature in deeper parts of the mantle. This, however, would suggest that there is a gradual change in the REE patterns in garnets from a normal or HREE enriched pattern to the sinusoidal REE pattern with depth, with the most extreme sinuosity being developed in the deepest samples. This is not the case. There is no depth correlation at all between the degree of sinuosity and the depth of recovery. There is, however, an abrupt change from 'normal' to 'sinusoidal' garnets at an approximate depth of 120 km (Figure 5.2). Thus, pressure and temperature effects do not change the degree of sinuosity in the garnet population. Instead, some kind of discontinuity could account for profound changes in the garnet trace element pattern over a limited depth interval. However, once again we must be very cautious with the spatial interpretation of the results. As mentioned previously, with all of the uncertainty that is associated with the final depth estimates, the garnet xenocrysts that comprise a large set of the sampled population could have in principle originated from the same

disaggregated larger crystal. Although, such a crystal with such a range in trace element distributions was not found amongst the 42 garnets in this study, including the xenolith samples. The varying degrees of sinuosity within the garnet population could be accounted for by zonation in a few linked samples from a similar protolith (e.g. Griffin et al, 1999). Further caution must also be taken under consideration because the change from 'normal' to 'sinusoidal' garnets is marked by only four 'normal' samples. Distinct petrographic differences in the 'normal' xenolith samples and the single 'normal' xenocryst make it possible to assume that these samples were not derived from the same source. Unfortunately the small number of 'normal' samples along with the uncertainty in the 'sinusoidal' population warrants some doubt to the relative depths of origin of the samples studied.

6.4 Carbonatite Metasomatism

The cause of the sinusoidal REE pattern in garnets is commonly attributed to metasomatism, with carbonatite being a favourable fluid for such effects (Stachel et al, 1998; Sweeney et al, 1995; Dautria et al, 1992; Rudnick et al, 1993; Norman, 1998; Ionov, 1998; Ionov et al, 1993; Griffin et al, 1999b; Hauri et al, 1993). A carbonatitic fluid would have a high LREE/HREE ratio and high Sr content, with depletion in Zr and Hf (Ionov et al, 1993), and can account for sinusoidal trace element patterns in garnets that have reacted with the fluid (Stachel et al 1998; Hoal et al, 1994). The sinusoidal pattern arises from carbonatitic metasomatism of garnet that has previously been depleted by partial melting processes in the upper mantle. Disequilibrium effects (with the carbonatitic melt) cause the LREE in garnets to adjust faster than the HREE to

the enriching melt possibly because of differences in diffusion rates for the rare earth elements in garnet (Hoal et al 1994). Results from Stachel et al (1998) and Hoal et al (1994) show REE patterns in garnet that are very similar to patterns seen in Figure 4.5, implying that the lithospheric mantle below Drybones Bay has reacted with a carbonatite melt, and has subsequently suffered a similar metasomatism.

Furthermore, in the Drybones Bay sample set there is a large population of wehrlitic garnets (Figure 4.3), which shows that clinopyroxene is present in varying abundance in the lithospheric mantle at this location. The fact that there are so many wehrlitic garnets in the sample set could be interpreted as a direct consequence of carbonatite metasomatism (Sweeney et al, 1995), along with the high Sr content of the garnets. The clinopyroxene can form from the interaction of a carbonatite with a harzburgitic assemblage, where orthopyroxene is converted to clinopyroxene (Norman, 1998), and as a result, garnets become wehrlitic since they are then equilibrating with a clinopyroxene-rich assemblage. As was stated above, this increase in clinopyroxene could be a direct cause of the sinusoidal nature of many garnets, but this only affects the LREE and does not explain the other elements in the pattern.

In this light, geochemical signatures of clinopyroxenes from Drybones Bay should also provide evidence of metasomatism. For comparison, trace element data from Ionov (1998) and Norman (1998) for clinopyroxenes that show strong evidence for carbonatite metasomatism are compared to clinopyroxene data from Drybones Bay (Figure 4.6). The trace element patterns match well, with the exception of a few elements such as Yb and Nb. The discrepancy in these elements is explained by the fact that clinopyroxene samples from Ionov (1998) and Norman (1998) are in equilibrium

with spinel and not garnet, and coexisting spinel would favorably partition Nb. The results of this comparison also strongly favour carbonatite metasomatism as the means by which the majority of garnets from the Drybones Bay kimberlite have obtained a sinusoidal REE signature.

What must also be addressed is the possibility that the garnet/clinopyroxene pairs studied here have come from the same xenolith, or in the most pessimistic case, even the same xenocryst pair. If we consider the uncertainties in T_{Ni} along with the further uncertainty in the paleogeotherm estimate it is easily conceivable that all four samples equilibrated at the same depth in the lithosphere. The possible error introduced by the temperature and depth estimates makes it difficult to determine with any confidence a spatial relationship with these samples. The differences in the REE patterns could simply be explained by a disaggregated xenocryst that was originally zoned and the rims differed compositionally from the cores due to disequilibrium with the metasomatizing fluid, but no such crystal was in any other sample studied.

The significant geochemical and petrological anomaly located at an estimated depth of 120 km, below which garnet type and chemistry changes, requires explanation. All of the garnets below the 120 km depth are 'sinusoidal' and are interpreted to have undergone carbonatite metasomatism. The critical depth of 120 km could be the extent to which the carbonatitic fluid penetrated upward, leaving behind an unaltered lithology at shallower depths that is distinctly different both in major and trace element characteristics compared to underlying mantle that was metasomatized. The plausibility of this interpretation becomes more evident when the depth uncertainties are

considered, but it remains unclear why an upward percolating metasomatic front would be impeded at this particular depth interface.

6.5 Mantle Lithosphere Structure

The presence of a thick cratonic root beneath southwest Slave Province as predicted by petrologic and geophysical studies is consistent with the presence of diamonds in the Drybones Bay kimberlite, but does not explain the geochemical anomalies that have been encountered in the garnet population. The discrete depth at which the REE patterns in the garnet population change from 'normal' to 'sinusoidal' is also reflected in other trace element ratios. The Nb/Th (Figure 6.3A), Ce/Yb (Figure 6.3B), Th/U (Figure 6.3C), Zr/Y (Figure 6.3D), Yb/Ga (Figure 6.3E) and Y/V (Figure 6.3F) ratios in garnet versus depth all show a distinct change around 120 km. The 'normal' garnets all plot above the 120 km depth (critical depth), and the change in trace element ratios does not increase gradually with depth, but rather show sudden and erratic changes once the 120 km depth is encountered. All of the plots of depth versus trace element ratios show a clustering of points at the critical depth, as well as the presence of 'normal' garnets at the shallowest depths. Another possibility to be considered in the explanation of the geochemical anomaly seen at the 120 km depth is the structural juxtaposition of two different lithologies in the mantle lithosphere beneath Drybones Bay, across the critical depth. Bostock (1998) has published teleseismic results from ~50 km north of Drybones Bay that reveal a similar change in lithology in the lithosphere at an approximate depth of 120 km, which he refers to as the *X* discontinuity (Figure 6.5). Bostock (1998) believes the discontinuity to be of structural

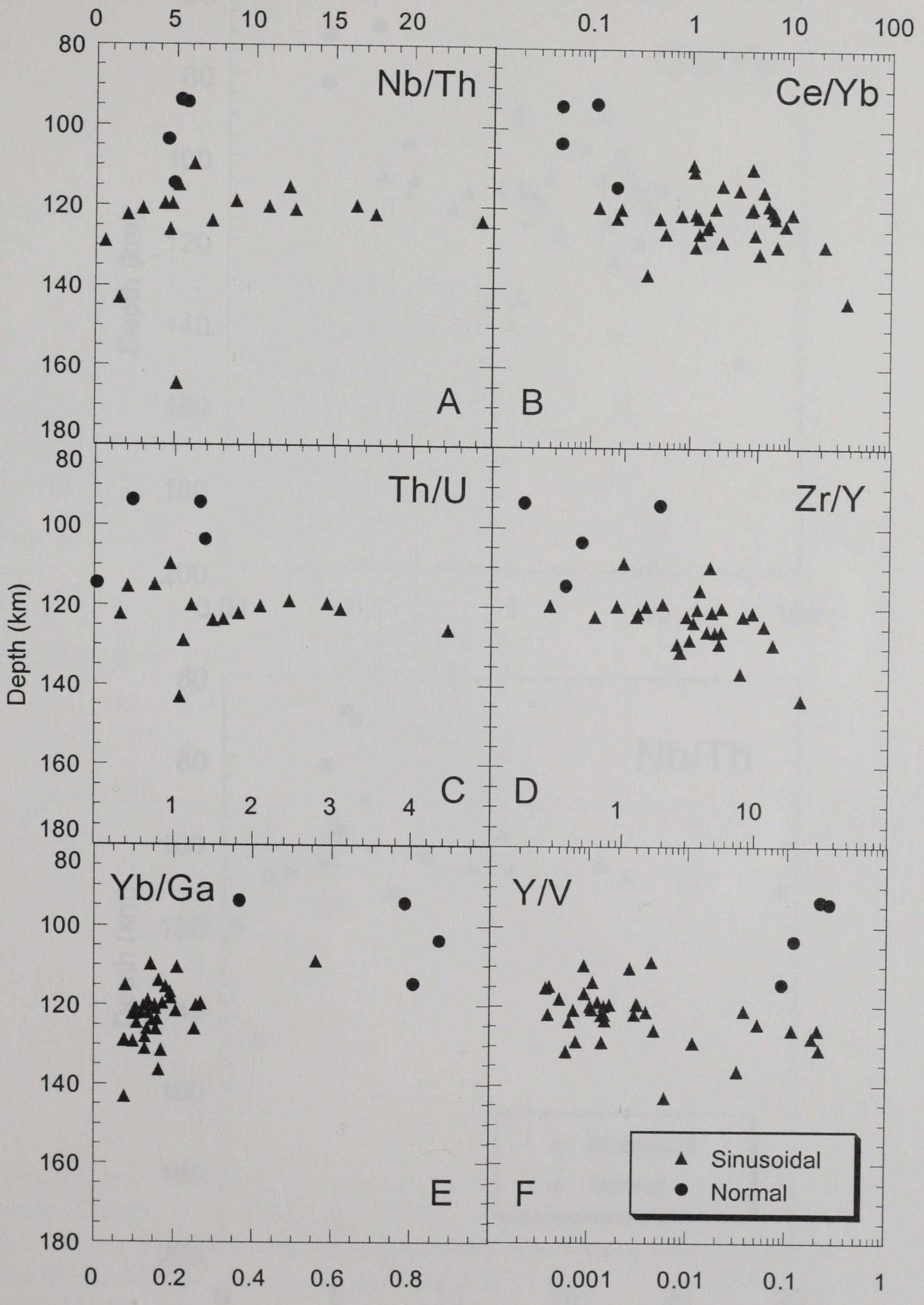

Figure 6.3. Trace element ratios plotted against depth for Drybones Bay garnets. S-Shaped samples are the "sinusoidal" garnets and HREE samples are the "normal" garnets. It is important to note that not all samples (n=42) are seen in every plot (A-F) because in some samples one or both of the elements in the plotted ratio were below the detection limits of the LAM-ICP-MS.

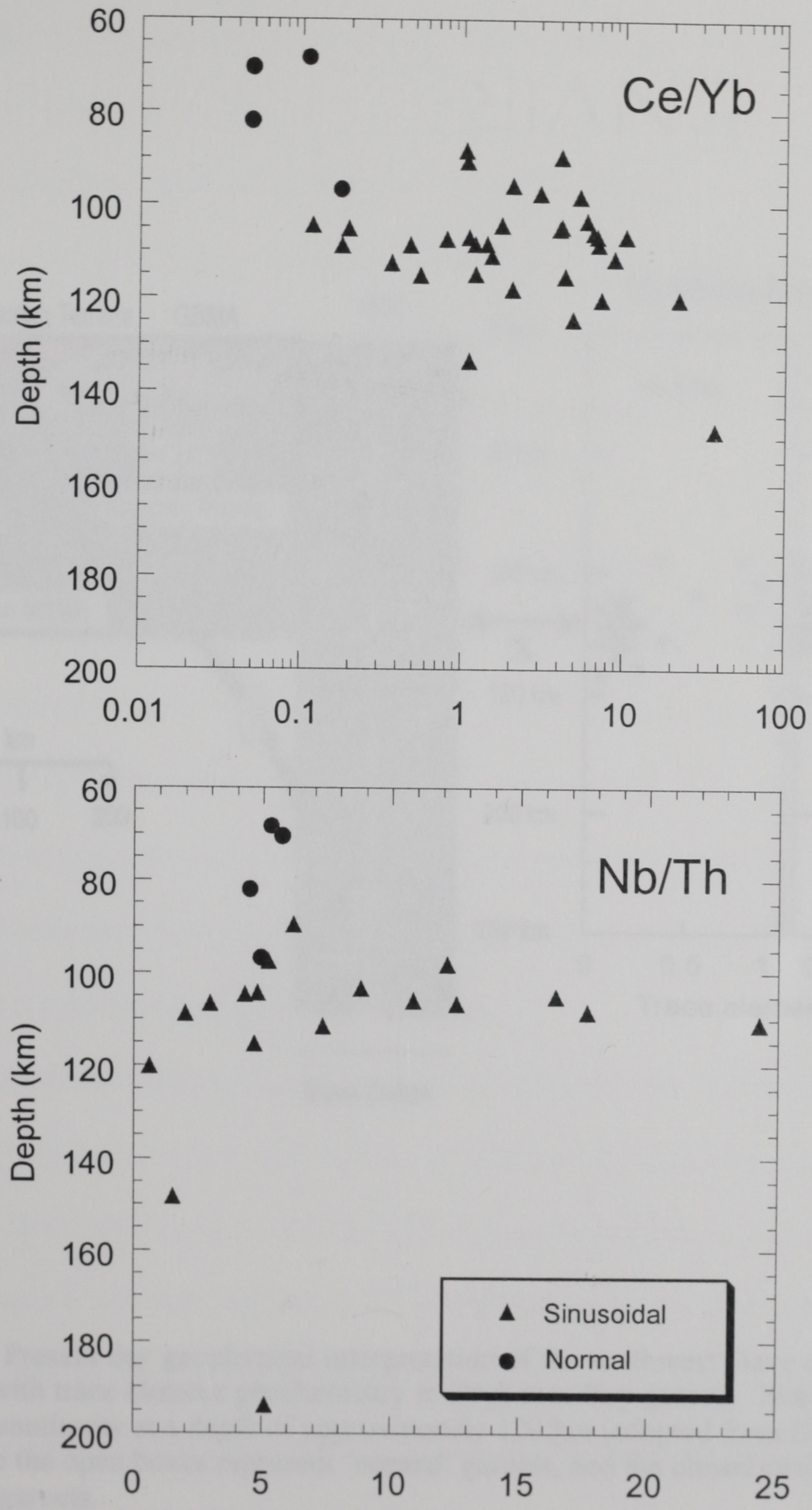

Figure 6.4. Trace element ratios plotted against depth for temperatures and depths derived from the empirical calibration of the Ni-in-garnet geothermometer (Ryan et al, 1996). This calibration increases the range in depth between samples and would estimate that the deepest sample was derived from 194 km, and the shallowest at 68 km.

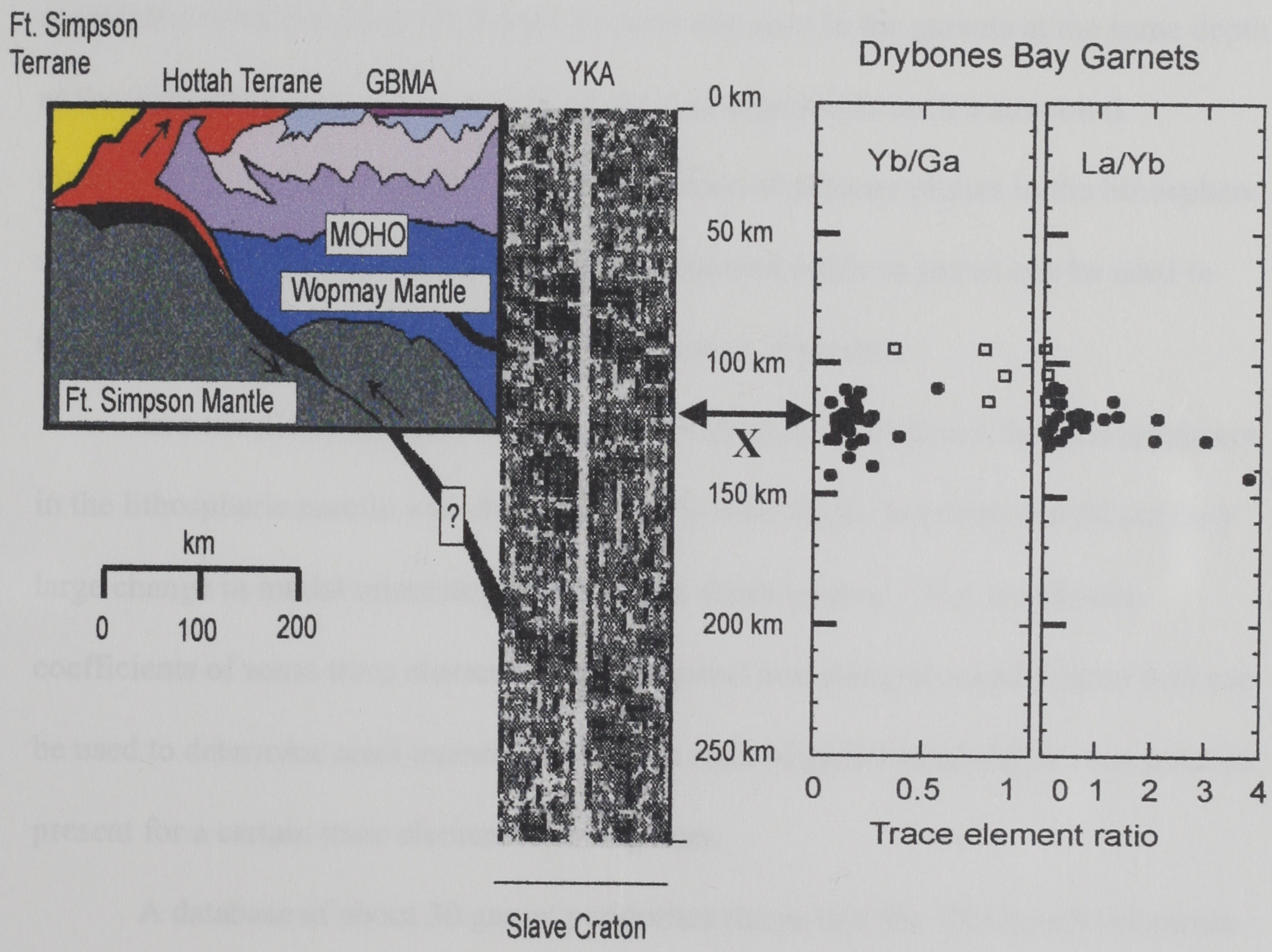

Figure 6.5. Present day geophysical interpretation of the southwest Slave craton and correlation with trace element geochemistry in Drybones Bay garnets. Note the location of the X-discontinuity at a depth of approximately 120 km (adapted from Bostock, 1998). In this figure the open boxes represent 'normal' garnets, and the closed circles represent 'sinusoidal' garnets.

origin, resulting from the subduction and subsequent stacking of different slabs of lithosphere beneath the ancient craton. Multiple layers mark the *X* discontinuity over a 30 km depth interval (Bostock, 1998). The presence of such a structural discontinuity is consistent with the sudden variations in chemistry seen in the garnets at the same depth as the *X* discontinuity. Any large lithological change across such a structural discontinuity should be apparent in the abundance of primary phases in the lithosphere, such as garnet and clinopyroxene. The trace element ratios in garnet can be used to investigate the nature of such a lithological change, if present.

In a mantle of constant composition the abundance of garnet and clinopyroxene in the lithospheric mantle will change gradually with depth, but there should not be a large change in modal mineralogy over a short depth interval. The distribution coefficients of some trace elements between garnet and clinopyroxene (Figure 6.1) can be used to determine semi-quantitatively what ratio of garnet to clinopyroxene must be present for a certain trace element ratio in garnet.

A database of about 30 garnet peridotites shows that the Yb/Ga ratio of garnet peridotite is about 0.12 (Frey et al, 1985), and changes very little with degree of depletion. We adopt this same ratio for typical garnet peridotite and calculate how the change in garnet/pyroxene ratio changes the Yb/Ga in garnet coexisting with clinopyroxene. In this calculation, all the Yb and Ga in the peridotite is assumed to be contained in garnet and clinopyroxene, and the distribution coefficients ($D^{gt/cpx}_{Yb}$ and $D^{gt/cpx}_{Ga}$) shown in Figure 6.1 were used:

$$(Yb/Ga)_{gt} = (0.12)_{bulk\ rock} \cdot (D^{gt/cpx}_{Yb} / D^{gt/cpx}_{Ga}) \cdot (X_{cpx} / X_{gt}) \qquad (6.1)$$

where $D^{gt/cpx}_{Yb}$ and $D^{gt/cpx}_{Ga}$ are the distribution coefficients between garnet and clinopyroxene of Yb and Ga respectively, and X_{gt} and X_{cpx} are the fractions of garnet and clinopyroxene respectively in the bulk rock. The results of the calculation are shown in Figure 6.6, along with the range of $(Yb/Ga)_{gt}$ in Drybones Bay garnets. This ratio in garnet changes from ~ 0.4 to 0.9 above 120 km and drops to as low as 0.1 below. Values for $(Yb/Ga)_{gt}$ above 120 km are consistent with a garnet/cpx ratio of 6 to 10, but below 120 km there is a very profound change in the ratio of 20 to 40. A similar trend can be seen in any trace element ratio in the Drybones garnets in which one element (e.g. Yb) is far more compatible in garnet relative to clinopyroxene, than another element (e.g. Ga – see Figure 6.1). Thus, the trace element ratios and REE patterns are consistent with a change across the 120 km depth from a peridotite containing relatively large amounts of clinopyroxene and retaining a 'normal' (HREE-enriched) trace element pattern, to a peridotite containing less clinopyroxene and garnets that have a 'sinusoidal' trace element pattern.

In order to scrutinize the possibility of a changing lithology across the 120 km depth the garnet samples were re-plotted using Ca and Cr cations as axes (Figure 6.7). This plot shows two distinct groupings in the garnet population that lie upon two different trends. The upper trend contains generally more calcic garnets, whereas the lower trend contains a relatively less calcic distribution of garnets. Figure 6.6 shows that the upper trend hosts the 'normal' garnet population, and these 'normal' garnets are seen exclusively in the xenolith samples and one xenocryst. Petrographic evidence shows the likely existence of clinopyroxene in these samples due to small grains sizes (Boyd and Mertzman, 1987) for pseudomorphed pyroxene grains. These lower

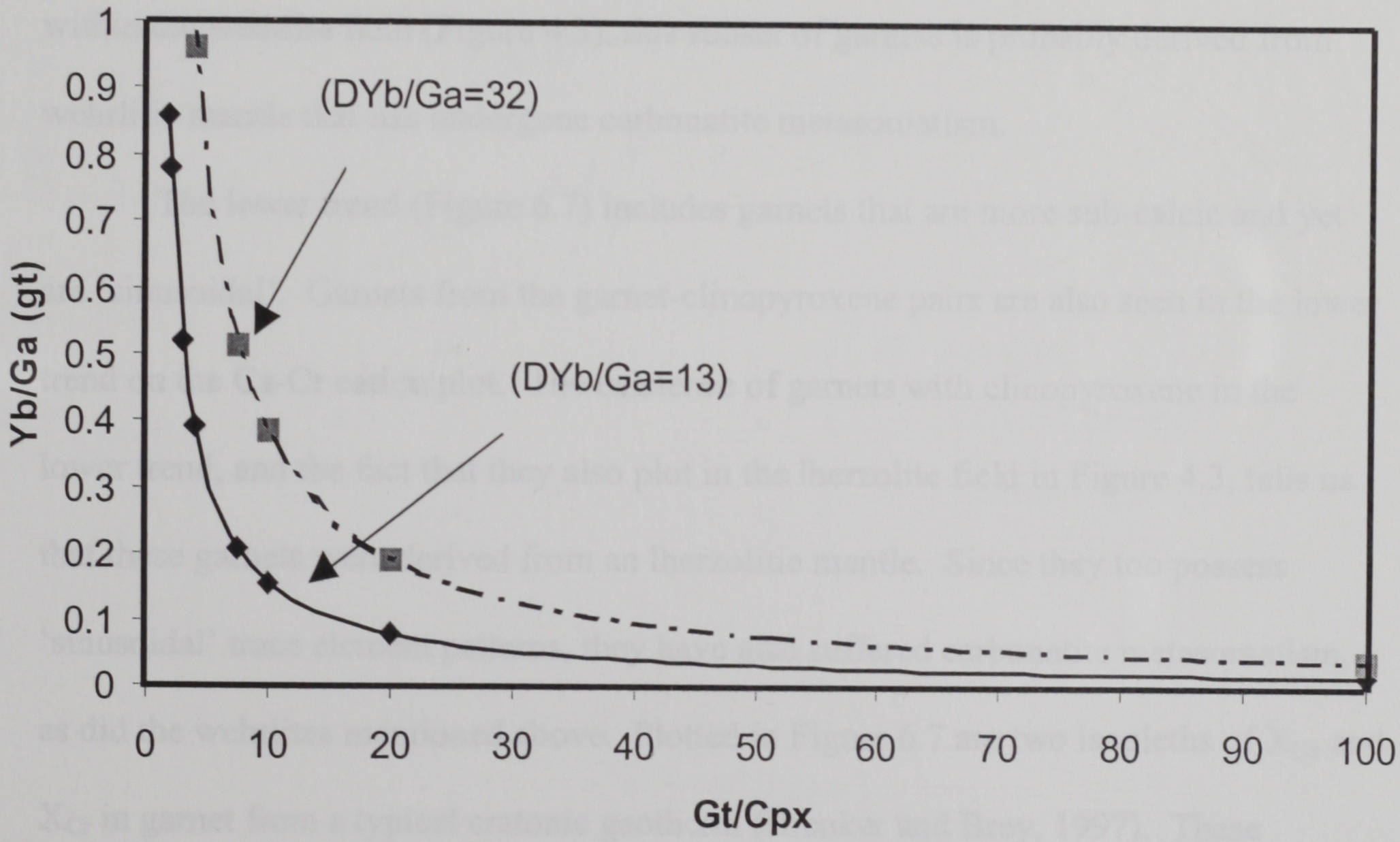

Figure 6.6. Plot of Yb/Ga ratio in garnet against garnet/clinopyroxene ratio for range of $D^{Yb/Ga}$ values (Figure 6.1) in order to illustrate the increase in Yb/Ga ratio with the increase in garnet in the fictitious mantle.

temperature 'normal' garnets (from T_{Ni}) that are in equilibrium with clinopyroxene are likely the only wehrlitic samples that are seen in the sample set that have not been metasomatized.

The upper trend (Figure 6.7) is more dominated by garnets that have been metasomatized, and which are single xenocryst samples. This group is high in calcium but have a 'sinusoidal' trace element pattern. From this, and the fact that they plot within the wehrlite field (Figure 4.3), this subset of garnets is probably derived from wehrlitic mantle that has undergone carbonatite metasomatism.

The lower trend (Figure 6.7) includes garnets that are more sub-calcic and yet are 'sinusoidal'. Garnets from the garnet-clinopyroxene pairs are also seen in the lower trend on the Ca-Cr cation plot. The existence of garnets with clinopyroxene in the lower trend, and the fact that they also plot in the lherzolite field in Figure 4.3, tells us that these garnets were derived from an lherzolitic mantle. Since they too possess 'sinusoidal' trace element patterns, they have also suffered carbonatite metasomatism, as did the wehrlites mentioned above. Plotted in Figure 6.7 are two isopleths of X_{Ca} and X_{Cr} in garnet from a typical cratonic geotherm (Brenker and Brey, 1997). These isopleths show that if all samples equilibrate along a geotherm the upper wehrlitic trend (trend A) must lie 'structurally' above the lower lherzolitic trend (trend B), since the wehrlitic trend is at relatively lower pressure and temperature conditions. These garnet trends are not well defined in the trace element ratios plotted against depth where the only correlation is in the fact that the 'normal' garnets plot at a depth shallower than the 'sinusoidal' garnets.

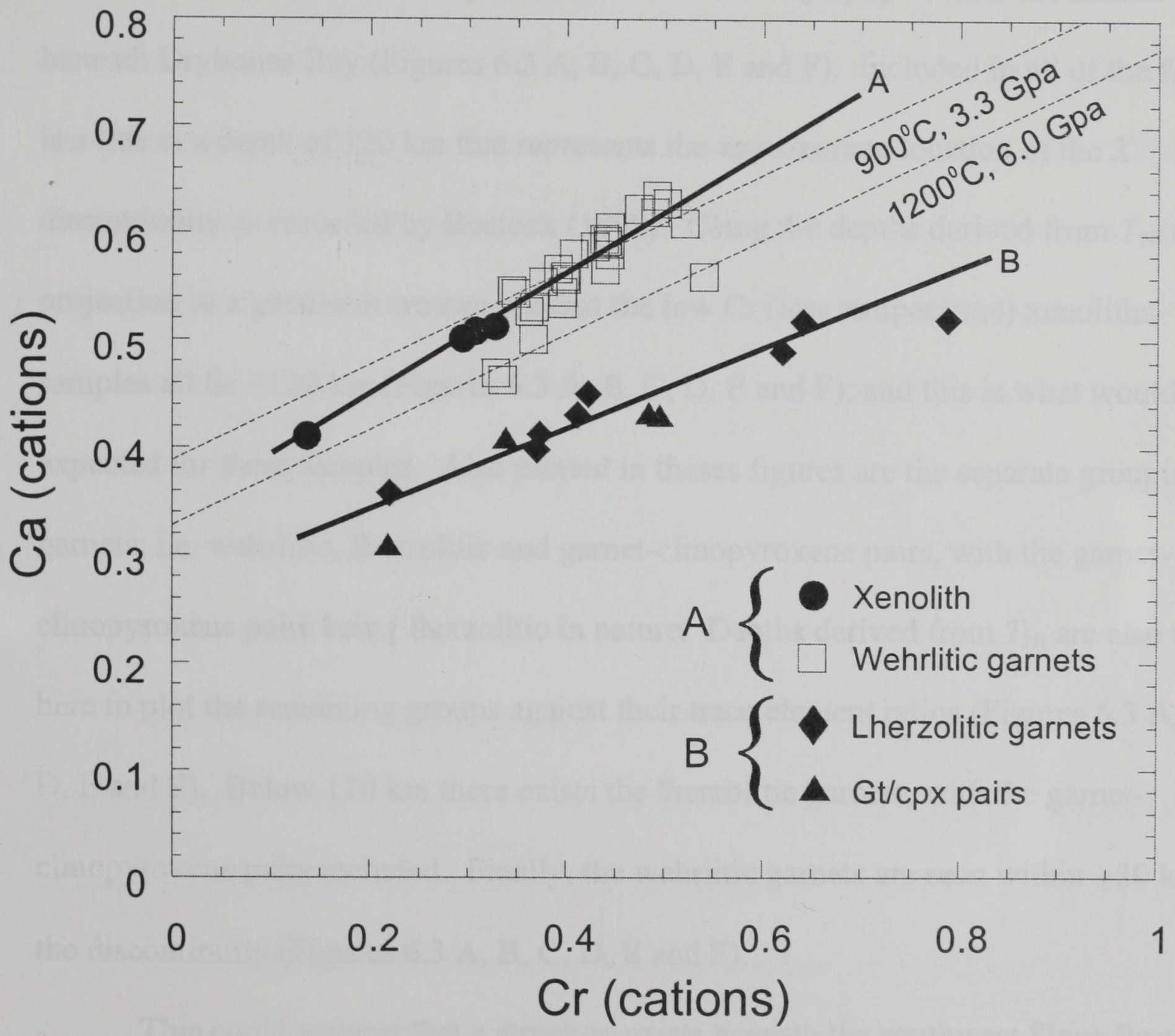

Figure 6.7. Plot of Ca cations versus Cr cations for Drybones Bay garnets. The garnets form two distinct groups on separate trends (A and B). The upper trend (A) is more calcic and likely represents a more wehrlitic source, whereas the lower trend (B) represents a lherzolitic source lithology. Also shown are two isopleths of pressure and temperature for a typical cratonic geotherm (Brenker and Brey, 1997) for a range of Ca and Cr values. This shows that garnets on the A trend must lie above garnets on trend B on a cratonic geotherm.

Furthermore, based on the distinction of the wehrlitic from the lherzolitic garnets (Figures 4.3 and 6.7), these groups of garnets were plotted against depth and trace element ratios in order to interpret their relative "stratigraphy" within the mantle beneath Drybones Bay (Figures 6.3 A, B, C, D, E and F). Included in all of the figures is a line at a depth of 120 km that represents the approximate location of the *X* discontinuity as recorded by Bostock (1998). Using the depths derived from T_{Ni} and projection to a geotherm we can see that the low Cr (low temperature) xenoliths samples all lie <120 km (Figures 6.3 A, B, C, D, E and F), and this is what would be expected for these samples. Also plotted in theses figures are the separate groupings of garnets; i.e. wehrlitic, lherzolitic and garnet-clinopyroxene pairs, with the garnet-clinopyroxene pairs being lherzolitic in nature. Depths derived from T_{Ni} are also used here to plot the remaining groups against their trace element ratios (Figures 6.3 A, B, C, D, E and F). Below 120 km there exists the lherzolitic garnets, with the garnet-clinopyroxene pairs included. Finally, the wehrlitic garnets are seen within ±20 km of the discontinuity (Figures 6.3 A, B, C, D, E and F).

This could suggest that a structure exists beneath the southwest Slave Province that starts with 'normal' wehrlite at the shallowest depth, through metasomatized wehrlite, eventually to a metasomatized lherzolite. The vast range in trace element ratios seen around 120 km in all plots (Figures 6.3 A, B, C, D, E and F) could imply that there isn't a simple transition in lithology with depth, but more than likely several different lithologies are interleaved at a discontinuity, which agrees with the seismological properties of the *X* discontinuity as interpreted by Bostock (1998) and observations of structural and petrologic changes in ophiolites. This could also explain

the fact that in the suite of garnets from Drybones Bay there is no correlation of degree of sinuosity in the metasomatized garnets with depth since many repeating lithologies could possibly exist. The problem with this model is that there are too few 'normal' garnets on which to base the existence of an 'upper layer' of 'normal' unmetasomatized lherzolite. More 'normal' garnets are required to completely confirm the structural discontinuity model. This model also assumes there has been no change in the mantle lithosphere beneath the southwest Slave in the last 450 Ma. Although, this is consistent with surface geology, many other cratons show mantle lithosphere that has been modified by more recent geological events.

6.6 Summary

The trace element systematics in garnet can be used as a proxy to estimate the geochemistry and mineralogy of the mantle lithosphere as a function of depth beneath Drybones Bay. Garnet and clinopyroxene are the major hosts of trace elements in mantle assemblages, so the partitioning of trace elements between these two phases is important. Such information is used to determine the relative modal abundance of each phase from the trace element concentrations in garnet. This, along with other key trace element ratios plotted against depth, tells us that there could exist a geochemically anomaly in the mantle lithosphere beneath Drybones Bay. This anomaly could be interpreted as a transition from 'normal' lherzolite at the shallowest depth, through metasomatized wehrlite, eventually to a metasomatized lherzolite. The metasomatic agent is believed to be a carbonatitic melt that has migrated through the deeper lithologies. This metasomatism can explain the nature of the 'sinusoidal' garnets.

Metasomatism coupled with the possibility that the garnet samples are genetically linked and simply represent zoning in disaggregated xenoliths or xenocrysts could explain the anomalous geochemistry seen throughout the 120 km depth range.

A structural discontinuity at an approximately 120 km depth beneath Drybones Bay recognized in geophysical studies can be correlated to the geochemical anomaly in the Drybones Bay garnets, if depths assumed are correct. An alternative model for this anomaly could be caused by multiple layers of different slabs of lithosphere that have been subducted and subsequently stacked beneath the ancient craton. This stacking of lithosphere is possibly what has imparted the mantle layering that is interpreted to exist beneath the southwest and central Slave Province. In this model, the abrupt change in garnet chemistry with depth is structural in origin, with metasomatized garnet-bearing lithosphere underthrust beneath 'normal' garnet lherzolite. Problems with this model are that it assumes the lithosphere today is identical to that in the Ordovician and that the depth estimates are completely correct. Furthermore, this model would be based on only four 'normal' garnet samples above 120 km, and more would be needed to fully substantiate such a scenario.

CHAPTER 7

CONCLUSIONS

7.1 Lithosphere Thickness

The Drybones Bay kimberlite provides a means of ground-truthing deep seismic interpretations in the southwest Slave Province by acting as a natural 'bore hole' to depths in the mantle that could not otherwise be studied. The Drybones Bay kimberlite pipe is located within the sampling range of nearby (~50 km) teleseismic and electrical study areas that give estimates of lithospheric thickness. These studies indicate that today's lithosphere is close to 200 km thick. Trace element data from garnets indicate that the Ordovician lithosphere beneath Drybones Bay was at least 160 km thick using the Ni-in-garnet geothermometer after Canil (1999). With the possible errors introduced by the methods used for depth estimates, this thickness is only an approximation of the lithospheric thickness beneath the southwest Slave. Comparing today's lithospheric depth estimates with depths in the Ordovician is only valid if it is assumed that the craton has been stable since before the Ordovician. The geology on and surrounding the Slave craton would suggest that the craton has in fact been stable.

7.2 Lithospheric Mantle Structure

Trace element data suggest that there is a change in the lithosphere at a depth of approximately 120 km that is seen in the garnet population (REE patterns) through a change from 'normal' to 'sinusoidal' garnets. A metasomatic fluid such as a carbonatitic melt that has penetrated the lithospheric mantle is a possible explanation for the geochemical change. The anomalous depth of 120 km could mark the extent to which the metasomatizing fluid has penetrated upward in the mantle, leaving the mantle above this depth unchanged by metasomatism. This change in garnet type could also be explained by a change in composition in the mantle at 120 km. A structural juxtaposition could also be used to describe a rapid change in composition in the mantle. Such a structure has been observed and has been expressed as the *X* discontinuity (Bostock, 1998) through geophysical interpretations. By interpreting major and trace element data revealed through Drybones Bay garnets the 120 km depth in the mantle lithosphere could mark a change from a 'normal' wehrlite (HREE-enriched garnets), to a metasomatized wehrlite ('sinusoidal', calcic garnets), finally to a sinusoidal lherzolite ('sinusoidal', less calcic garnets). The 120 km depth also marks the boundary between 'sinusoidal' garnets that have undergone carbonatite metasomatism, and 'normal' garnets that have not been metasomatized. Geochemical anomalies that are seen in trace element ratios in the garnet populations, when plotted against depth, show that there could be some kind of interlayering of lithologies in the region of the discontinuity.

The existence thus far of four 'normal' garnets with depths of origin that are only approximations gives limited confidence in the interpretation of the 120 km depth.

The samples have been metasomatized, and distinguishing whether metasomatism or a geophysical discontinuity has produced the change in the garnet geochemistry cannot be ascertained with a large degree of certainty.

7.3 Future Work

Samples derived from the Drybones Bay kimberlite pipe are heavily altered either through serpentinization, carbonatization, or a combination of both. Perhaps with larger scale bulk sampling xenoliths with primary phases other than garnet may be recovered. Conventional methods of geothermobarometry might better constrain the assumption of the paleogeotherm beneath the southwest Slave Province in the Ordovician. More samples, and in particular more garnets with a 'normal' REE pattern would enforce the importance of the 120 km depth and perhaps provide further insight into the geophysical discontinuity or metasomatism which has been interpreted here.

The Slave craton has received much attention in the recent past because of the discovery of diamondiferous kimberlites in the central part of the craton. Exploration programs have covered most of the craton where prospective kimberlites might possibly be found. This, along with the opening of the Ekati Diamond Mine (operated by BHP Diamonds Inc.) in October, 1998 will make accessible many more xenolith and xenocryst suites over a larger area of the craton. This kind of information may make it possible to link mantle beneath the central Slave craton to mantle margins at the apparent edge of the craton that have been constrained geochemically in this study.

REFERENCES

Bleeker, W., Ketchum, J.W.F., Jackson, V.A., and Villeneuve, M., 1999, The central Slave Basement Complex. Part I: Its structural topology and autochthonous core: Canadian Journal of Earth Sciences, v. 36, (in press).

Bostock, M.G., 1997, Anisotropic upper-mantle stratigraphy and architecture of the Slave craton: Nature, v. 390, p. 392-395.

Bostock, M.G., 1998, Mantle stratigraphy and evolution of the Slave province: Journal of Geophysical Research, v. 103, p. 21,183-21,200.

Bostock, M.G., and Cassidy, J.F., 1997, Upper mantle stratigraphy beneath the southern Slave craton: Canadian Journal of Earth Sciences, v. 34, p. 577-587.

Bowring, S.A., Housch, T.B., and Isachsen, C.E., 1990, The Acasta gneiss: remnant of Earth's early crust: In H. Newsome, J. Jones (eds), Origin of the Earth. Lunar and Planetary Institute, Houston, p. 242-319.

Boyd, F.R., 1989, Compositional distinction between oceanic and cratonic lithosphere: Earth and Planetary Science Letters, v. 96, p. 15-26.

Boyd, F.R., and Canil, D., 1997, Peridotite xenoliths from the Slave craton, Northwest Territories: Seventh Annual V. M. Goldschmidt Conference, Lunar and Planetary Institute, Houston, LPI contribution No. 921, p. 34-35.

Boyd, F.R., and Mertzman, S.A., 1987, Composition and structure of the Kaapvaal lithosphere, southern Africa: In B.O. Mysen (ed), Magmatic processes: physiochemical principles. Geochemical Society, Penn State University, Geochemical Society Special Publication 1, p. 13-24.

Brenker, F.E., and Brey, G.P., 1997, Reconstruction of the exhumation path of the Alpe Arami garnet-peridotite body from depths exceeding 160 km: Journal of Metamorphic Geology, v. 15, p. 581-592.

Canil, D., 1994, An experimental calibration of the "Nickel in Garnet" geothermometer with applications: Contributions to Mineralogy and Petrology, v. 117, p. 410-420.

Canil, D., 1996, An experimental calibration of the nickel in garnet geothermometer with applications: reply: Contributions to Mineralogy and Petrology, v. 124, p. 219-223.

Canil, D., 1999, The Ni-in-garnet geothermometer: calibration at natural abundances: Contributions to Mineralogy and Petrology, v. 136, p. 240-246.

Carswell, D.A., 1991, The garnet-orthopyroxene Al barometer: problematic application to natural garnet lherzolite assemblages: Mineralogical Magazine, v. 55, p. 19-31.

Chen, Z., Doherty, W., and Gregoire, D.C., 1997, Application of laser sampling Microprobe Inductively Coupled Plasma Mass Spectrometry to the in situ trace element analysis of selected geological materials: Journal of Analytical Atomic Spectrometry, v. 12, p. 653.

Cook, F.A., van der Velden, A.J., Hall, K.W., and Roberts, B.J., 1998, Tectonic delamination and subcrustal imbrication of the Precambrian lithosphere in northwestern Canada mapped by LITHOPROBE: Geology, v. 26, p. 839-842.

Cox, K.G., Smith, M.R., and Beswetherick, S., 1987, Textural studies of garnet lherzolites: evidence of exsolution origin from high-temperature harzburgites: In: Nixon PH (ed), Mantle Xenoliths, Wiley, New York, p. 537-550.

Dautria, J.M., Dupuy, C., Takherist, D., and Dostal, J., 1992, Carbonate metasomatism in the lithospheric mantle: peridotitic xenoliths from a melilititic district of the Sahara basin: Contributions to Mineralogy and Petrology, v. 111, p. 37-57.

Davis, W.J., Fryer, B.J., and King, J.E., 1994, Geochemistry and evolution of Late Archean plutonism and its significance to the tectonic development of the Slave craton: Precambrian Research, v. 67, p. 207-241.

Dawson, J.B., and Stephens, W.E., 1975, Statistical classification of garnets from kimberlite and associated xenoliths: Journal of Geology, v. 83, p. 589-607.

De Wit, M.J., Roering, C., Hart, R.J., Armstrong, R.A., de Ronde, C.E.J., Green, R.W.E., Tredoux, M., Peberdy, E., and Hart, R.A., 1992, Formation of an Archean continent: Nature, v. 357, p. 553-562.

Fipke, C.E., Gurney, J.J., and Moore, R.O., 1995, Diamond Exploration Techniques Emphasizing Indicator Mineral Geochemistry and Canadian Examples: GSC Bulletin, v. 423, p. 86 p.

Frey, F.A., Suen, C.J., and Stockman, H.W., 1985, The Rhonda high temperature peridotite: geochemistry and petrogenesis: Geochimica et Cosmochimica Acta, v. 49, p. 2469-2491.

Girnis, A.V., Brey, G.P., and Ryabchikov, I.D., 1995, Origin of Group 1A kimberlites: Fluid-saturated melting experiments at 45-55 kbar: Earth and Planetary Science Letters, v. 134, p. 283-296.

Griffin, W.L., Cousins, D.R., Ryan, C.G., Sie, S.H., and Suter, G.F., 1989, Ni in chrome pyrope garnets: a new thermometer: Contributions to Mineralogy and Petrology, v. 103, p. 199-203.

Griffin, W.L., Doyle, B.J., Ryan, C.G., Pearson, N.J., O'Reilly, S.Y., Davies, R., Kivi, K., Van Achterbergh, E., and Natapov, L.M., 1999a, Layered Mantle Lithosphere in the Lac de Gras, Slave Craton: Composition, Structure and Origin: Journal of Petrology, v. 40, p. 705-727.

Griffin, W.L., and Ryan, C.G., 1995, Trace elements in indicator minerals: area selection and target evaluation in diamond exploration: Journal of Geochemical Exploration, v. 53, p. 311-337.

Griffin, W.L., and Ryan, C.G., 1996, An experimental calibration of the "nickel in garnet" geothermometer with applications, by D. Canil: discussion: Contributions to Mineralogy and Petrology, v. 124, p. 216-218.

Griffin, W.L., Shee, S.R., Ryan, C.G., Win, T.T., and Wyatt, B.A., 1999b, Harzburgite to lherzolite and back again: metasomatic processes in ultramafic xenoliths from the Wesselton kimberlite, Kimberley, South Africa: Contributions to Mineralogy and Petrology, v. 134, p. 232-250.

Gurney, J.J., 1984, A correlation between garnets and diamonds in kimberlites: In J.E. Glover and P.G. Harris (eds.), Kimberlite Occurrence and Origin: A basis for conceptual models in exploration, Geology Department and University Extension, University of Western Australia, Publication No. 8, p. 143-166.

Haggerty, S.E., 1994, Superkimberlites: A geodynamic diamond window to the Earth's core: Earth and Planetary Science Letters, v. 122, p. 57-69.

Hart, R.J., Tredoux, M., and de Wit, M.J., 1997, refractory trace elements in diamond inclusions: Further clues to the origins of the ancient cratons: Geology, v. 25, p. 1143-1146.

Harte, B., 1977, Rock nomenclature with particular relation to deformation and recrystallisation textures in olivine-bearing xenoliths: Journal of Geology, v. 85, p. 279-288.

Hauri, E.H., Shimizu, N., Dieu, J.J., and Hart, S.R., 1993, Evidence for hotspot-related carbonatite metasomatism in the oceanic mantle: Nature, v. 365, p. 221-227.

Hawthorne, J.B., 1975, Model of a kimberlite pipe: Physics and Chemistry of the Earth, v. 9, p. 1-15.

Heaman, L.M., Kjarsgaard, B., Creaser, R.A., Cookenboo, H.O., and Kretschmar, U., 1997, Multiple episodes of kimberlite magmatism in the Slave Province, North America: In F. Cook, P. Erdmer (compilers), Slave-Northern Cordillera Lithospheric Evolution (SNORCLE) transect and Cordilleran tectonics workshop meeting (University of Calgary, 1997), LITHOPROBE Report 56, p. 14-17.

Helmstaedt, H., and Schulze, D.J., 1989, Southern African kimberlites and their mantle sample: implications for Archean tectonics and lithosphere evolution: In J Ross (ed), Kimberlites and Related Rocks Volume 1: Their Composition, Occurrence, Origin and Emplacement, Blackwell Scientific Publications, Carlton, Australia, Geological Society of Australia Special Publication Number 14.

Hoal, K.E.O., Hoal, B.G., Erlank, A.J., and Shimizu, N., 1994, Metasomatism of the mantle lithosphere recorded by rare earth elements in garnets: Earth and Planetary Science Letters, v. 126, p. 303-313.

Hoffman, P.F., 1990, Geological constraints on the origin of the mantle root beneath the Canadian Shield: Philosophical Transactions of the Royal Society, v. A331, p. 523-532.

Ionov, D.A., 1998, Trace Element Composition and Mantle-derived Carbonates and Coexisting Phases in Peridotite Xenoliths from Alkali Basalts: Journal of Petrology, v. 39, p. 1931-1941.

Ionov, D.A., Dupuy, C., O'Reilly, S.Y., Kopylova, M.G., and Genshaft, Y.S., 1993, Carbonated peridotite xenoliths from Spitsbergen: implications for trace element signatures of mantle carbonate metasomatism: Earth and Planetary Science Letters, v. 119, p. 283-297.

Isachsen, C.E., and Bowring, S.A., 1994, Evolution of the Slave craton: Geology, v. 22, p. 917-920.

Jones, A.G., and Ferguson, I.J., 1997, Results from 1996 MT studies along SNORCLE profiles 1 and 1A: In F Cook, P Erdmer (compilers), Slave-Northern Cordillera Lithospheric Evolution (SNORCLE) transect and Cordilleran tectonics workshop meeting (University of Calgary, 1997), LITHOPROBE Report 56, p. 42-47.

Kennedy, C.S., and Kennedy, G.C., 1976, The Equilibrium Boundary Between Graphite and Diamond: Journal of Geophysical Research, v. 81, p. 2467-2470.

Köhler, T., and Brey, G.P., 1990, Calcium exchange between olivine and clinopyroxene calibrated as a geothermobarometer for natural peridotites from 2-60 kb with applications: Geochimica et Cosmochimica Acta, v. 54, p. 2375-2388.

Kopylova, M.G., Russell, J.K., and Cookenboo, H., 1998, Upper-mantle stratigraphy of the Slave craton, Canada: Insights into a new kimberlite province: Geology, v. 26, p. 315-318.

Kopylova, M.G., Russell, J.K., and Cookenboo, H., 1999, Petrology of Peridotite and Pyroxenite Xenoliths from the Jericho Kimberlite: Implications for the Thermal State of the Mantle beneath the Slave Craton, Northern Canada: Journal of Petrology, v. 40, p. 79-104.

Kretschmar, U.,1997, 1997 PDAC Exploration Summary, 9p.

Krogh, E.J., 1988, The garnet-clinopyroxene Fe-Mg geothermometer - a reinterpretation of existing experimental data: Contributions to Mineralogy and Petrology, v. 99, p. 44-88.

Lewis, T.J., and Wang, K., 1992, Influence of terrain on bedrock temperatures: Palaeogeography, Palaeoclimatology, Palaeoecology, v. 98, p. 87-100.

Longerich, H.P., Jackson, S.E., and Gunther, D.J., 1996, Laser Ablation Inductively Coupled Plasma Mass Spectrometry transient signal data acquisition and analyte concentration calculation: Journal of Analytical Atomic Spectrometry, v. 11, p. 899.

MacKenzie, J.M., and Canil, D., 1999, Composition and thermal evolution of cratonic mantle beneath the central Archean Slave Province, NWT, Canada: Contributions to Mineralogy and Petrology, v. 134, p. 313-324.

Mitchell, R.H., 1986, Kimberlites: Mineralogy, Geochemistry, and Petrology: Plenum Press, New York, NY.

Mitchell, R.H., 1995, Kimberlites, Orangeites and Related Rocks: Plenum Press, New York, NY.

Nixon, P.H., and Davies, G.R., 1987, Mantle xenolith perspectives: In PH Nixon (ed), Mantle Xenoliths, Wiley, New York, p. 741-756.

Nixon, P.H., van Calsteren, P.W., Boyd, F.R., and Hawkesworth, C.J., 1987, Harzburgites with garnets of diamond facies from southern African kimberlites: In PH Nixon (ed), Mantle Xenoliths, Wiley, New York, p. 523-533.

Norman, M.D., 1998, Melting and metasomatism in the continental lithosphere: laser ablation ICPMS analysis of minerals in spinel lherzolites from eastern Australia: Contributions to Mineralogy and Petrology, v. 130, p. 240-255.

O'Neill, H.C., and Wood, B.J., 1979, An experimental study of Fe-Mg partitioning between garnet and olivine and its calibration as a geothermometer: Contributions to Mineralogy and Petrology, v. 70, p. 59-70.

Padgham, W.A., and Fyson, W.K., 1992, The Slave province: a distinct Archean craton: Canadian Journal of Earth Sciences, v. 29, p. 2072-2086.

Pell, J.A., 1995, Kimberlites in the Slave Structural Province: A Preliminary Review: Indian and Northern Affairs, Canada, EGS 1995-12, 20p.

Pell, J.A., 1997, Kimberlites in the Slave Craton, Northwest Territories, Canada: Geoscience Canada, v. 24, p. 77-90.

Power, M.A., 1997, Seismic signature of the Drybones Bay kimberlite pipe, N.W.T.: CIM Bulletin, v. 90, p. 66-69.

Reid, A.M., Donaldson, C.H., Dawson, J.B., Brown, R.W., and Ridley, W.I., 1975, The Igwisi Hills extrusive "kimberlite": Physics and Chemistry of the Earth, v. 9, p. 199-218.

Ringwood, A.E., Kesson, S.E., Hibberson, W., and Ware, N., 1992, Origin of kimberlites and related magmas: Earth and Planetary Science Letters, v. 113, p. 521-538.

Rossman, G.R., 1988, Optical Spectroscopy: In FC Hawthorne (ed), MSA Reviews in Mineralogy - Spectroscopic Methods in Mineralogy and Geology, v. 18, p. 207-223.

Rudnick, R.L., McDonough, W.F., and Chappell, B.W., 1993, Carbonatite metasomatism in the northern Tanzanian mantle: petrographic and geochemical characteristics: Earth and Planetary Science Letters, v. 114, p. 463-475.

Russell, J.K., and Kopylova, M.G., 1998, A Steady-State Conductive Geotherm for the Northern Central Slave: Inversion of Petrological Data From the Jericho Kimberlite Pipe: In: F Cook, P Erdmer (compilers), Slave-Northern Cordillera Lithospheric Evolution (SNORCLE) and Cordilleran tectonics workshop meeting (Simon Fraser University, 1998), LITHOPROBE Report No. 64, p. 45-48.

Ryan, C.G., and Griffin, W.L., 1996, Garnet geotherms: Pressure-temperature data from Cr-pyrope garnet xenocrysts in volcanic rocks: Journal of Geophysical Research, v. 101, p. 5611-5625.

Shimizu, N., 1975, Rare earth elements in garnets and clinopyroxenes from garnet lherzolite nodules in kimberlites: Earth and Planetary Science Letters, v. 25, p. 26-35.

Shimizu, N., and Richardson, S.H., 1987, Trace element abundance patterns of garnet inclusions in peridotite-suite diamonds: Geochimica et Cosmochimica Acta, v. 51, p. 755-758.

Sobolev, N.V., Lavrent'yev, Y.G., Pokhilenko, N.P., and Usova, L.V., 1973, Chrome-rich garnets from the kimberlites of Yakutia and their paragenesis: Contributions to Mineralogy and Petrology, v. 40, p. 39-52.

Solomon, M., 1963, Counting and sampling errors in modal analysis by point counter: Journal of Petrology, v. 4, p. 367-382.

Stachel, T., Viljoen, K.S., Brey, G., and Harris, J.W., 1998, Metasomatic processes in lherzolitic and harzburgitic domains of diamondiferous lithospheric mantle: REE in garnets from xenoliths and inclusions in diamonds: Earth and Planetary Science Letters, v. 159, p. 1-12.

Sweeney, R.J., Prozesky, V., and Przybylowicz, W., 1995, Selected trace and minor element partitioning between peridotite minerals and carbonatite melts at 18-46 kb pressure: Geochimica et Cosmochimica Acta, v. 59, p. 3671-3683.

Wagner, P.A., 1914, The Diamond Fields of Southern Africa: Transvaal Leader, Johannesburg, South Africa.

Wood, B.J., and Fraser, D.G., 1977, Elementary Thermodynamics for Geologists: Oxford University Press.

Woolley, A.R., Bergman, S.C., Edgar, A.D., Bas, M.J.L., Mitchell, R.H., Rock, N.M.S., and Scott-Smith, B.H., 1996, Classification of lamprophyres, lamproites, kimberlites, and the kalsilitic, melilitic, and leucitic rocks: Canadian Mineralogist, v. 34, p. 175-186.

Yaxley, G.M., Green, D.H., and Kamenetsky, V., 1998, Carbonatite Metasomatism in the Southeastern Australian Lithosphere: Journal of Petrology, v. 39, p. 1917-1930.

Zack, T., Foley, S.F., and Jenner, G.A., 1997, A consistent partition coefficient set for clinopyroxene, amphibole and garnet from laser ablation microprobe analysis of garnet pyroxenites from Kakanui, New Zealand: Neves Jahrboch Mineralogie Abhandlungen, v. 172, p. 23-41.

APPENDIX A

XENOLITH PETROGRAPHY

SAMPLE	ROCK TYPE	XENOLITH SIZE (mm^2)	GRT (Vol%)	PYR (Vol%)	OL (Vol%)	SPL (Vol%)
96-11-196 A&B	Gt Peridotite	300	20	60	15	0

Comments: Course texture with garnet grains from 2-3mm. Sample has been carbonatized and serpentinized, with some garnet grains possessing kelyphite reaction rims. Alteration has left some grains optically unresolvable (~5%).

96-16-265	Gt Peridotite	65	48	26	22	0

Comments: Course texture with pyroxene and olivine grains from 1-3mm, and garnet grains ~3mm. Sample has been carbonatized and serpentinized with 3% optically unresolvable mineralogy, and 1% secondary spinel.

96-16-401	Gt Peridotite	150	37	24	38	0

Comments: Course texture and strongly serpentinized. Garnets (2-3mm) have kelyphite reaction Rims. Secondary spinel (<1%) is also found.

96-16-467.15	Gt Peridotite	150	4	43	49	0

Comments: Course textured sample with intense alteration – even garnet grains show the effects of the alteration. No spinel is found in the sample. ~4% of sample is interstitial carbonate.

96-19-389	Gt Peridotite	500	19	7	32	0

Comments: Course texture with large garnet grains (3-6mm) which possess kelyphite reaction rims. Other minerals (i.e. olivine and pyroxene) have been badly serpentinized and/or carbonatized (~42%) so that recognition of pseudomorphs is not possible.

96-21-442.1A&B	Gt-Spl Peridotite	850	3	12	84	1

Comments: Course texture and is dominated by serpentinized olivine. Large primary spinel grains (~1mm) are seen. Garnet is seen surrounding some spinel grains. Both spinel and garnet grains occasionally possess kelyphite reaction rims.

APPENDIX B

MODAL ANALYSIS

Sample		11-196A	16-265	16-401	16-467.15	19-389	21-442.1A&B
Area	(mm^2)	400	65	150	150	500	850
Grid Spacing	(mm)	0.25	0.25	0.25	0.1	0.25	0.25
Total Counts		4493	1532	4500	7525	3114	6189
Garnet	(vol%)	39 *(1)	48 (3)	37 (1)	4 (1)	19 (1)	3 (1)
Pyroxene	(vol%)	<1	26 (3)	24 (1)	43 (1)	7 (1)	12 (1)
Olivine	(vol%)	7 (1)	22 (4)	38 (1)	49 (1)	32 (1)	84 (1)
Spinel	(vol%)						<1
Alteration		53%	4%	1%	4%	42%	<1%

*() = relative error at 2 σ

Note: "Alteration" refers to any mineralogy in thin section that was not optically resolvable as a primary phase or a pseudomorph.

APPENDIX C

MAJOR ELEMENT GEOCHEMISTRY

Garnet

Oxide %	96-11-196A	96-16-265	96-16-401	96-21-442.1	tdn-11-1a	tdn-11-1c
Na_2O	0.02	0.03	0.01	0.02	0.08	0.04
MgO	17.31	17.36	17.97	18.56	14.55	17.68
Al_2O_3	19.64	19.49	20.28	22.31	21.26	16.94
SiO_2	40.65	40.87	40.95	41.28	39.90	40.26
CaO	6.46	6.53	6.45	5.32	5.99	7.10
TiO_2	0.10	0.03	0.01	0.08	0.34	0.01
Cr_2O_3	5.29	5.65	5.12	2.37	1.04	9.27
MnO	0.51	0.47	0.56	0.54	0.66	0.48
FeO	9.05	9.04	8.57	9.34	15.59	7.69
NiO	0.01	0.01	0.02	0.02	0.01	0.00
Total	99.03	99.47	99.93	99.84	99.41	99.47
Cation						
NA+	0.003	0.004	0.002	0.004	0.002	0.010
MG2+	1.898	1.896	1.945	1.989	1.609	1.950
AL3+	1.702	1.683	1.736	1.893	1.857	1.480
SI4+	2.989	2.994	2.975	2.974	2.959	2.980
CA2+	0.509	0.513	0.502	0.411	0.476	0.560
TI4+	0.006	0.002	0.000	0.004	0.009	0.000
CR3+	0.307	0.327	0.294	0.136	0.481	0.540
MN2+	0.032	0.029	0.034	0.033	0.041	0.030
FE2+	0.556	0.554	0.520	0.564	0.567	0.480
NI2+	0.000	0.001	0.001	0.001	0.000	0.000
CATSUM	8.002	8.001	8.011	8.009	8.001	8.017

*tdn prefix indicates coarse concentrate; tdngc prefix indicates garnet/clinopyroxene pair; 96- prefix indicates xenolith.

Garnet

Oxide %	tdn-11-1d	tdnc-10a	tdnc-10b	tdnc-10c	tdnc-10d	tdnc-10e
Na_2O	0.01	0.00	0.02	0.00	0.00	0.00
MgO	17.04	17.61	18.88	17.98	18.12	17.56
Al_2O_3	17.11	18.45	19.79	19.63	19.04	18.32
SiO_2	40.11	40.43	41.03	40.80	40.69	40.52
CaO	7.69	7.18	5.96	6.97	7.16	7.49
TiO_2	0.00	0.01	0.01	0.05	0.06	0.01
Cr_2O_3	8.93	7.54	5.85	6.05	6.90	7.61
MnO	0.44	0.42	0.39	0.35	0.40	0.39
FeO	8.05	7.54	7.93	7.87	7.23	7.46
NiO	0.04	0.01	0.01	0.02	0.00	0.02
Total	99.43	99.19	99.87	99.72	99.60	99.38
Cation						
NA+	0.000	0.000	0.003	0.000	0.000	0.000
MG2+	1.880	1.932	2.041	1.953	1.972	1.924
AL3+	1.500	1.600	1.691	1.685	1.638	1.587
SI4+	2.970	2.976	2.975	2.972	2.970	2.978
CA2+	0.610	0.566	0.463	0.544	0.560	0.590
TI4+	0.000	0.001	0.001	0.003	0.003	0.001
CR3+	0.520	0.439	0.335	0.348	0.398	0.442
MN2+	0.030	0.026	0.024	0.022	0.025	0.024
FE2+	0.500	0.464	0.481	0.479	0.441	0.459
NI2+	0.000	0.001	0.001	0.001	0.000	0.001
CATSUM	8.017	8.004	8.013	8.008	8.008	8.006

*tdn prefix indicates coarse concentrate; tdngc prefix indicates garnet/clinopyroxene pair; 96- prefix indicates xenolith.

Garnet

Oxide %	tdnc-11c	tdnc-11d	tdnc-11e	tdnc-12a	tdnc-12b	tdnc-12c
Na_2O	0.00	0.01	0.01	0.00	0.01	0.01
MgO	17.77	17.74	18.03	16.63	17.21	17.29
Al_2O_3	19.56	18.23	19.11	17.38	17.94	18.22
SiO_2	40.85	40.54	40.62	40.07	40.31	40.38
CaO	6.82	7.71	6.96	7.89	7.88	7.35
TiO_2	0.02	0.01	0.00	0.00	0.02	0.00
Cr_2O_3	6.38	7.66	6.84	8.56	8.10	7.62
MnO	0.40	0.35	0.40	0.47	0.38	0.44
FeO	8.34	7.33	7.46	8.36	7.41	8.08
NiO	0.03	0.01	0.02	0.01	0.01	0.02
Total	100.17	99.59	99.45	99.37	99.27	99.41
Cation						
NA+	0.000	0.001	0.001	0.000	0.001	0.001
MG2+	1.926	1.940	1.966	1.840	1.893	1.900
AL3+	1.676	1.576	1.647	1.520	1.560	1.583
SI4+	2.971	2.974	2.971	2.974	2.975	2.976
CA2+	0.531	0.606	0.545	0.628	0.623	0.580
TI4+	0.001	0.001	0.000	0.000	0.001	0.000
CR3+	0.367	0.444	0.396	0.502	0.473	0.444
MN2+	0.025	0.022	0.025	0.030	0.024	0.027
FE2+	0.507	0.450	0.456	0.519	0.457	0.498
NI2+	0.002	0.001	0.001	0.001	0.001	0.001
CATSUM	8.007	8.015	8.008	8.014	8.008	8.011

*tdn prefix indicates coarse concentrate; tdngc prefix indicates garnet/clinopyroxene pair; 96- prefix indicates xenolith.

Garnet

Oxide %	tdnc-12d	tdnc-12e	tdnc-13a	tdnc-13b	tdnc-13c	tdnc-13d
Na_2O	0.01	0.01	0.01	0.01	0.02	0.01
MgO	18.00	18.09	17.23	17.98	18.08	17.86
Al_2O_3	13.92	19.22	17.36	19.08	19.38	19.04
SiO_2	39.72	40.71	40.23	40.71	40.95	40.57
CaO	6.48	7.09	8.09	7.12	6.42	6.81
TiO_2	0.01	0.02	0.00	0.04	0.02	0.01
Cr_2O_3	13.30	6.51	8.86	6.92	6.35	6.83
MnO	0.44	0.36	0.34	0.38	0.46	0.39
FeO	7.29	7.61	7.20	7.54	8.10	8.00
NiO	0.00	0.00	0.00	0.01	0.03	0.01
Total	99.17	99.62	99.32	99.79	99.81	99.53
Cation						
NA+	0.001	0.001	0.001	0.001	0.003	0.001
MG2+	2.011	1.969	1.899	1.955	1.963	1.950
AL3+	1.230	1.654	1.512	1.640	1.664	1.643
SI4+	2.977	2.972	2.974	2.970	2.983	2.971
CA2+	0.520	0.555	0.641	0.557	0.501	0.534
TI4+	0.001	0.001	0.000	0.002	0.001	0.001
CR3+	0.788	0.376	0.518	0.399	0.366	0.395
MN2+	0.028	0.022	0.021	0.023	0.028	0.024
FE2+	0.457	0.465	0.445	0.460	0.493	0.490
NI2+	0.000	0.000	0.000	0.001	0.002	0.001
CATSUM	8.014	8.013	8.012	8.009	8.003	8.010

*tdn prefix indicates coarse concentrate; tdngc prefix indicates garnet/clinopyroxene pair; 96- prefix indicates xenolith.

Garnet

Oxide %	tdnc-13e	tdnc-15a	tdnc-15b	tdnc-15c	tdnc-15d	tdnc-15e
Na_2O	0.01	0.00	0.02	0.00	0.01	0.01
MgO	17.59	17.39	16.47	17.71	19.44	18.22
Al_2O_3	18.44	18.67	17.67	18.50	19.61	19.33
SiO_2	40.72	40.76	40.15	40.62	40.90	40.96
CaO	7.48	7.09	8.01	7.58	5.12	6.67
TiO_2	0.01	0.01	0.00	0.01	0.01	0.02
Cr_2O_3	7.40	6.63	8.40	7.64	6.45	6.21
MnO	0.36	0.37	0.49	0.40	0.41	0.37
FeO	7.27	7.82	8.41	7.58	7.84	7.30
NiO	0.01	0.01	0.00	0.01	0.02	0.00
Total	99.29	98.75	99.62	100.05	99.81	99.09
Cation						
NA+	0.001	0.000	0.003	0.000	0.001	0.001
MG2+	1.925	1.935	1.818	1.929	1.986	2.002
AL3+	1.595	1.642	1.542	1.593	1.664	1.679
SI4+	2.989	2.967	2.972	2.968	2.996	2.967
CA2+	0.588	0.567	0.635	0.593	0.523	0.527
TI4+	0.001	0.001	0.000	0.001	0.001	0.001
CR3+	0.429	0.391	0.492	0.441	0.359	0.362
MN2+	0.022	0.023	0.031	0.025	0.023	0.023
FE2+	0.446	0.488	0.521	0.463	0.446	0.450
NI2+	0.001	0.001	0.000	0.001	0.001	0.000
CATSUM	7.999	8.015	8.013	8.014	8.000	8.012

*tdn prefix indicates coarse concentrate; tdngc prefix indicates garnet/clinopyroxene pair; 96- prefix indicates xenolith.

Garnet

Oxide %	tdnc-16a	tdnc-16b	tdnc-16c	tdnc-16d	tdnc2-12a	tdnc2-13a
Na_2O	0.00	0.00	0.00	0.01	0.04	0.07
MgO	17.34	17.27	17.75	18.49	19.95	18.25
Al_2O_3	18.54	18.70	19.57	20.05	21.10	17.91
SiO_2	40.48	40.47	40.71	40.90	41.64	40.87
CaO	7.57	7.37	6.97	6.03	4.67	5.73
TiO_2	0.01	0.02	0.01	0.03	0.24	0.28
Cr_2O_3	7.55	7.00	5.94	5.72	3.88	7.27
MnO	0.43	0.40	0.37	0.42	0.41	0.46
FeO	7.81	8.04	7.98	8.25	8.41	8.92
NiO	0.01	0.02	0.01	0.02	0.02	0.00
Total	99.74	99.29	99.31	99.92	100.35	99.73
Cation						
NA+	0.000	0.000	0.000	0.001	0.006	0.010
MG2+	1.896	1.895	1.936	2.000	2.128	1.995
AL3+	1.603	1.622	1.688	1.715	1.780	1.547
SI4+	2.970	2.978	2.979	2.968	2.980	2.997
CA2+	0.595	0.581	0.546	0.469	0.358	0.450
TI4+	0.001	0.001	0.001	0.002	0.013	0.015
CR3+	0.438	0.407	0.344	0.328	0.220	0.422
MN2+	0.027	0.025	0.023	0.026	0.025	0.029
FE2+	0.479	0.495	0.488	0.501	0.503	0.547
NI2+	0.001	0.001	0.001	0.001	0.002	0.000
CATSUM	8.009	8.006	8.005	8.010	8.011	8.009

*tdn prefix indicates coarse concentrate; tdngc prefix indicates garnet/clinopyroxene pair; 96- prefix indicates xenolith.

Garnet

Oxide %	tdnc2-13d	tdnc2-15c	tdngc-a	tdngc-c	tdngc-d	tdngc-e
Na_2O	0.04	0.04	0.03	0.06	0.07	0.06
MgO	19.29	19.51	19.06	19.19	20.45	19.21
Al_2O_3	18.42	18.84	19.59	17.32	21.32	17.52
SiO_2	41.11	41.37	40.80	40.45	40.97	40.32
CaO	5.54	5.31	5.26	5.51	4.05	5.53
TiO_2	0.16	0.14	0.10	0.30	0.16	0.35
Cr_2O_3	7.16	6.51	5.91	8.59	3.87	8.38
MnO	0.43	0.36	0.50	0.42	0.46	0.39
FeO	7.88	7.83	8.52	8.11	8.52	7.90
NiO	0.01	0.03	0.01	0.00	0.01	0.00
Total	100.01	99.92	99.77	99.96	99.88	99.66
Cation						
NA+	0.005	0.006	0.004	0.008	0.010	0.009
MG2+	2.089	2.107	2.064	2.090	2.187	2.093
AL3+	1.577	1.609	1.632	1.488	1.794	1.507
SI4+	2.987	2.997	2.982	2.950	2.934	2.947
CA2+	0.431	0.413	0.409	0.431	0.310	0.433
TI4+	0.009	0.008	0.005	0.016	0.009	0.019
CR3+	0.411	0.373	0.338	0.495	0.219	0.484
MN2+	0.027	0.022	0.031	0.026	0.028	0.024
FE2+	0.479	0.474	0.517	0.495	0.510	0.483
NI2+	0.001	0.002	0.002	0.001	0.002	0.001
CATSUM	8.013	8.008	7.984	8.000	8.003	8.000

*tdn prefix indicates coarse concentrate; tdngc prefix indicates garnet/clinopyroxene pair; 96- prefix indicates xenolith.

Clinopyroxene

Oxide %	tdngc-a	tdngc-c	tdngc-d	tdngc-e
Na_2O	3.79	3.14	3.34	2.99
MgO	13.96	14.90	14.75	15.19
Al_2O_3	3.70	2.45	3.73	2.48
SiO_2	54.14	54.16	54.13	54.23
CaO	16.83	17.01	16.98	17.27
TiO_2	0.08	0.16	0.13	0.17
Cr_2O_3	3.52	4.23	2.60	3.71
MnO	0.06	0.13	0.11	0.11
FeO	2.85	2.68	3.08	2.63
NiO	0.02	0.05	0.09	0.04
Total	98.95	98.91	98.93	98.80
Cation				
NA+	0.273	0.222	0.234	0.211
MG2+	0.753	0.810	0.801	0.835
AL3+	0.157	0.106	0.159	0.106
SI4+	1.967	1.985	1.970	1.980
CA2+	0.652	0.664	0.659	0.673
TI4+	0.002	0.004	0.004	0.005
CR3+	0.101	0.122	0.074	0.106
MN2+	0.002	0.004	0.003	0.003
FE2+	0.086	0.082	0.093	0.080
NI2+	0.007	0.001	0.003	0.001
CATSUM	4.000	4.000	4.000	4.000

*tdn prefix indicates coarse concentrate; tdngc prefix indicates garnet/clinopyroxene pair; 96- prefix indicates xenolith.

APPENDIX D

TRACE ELEMENT GEOCHEMISTRY

GARNET

Element (ppm)	96-11-196A	96-16-265	96-16-401	96-21-442.1	tdn-11-1a	tdn-11-1c	tdn-11-1d	tdnc-10a
V	251.81	121.37	285.59	132.14	223.96	429.03	588.33	384.18
Ni	28.10	12.09	34.62	20.80	15.88	70.73	44.71	48.04
Ga	3.66	9.93	2.08	2.87	14.51	3.24	3.32	2.63
Ge	2.48	2.28	3.38	7.32	19.20	3.57	bd	2.44
Sr	0.64	0.33	4.69	0.47	0.87	1.53	0.43	bd
Y	22.47	26.23	0.30	15.44	59.52	2.57	0.44	0.23
Zr	8.24	4.59	1.10	7.39	110.80	56.11	2.33	bd
Nb	0.20	0.12	1.04	0.37	1.11	1.07	0.44	0.20
La	0.22	0.07	0.53	0.28	0.41	1.40	1.15	bd
Ce	0.52	0.40	1.67	0.12	0.56	9.26	5.71	bd
Pr	0.08	0.14	0.18	0.10	0.29	2.01	0.85	bd
Nd	0.71	1.52	0.70	0.49	1.41	12.24	3.33	bd
Sm	0.82	1.06	0.36	0.63	2.00	3.95	0.52	bd
Eu	0.46	0.57	0.12	0.23	0.75	1.17	0.14	bd
Gd	2.04	2.08	0.64	1.46	4.02	3.19	0.41	bd
Tb	0.50	0.51	0.04	0.25	0.99	0.30	bd	bd
Dy	3.95	4.25	0.15	2.19	11.78	0.82	0.15	bd
Ho	0.91	1.08	0.04	0.58	2.54	0.11	bd	0.02
Er	2.89	3.37	0.16	2.06	8.04	0.23	bd	bd
Tm	0.43	0.52	0.04	0.34	1.71	0.04	bd	0.03
Yb	2.94	3.64	0.26	2.50	11.38	0.25	0.26	0.45
Lu	0.46	0.54	0.06	0.41	1.95	0.05	0.06	0.13
Hf	0.34	0.07	0.14	0.30	2.54	0.63	bd	bd
Th	0.04	0.02	0.10	0.08	0.20	0.71	0.75	bd
U	1.34	0.05	0.05	0.06	0.15	0.66	0.67	bd

*tdn prefix indicates coarse concentrate; tdngc prefix indicates garnet/clinopyroxene pairs;
96- prefix indicates xenolith. "bd" – below detection limits of LAM-ICP-MS.

GARNET

Element (ppm)	tdnc-10b	tdnc-10c	tdnc-10d	tdnc-10e	tdnc-11c	tdnc-11d	tdnc-11e	tdnc-12a
V	332.43	393.18	304.70	321.33	481.22	371.30	348.97	446.26
Ni	35.99	35.25	41.00	27.23	35.96	38.15	34.70	32.41
Ga	3.74	3.22	1.95	2.53	1.96	2.29	2.09	2.40
Ge	1.70	2.09	bd	2.35	2.01	2.86	2.20	2.69
Sr	bd	bd	0.24	0.23	0.26	0.23	0.58	0.19
Y	0.96	1.50	1.42	0.35	0.19	0.24	0.38	0.56
Zr	7.70	1.95	7.00	bd	0.57	bd	bd	1.10
Nb	0.58	1.04	2.18	0.26	0.91	1.12	0.49	1.12
La	0.12	bd	0.20	0.79	0.23	0.38	0.99	0.32
Ce	0.53	0.53	1.32	0.84	1.86	2.96	2.20	1.93
Pr	0.12	0.08	0.31	0.08	0.30	0.35	0.07	0.31
Nd	0.65	0.26	1.81	0.37	1.03	0.66	0.18	1.34
Sm	0.25	bd	0.48	bd	bd	bd	bd	bd
Eu	0.05	bd	0.14	bd	0.04	bd	bd	0.06
Gd	bd	bd	0.32	bd	bd	bd	bd	bd
Tb	bd	0.02	0.04	bd	bd	bd	bd	bd
Dy	0.11	0.17	0.33	bd	bd	bd	bd	0.08
Ho	bd	0.06	0.07	bd	bd	bd	bd	bd
Er	0.14	0.31	0.21	0.10	bd	bd	0.06	0.11
Tm	0.03	0.07	0.04	0.03	bd	bd	bd	0.03
Yb	0.45	0.67	0.31	0.42	0.27	0.34	0.32	0.33
Lu	0.09	0.14	0.07	0.10	0.08	0.10	0.08	0.08
Hf	0.11	0.13	0.17	bd	bd	bd	bd	bd
Th	bd	bd	0.47	bd	0.05	0.15	0.17	0.13
U	0.08	0.03	0.10	bd	0.03	0.10	bd	0.05

*tdn prefix indicates coarse concentrate; tdngc prefix indicates garnet/clinopyroxene pairs;
96- prefix indicates xenolith. "bd" – below detection limits of LAM-ICP-MS.

GARNET

Element (ppm)	tdnc-12b	tdnc-12c	tdnc-12d	tdnc-12e	tdnc-13a	tdnc-13b	tdnc-13c	tdnc-13d
V	425.12	483.01	501.32	395.41	376.33	329.87	373.99	409.39
Ni	23.32	28.40	44.79	37.79	30.10	33.11	36.15	36.29
Ga	2.93	2.30	2.73	2.66	2.69	3.05	3.77	3.29
Ge	1.96	1.94	2.37	2.32	2.05	2.30	2.43	2.37
Sr	0.14	bd	2.34	bd	bd	0.29	bd	bd
Y	0.38	0.19	0.69	0.58	0.34	1.03	0.54	0.55
Zr	1.73	bd	1.75	1.95	bd	0.29	0.68	0.34
Nb	0.38	0.23	0.56	1.24	0.19	0.27	0.29	0.16
La	0.20	0.07	0.61	0.09	bd	0.41	bd	bd
Ce	1.71	0.55	1.49	0.64	bd	0.92	0.17	0.06
Pr	0.36	0.12	0.22	0.10	bd	0.07	0.06	bd
Nd	2.10	0.55	0.86	0.42	bd	0.26	0.27	bd
Sm	0.37	bd	bd	0.11	bd	bd	0.13	bd
Eu	0.06	bd	bd	bd	bd	bd	bd	bd
Gd	bd	bd	bd	bd	bd	bd	bd	bd
Tb	bd	bd	bd	bd	bd	0.02	bd	bd
Dy	bd	bd	0.15	0.07	bd	0.16	0.10	0.07
Ho	bd	bd	bd	bd	bd	0.04	bd	bd
Er	bd	bd	bd	0.13	bd	0.23	bd	0.11
Tm	0.02	0.02	bd	0.03	0.05	0.05	0.03	0.04
Yb	0.42	0.18	0.20	0.42	0.52	0.53	0.37	0.34
Lu	0.13	0.08	0.05	0.11	0.16	0.14	0.09	0.09
Hf	bd	bd	bd	bd	bd	bd	bd	bd
Th	0.06	0.04	bd	0.05	bd	0.06	bd	0.08
U	0.06	0.06	bd	0.03	0.02	bd	bd	0.25

*tdn prefix indicates coarse concentrate; tdngc prefix indicates garnet/clinopyroxene pairs;
96- prefix indicates xenolith. "bd" – below detection limits of LAM-ICP-MS.

GARNET

Element (ppm)	tdnc-13e	tdn-11-2c	tdnc-15b	tdnc-15c	tdnc-15d	tdnc-15e	tdnc-16a	tdnc-16b
V	342.04	318	399.27	376.23	301.07	286.89	337.20	416.86
Ni	33.24	109	28.76	34.75	22.55	24.03	31.61	33.59
Ga	2.42	Bd	1.92	2.40	1.47	2.25	1.79	2.23
Ge	bd	Bd	2.33	1.71	2.01	2.30	bd	bd
Sr	0.86	14.6	bd	0.31	0.57	0.43	bd	bd
Y	0.56	Bd	0.15	0.27	1.30	0.75	0.17	0.60
Zr	0.83	Bd	0.56	1.24	1.30	bd	bd	3.29
Nb	0.53	3.57	0.80	1.76	0.44	0.36	0.21	1.27
La	0.76	2.51	0.16	0.43	0.23	0.07	bd	0.13
Ce	2.67	4.13	1.85	2.64	0.86	0.50	bd	1.37
Pr	0.31	0.44	0.46	0.37	0.14	0.07	bd	0.35
Nd	1.18	1.73	2.16	0.89	0.63	0.27	bd	1.60
Sm	0.21	Bd	bd	bd	bd	bd	bd	bd
Eu	bd	Bd	bd	bd	0.07	bd	bd	bd
Gd	bd	Bd	bd	bd	bd	bd	bd	bd
Tb	bd	Bd	bd	bd	0.02	bd	bd	bd
Dy	bd	Bd	bd	0.07	0.14	bd	bd	0.13
Ho	bd	Bd	bd	bd	0.05	bd	bd	bd
Er	0.13	Bd	bd	bd	0.24	0.21	bd	bd
Tm	0.04	Bd	0.02	bd	0.07	0.05	0.02	0.04
Yb	0.65	Bd	0.35	0.26	0.83	0.47	0.35	0.34
Lu	0.14	Bd	0.10	0.09	0.31	0.14	0.09	0.08
Hf	bd	Bd	bd	bd	bd	bd	bd	0.15
Th	0.12	0.70	0.07	0.14	bd	bd	bd	0.08
U	0.04	0.04	0.16	0.05	bd	0.01	bd	0.06

*tdn prefix indicates coarse concentrate; tdngc prefix indicates garnet/clinopyroxene pairs;
96- prefix indicates xenolith. "bd" – below detection limits of LAM-ICP-MS.

GARNET

Element (ppm)	tdnc-16c	tdnc-16d	tdnc2-12a	tdnc2-13a	tdnc2-11d	tdnc2-15c	tdngc-a	tdngc-c
V	392.38	356.57	242.25	231.77	318	257.58	165	206
Ni	33.69	33.21	55.40	38.94	45.1	34.91	48.0	43.0
Ga	2.07	3.30	4.40	5.48	5.36	5.60	4.65	5.11
Ge	1.77	bd	bd	bd	bd	bd	2.26	Bd
Sr	bd	bd	bd	0.60	0.38	0.50	21.25	11.4
Y	0.41	1.09	7.72	11.88	3.64	9.48	35.13	37.3
Zr	bd	0.97	59.13	135.50	49.1	89.50	94.37	117
Nb	0.29	bd	bd	0.69	0.55	0.75	3.08	1.22
La	bd	bd	bd	0.09	bd	bd	1.30	1.89
Ce	0.10	0.05	0.26	0.84	0.58	0.63	2.87	1.34
Pr	bd	bd	0.10	0.34	0.25	0.22	0.62	0.30
Nd	bd	0.13	1.30	3.34	2.63	2.61	3.46	1.83
Sm	bd	bd	1.12	2.61	1.77	2.28	1.46	1.44
Eu	bd	bd	0.57	1.15	0.71	0.95	0.79	0.78
Gd	bd	bd	1.74	4.03	1.76	3.41	3.06	3.13
Tb	bd	bd	0.38	0.72	0.25	0.53	0.42	0.50
Dy	bd	0.16	2.12	3.78	1.08	2.66	2.66	2.99
Ho	0.02	0.05	0.38	0.49	0.19	0.36	0.50	0.52
Er	0.11	0.25	0.67	0.83	0.40	0.75	1.03	1.14
Tm	0.04	0.05	0.10	0.11	0.05	0.08	0.11	0.12
Yb	0.54	0.46	0.72	0.59	0.53	0.58	0.60	0.66
Lu	0.17	0.10	0.13	0.13	0.11	0.11	0.13	0.11
Hf	bd	bd	1.46	2.84	1.17	1.71	1.32	2.13
Th	bd	bd	bd	bd	bd	bd	0.15	0.07
U	bd	0.04	bd	0.03	0.03	0.03	0.10	0.04

*tdn prefix indicates coarse concentrate; tdngc prefix indicates garnet/clinopyroxene pairs;
96- prefix indicates xenolith. "bd" – below detection limits of LAM-ICP-MS.

APPENDIX E

TEMPERATURES, DEPTHS AND TRACE RATIOS

GARNET		*CLINOPYROXENE*				
Element (ppm)	**tdngc-d**	**tdngc-e**	***tdngc-a***	***tdngc-c***	***tdngc-d***	***tdngc-e***	**Detection Limits**
V	133	224	*317.27*	*112.45*	*84.37*	*109.98*	**1.66**
Ni	41.0	41.0	*444.13*	*84.25*	*70.10*	*84.69*	**28.21**
Ga	3.67	4.35	*13.62*	*1.53*	*1.56*	*1.80*	**1.19**
Ge	2.40	1.98	*1.46*	*0.68*	*0.56*	*0.69*	**3.02**
Sr	0.44	1.05	*185.10*	*81.16*	*91.04*	*76.23*	**0.33**
Y	27.3	25.28	*3.74*	*1.66*	*1.84*	*1.16*	**0.24**
Zr	150	107.28	*69.38*	*30.07*	*52.43*	*22.49*	**0.45**
Nb	0.29	0.54	*12.50*	*6.06*	*1.73*	*0.75*	**0.36**
La	Bd	0.36	*15.92*	*6.52*	*3.02*	*2.85*	**0.13**
Ce	0.27	1.33	*42.12*	*14.32*	*9.69*	*8.46*	**0.07**
Pr	0.12	0.24	*5.10*	*1.79*	*1.46*	*1.21*	**0.09**
Nd	1.14	1.84	*20.15*	*7.24*	*6.62*	*5.33*	**0.30**
Sm	1.20	1.42	*3.67*	*1.43*	*1.33*	*1.13*	**0.49**
Eu	0.66	0.91	*1.02*	*0.42*	*0.38*	*0.33*	**0.13**
Gd	2.42	3.76	*2.68*	*1.05*	*0.94*	*0.75*	**0.81**
Tb	0.45	0.55	*0.32*	*0.13*	*0.12*	*0.09*	**0.05**
Dy	2.75	3.39	*1.32*	*0.59*	*0.58*	*0.40*	**0.20**
Ho	0.51	0.54	*0.18*	*0.08*	*0.08*	*0.05*	**0.06**
Er	1.02	1.28	*0.37*	*0.15*	*0.18*	*0.11*	**0.20**
Tm	0.10	0.15	*0.04*	*0.02*	*0.02*	*0.01*	**0.04**
Yb	0.49	1.11	*0.20*	*0.07*	*0.08*	*0.04*	**0.17**
Lu	0.09	0.19	*0.02*	*0.01*	*0.01*	*0.00*	**0.05**
Hf	1.38	1.98	*3.21*	*1.73*	*2.13*	*1.38*	**0.21**
Th	bd	0.03	*1.69*	*0.36*	*0.15*	*0.02*	**0.03**
U	0.01	0.04	*0.46*	*0.09*	*0.05*	*0.01*	**0.03**

*tdn prefix indicates coarse concentrate; tdngc prefix indicates garnet/clinopyroxene pairs; 96- prefix indicates xenolith. "bd" – below detection limits of LAM-ICP-MS. Typical detections limits for the LAM-ICP-MS at the University of Victoria are included.

APPENDIX E

TEMPERATURE, DEPTH AND TRACE RATIOS

SAMPLE	Ni (ppm)	*T_{Ni} (°C)	Depth (km)	La/Yb	Th/U	Nb/U	Nb/Th	Ce/Yb	Zr/Y	Yb/Ga	Y/V
96-11-196A	28	966	114	0.08	0.03	0.15	4.89	0.18	0.37	0.80	0.09
96-16-265	12	849	94	0.02	0.47	2.47	5.29	0.11	0.17	0.37	0.22
96-16-401	35	997	120	2.04	2.09	22.61	10.83	6.41	3.62	0.13	-
96-21-442.1	21	906	104	0.11	1.39	6.22	4.48	0.05	0.48	0.87	0.12
tdn-11-1a	16	853	94	0.04	1.32	7.53	5.69	0.05	1.86	0.78	0.27
tdn-11-1c	71	1112	143	5.60	1.08	1.62	1.51	37.04	21.83	0.08	0.01
tdn-11-1d	45	1042	129	4.42	1.12	0.66	0.59	21.96	5.30	0.08	-
tdnc-10a	48	1055	131	-	-	-	-	-	-	0.17	-
tdnc-10b	36	1007	122	0.27	-	7.00	-	1.18	7.99	0.12	-
tdnc-10c	35	1003	121	-	-	36.73	-	0.80	1.30	0.21	-
tdnc-10d	41	1028	126	0.65	4.45	20.80	4.67	4.32	4.94	0.16	-
tdnc-10e	27	963	114	1.89	-	-	-	2.03	-	0.16	-
tdnc-11c	36	1006	122	0.86	1.81	31.87	17.60	6.93	3.00	0.14	-
tdnc-11d	38	1016	124	1.13	1.49	10.90	7.31	8.76	-	0.15	-
tdnc-11e	35	1001	121	3.07	-	-	2.95	6.79	-	0.15	-
tdnc-12a	32	990	119	0.97	2.45	21.55	8.79	5.87	1.98	0.14	-
tdnc-12b	23	941	110	0.47	0.95	5.87	6.17	4.06	4.50	0.14	-
tdnc-12c	28	970	115	0.39	0.75	3.94	5.22	3.00	-	0.08	-
tdnc-12d	45	1043	129	2.96	-	-	-	7.27	2.54	0.08	-
tdnc-12e	38	1014	124	0.20	1.62	39.40	24.28	1.51	3.37	0.16	-
tdnc-13a	30	979	117	-	-	8.67	-	-	-	0.19	-
tdnc-13b	33	993	120	0.77	-	-	4.80	1.74	0.28	0.17	-
tdnc-13c	36	1007	122	-	-	-	-	0.47	1.26	0.10	-
tdnc-13d	36	1008	122	-	0.33	0.65	1.99	0.18	0.61	0.10	-
tdnc-13e	33	994	120	1.17	2.93	12.60	4.31	4.11	1.49	0.27	-
tdn-11-2c	109	1236	164	-	-	-	5.10	-	-	-	-
tdnc-15b	29	972	115	0.46	0.42	5.08	12.16	5.32	3.76	0.18	-
tdnc-15c	35	1001	121	1.67	3.09	38.75	12.53	10.30	4.64	0.11	-
tdnc-15d	23	936	109	0.27	-	-	-	1.04	1.00	0.56	-
tdnc-15e	24	945	111	0.15	-	25.55	-	1.06	-	0.21	-

*T_{Ni} calculated using Ni-in-garnet geothermometer after Canil (1999). Depth estimates were calculated from projection to an assumed 41 mW/m^2 geotherm.

SAMPLE	Ni (ppm)	*T_{Ni} (°C)	Depth (km)	La/Yb	Th/U	Nb/U	Nb/Th	Ce/Yb	Zr/Y	Yb/Ga	Y/V
tdnc-16a	32	986	118	-	-	-	-	-	-	0.19	-
tdnc-16b	34	996	120	0.37	1.22	19.97	16.37	3.99	5.52	0.15	-
tdnc-16c	34	996	120	-	-	-	-	0.19	-	0.26	-
tdnc-16d	33	994	120	-	-	-	-	0.12	0.89	0.14	-
tdnc2-12a	55	1080	136	-	-	-	-	0.36	7.66	0.16	0.03
tdnc2-13a	39	1019	125	0.15	-	21.38	-	1.42	11.40	0.11	0.05
tdnc2-11d	45	1037	129	-	-	18.3	-	1.10	13.5	0.10	0.01
tdnc2-15c	35	1002	121	-	-	28.73	-	1.09	9.44	0.10	0.04
tdngc-a	48	1055	131	-	-	-	-	4.8	2.69	0.13	0.21
tdngc-c	43	1028	128	-	-	-	-	2.03	3.16	0.13	0.18
tdngc-d	41	1019	126	-	-	-	-	0.55	5.50	0.13	0.21
tdngc-e	41	1019	126	-	-	-	-	1.20	4.24	0.25	0.11

*T_{Ni} calculated using Ni-in-garnet geothermometer after Canil (1999). Depth estimates were calculated from projection to an assumed 41 mW/m^2 geotherm.

APPENDIX F

GARNET REE PATTERN PLOTS

Garnet Rare Earth Element (REE) concentrations normalized to chondrite for all 42 garnets studied from the Drybones Bay kimberlite. The resulting REE patterns are shown for 'normal' garnets (plot A) and 'sinusoidal' garnets (plots B-E). In many samples not all element concentrations are above detection. Elements with concentrations below detection are ignored and the sample pattern is joined to the next element with values above detection.

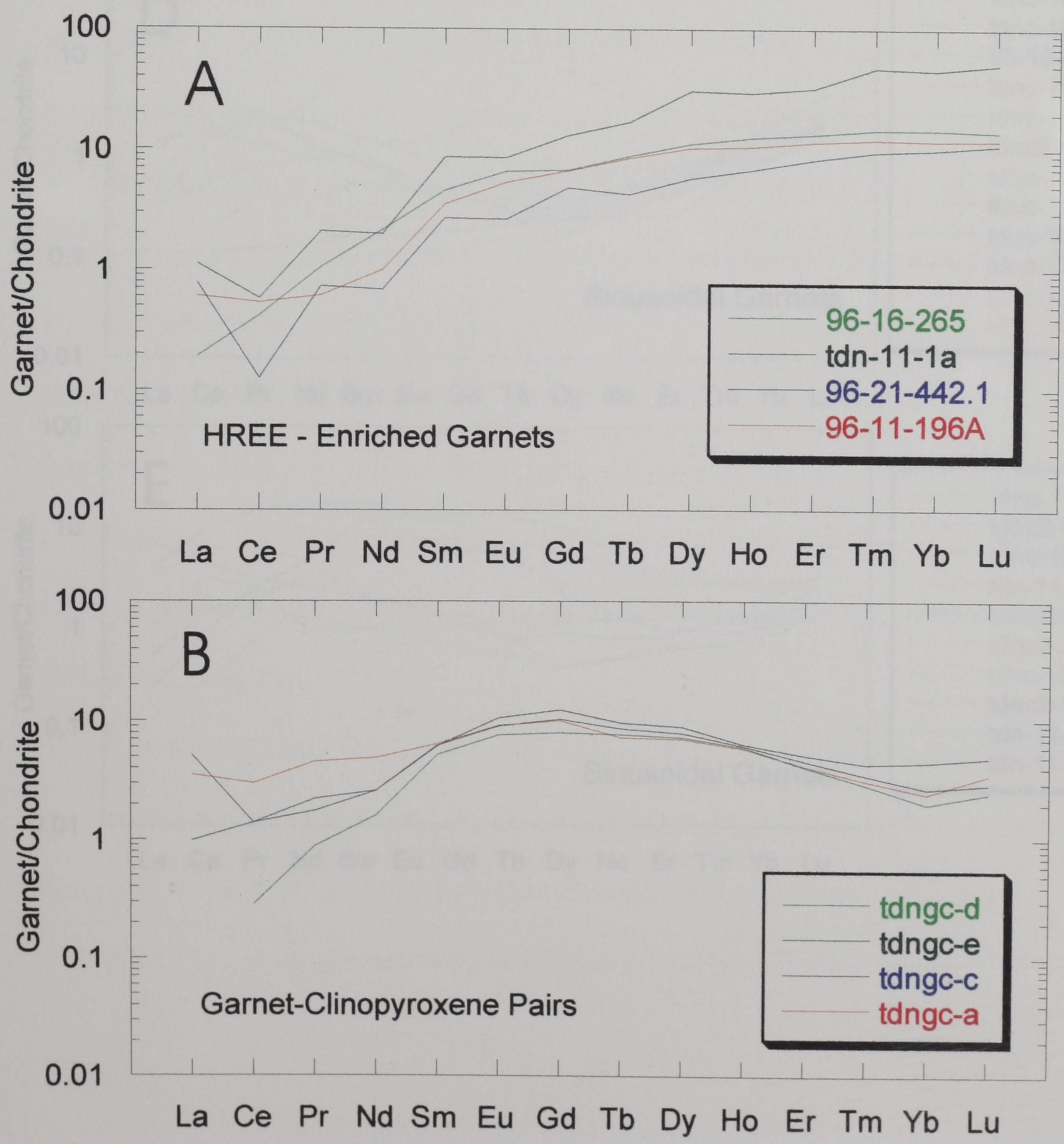

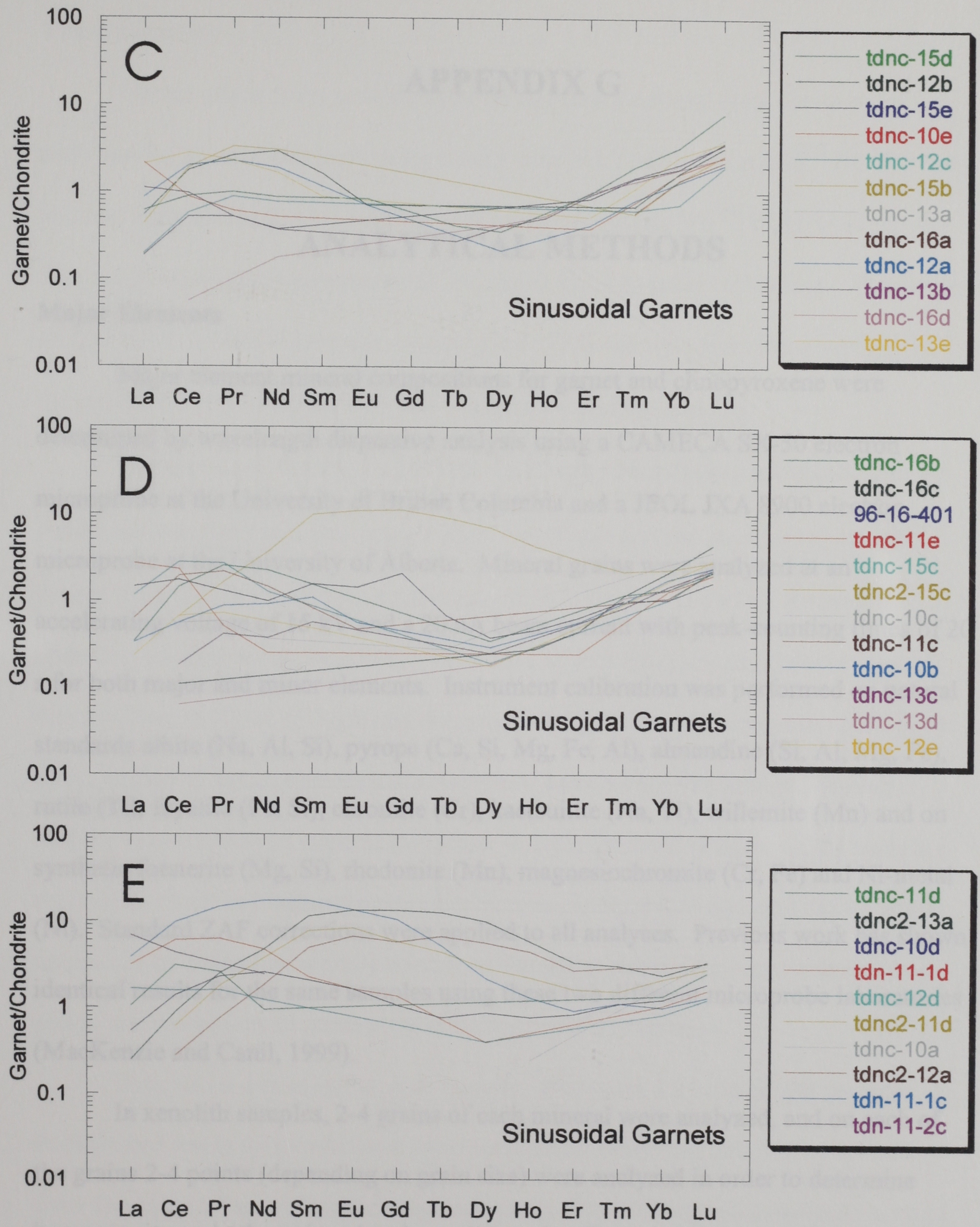
C
Garnet/Chondrite
100
10
1
0.1
0.01
Sinusoidal Garnets
tdnc-15d
tdnc-12b
tdnc-15e
tdnc-10e
tdnc-12c
tdnc-15b
tdnc-13a
tdnc-16a
tdnc-12a
tdnc-13b
tdnc-16d
tdnc-13e
La Ce Pr Nd Sm Eu Gd Tb Dy Ho Er Tm Yb Lu
D
Garnet/Chondrite
100
10
1
0.1
0.01
Sinusoidal Garnets
tdnc-16b
tdnc-16c
96-16-401
tdnc-11e
tdnc-15c
tdnc2-15c
tdnc-10c
tdnc-11c
tdnc-10b
tdnc-13c
tdnc-13d
tdnc-12e
La Ce Pr Nd Sm Eu Gd Tb Dy Ho Er Tm Yb Lu
E
Garnet/Chondrite
100
10
1
0.1
0.01
Sinusoidal Garnets
tdnc-11d
tdnc2-13a
tdnc-10d
tdn-11-1d
tdnc-12d
tdnc2-11d
tdnc-10a
tdnc2-12a
tdn-11-1c
tdn-11-2c
La Ce Pr Nd Sm Eu Gd Tb Dy Ho Er Tm Yb Lu

APPENDIX G

ANALYTICAL METHODS

Major Elements

Major element mineral compositions for garnet and clinopyroxene were determined by wavelength dispersive analysis using a CAMECA SX-50 electron microprobe at the University of British Columbia and a JEOL JXA 8900 electron microprobe at the University of Alberta. Mineral grains were analyzed at an accelerating voltage of 15 kV and a 20 nA beam current with peak-counting times of 20 s for both major and minor elements. Instrument calibration was performed on natural standards albite (Na, Al, Si), pyrope (Ca, Si, Mg, Fe, Al), almandine (Si, Al, Mg, Fe), rutile (Ti), fayalite (Fe, Si), chromite (Cr), kaersuitite (Na, Ti), willemite (Mn) and on synthetic forsterite (Mg, Si), rhodonite (Mn), magnesiochromite (Cr, Fe) and Ni-metal (Ni). Standard ZAF corrections were applied to all analyses. Previous work has shown identical results for the same samples using these two different microprobe laboratories (MacKenzie and Canil, 1999).

In xenolith samples, 2-4 grains of each mineral were analyzed, and on each of the grains 2-4 points (depending on grain size) were analyzed in order to determine homogeneity on both a mineral and xenolith scale. The mineral compositions in Appendix C are averages since all garnets showed no sign of heterogeneity.

Trace Elements

Garnet grains from xenolith samples and heavy mineral concentrate were analyzed for 25 trace elements using a solid state Nd:YAG Merchantek™ EO UV laser ablation microprobe (LAM) coupled with a high sensitivity VG™ PQII S inductively coupled plasma mass spectrometer (ICP-MS) at the University of Victoria. The output of the Nd:YAG laser is frequency quadrupled to 266 nm with a maximum energy of 4 mJ and is operated in a gated Q-switch mode for optimum stability.

The laser spot size can range from 5-300 μm under computer control. During garnet analysis laser spot size ranged from 70-100 μm and the laser power output ranged from 0.75-2.19 mJ with a pulse rate of 10.0 Hz (see Table G.1 for typical operating conditions for the LAM). Variations in spot size and output power were dependent upon signal strength and the condition of the sample being analyzed. Several of the garnets in both xenoliths and concentrate have a very fractured appearance, making the condition of some of the grains variable for laser analysis. If the sample is sufficiently thick and without numerous fractures, a larger spot size and higher power output can be utilized in order to maximize the signal output since spot size and laser power are two important parameters affecting limits of detection.

Data was acquired in the peak-jumping mode over a period of 120 seconds. Background levels for all elements were obtained by collecting data for a gas blank from the initial 60 seconds before laser sampling. Since the samples analyzed were in epoxy mounts, the grains were usually of sufficient thickness to avoid burning through, and a lengthy signal could be recorded because of the amount of time allowed for

Table G.1. Typical operating conditions of LAM-ICP-MS for analysis of garnet and clinopyroxene.

LAM

Laser	UV 266nm frequency quadrupled Nd:YAG
Mode	Q-Switched
Flash Lamp Frequency	20 Hz
Laser Output Frequency	10 Hz
Spot Size	3-5 (70-100 μm)
Laser Output Power	0.75-2.19 mJ

ICP-MS

Plasma

Plasma Gas	Argon
RF Power	1.53 kW forward, <5 W reflection

Gas Flow

Plasma Gas Flow Rate	14 dm^3min^{-1}
Auxiliary Gas Flow Rate	0.94 dm^3min^{-1}
Inner Gas Flow Rate	~ 1.20 dm^3min^{-1}

Interface

Sampling Distance	16 mm
Sampling Aperture	Ni 1.0 mm diameter
Skimmer Aperture	Ni 0.7 mm diameter

Ion Lens Settings

Extraction Lens	-365 V
Collector Lens	-77.9 V
L1 Lens	+2.8 V
L2 Lens	-10.7 V
L3 Lens	+4.8 V
L4 Lens	-29.9 V
Pole Bias	0 V

Acquisition Parameters

Ion Detection	pulse counting
Scanning Mode	peak jumping, 1 point/peak
Dwell Time	10.24 ms
Data Acquisition Time	120 s (maximum)

counting with the laser on (60 seconds). Some samples, however, were quickly burned through in 10-20 seconds because of thickness or grain fractures, and these were usually re-analyzed on a different spot on the same grain if possible. The Sr counts as a function of time were used to indicate the state of the sample during laser ablation. The Sr value in an invading matrix, such as carbonate or kimberlite, is much higher than in garnet (Sweeney et al, 1995), and therefore Sr spikes in the data were used to determine when a grain was burned through or a crack encountered (Figure G.1).

Detection limits for each sample run are of utmost importance since most elements being analyzed for occur in only trace quantities. Detection limits or Limit of Detection (LOD) is defined as three times the standard deviation of the Ar gas blank (background level) element concentrations (Longerich et al, 1996). This can be calculated using the following equation:

$$LOD = 3\sigma\,(1/N_a + 1/N_b)^{1/2}$$

where σ is the standard deviation, and N_a and N_b are the number of slices in the ablation time that are integrated for background and signal intensity, respectively. Detection limits for several sample runs for NIST 613 are included in Table G.2, and are plotted in Figure G.2.

NIST 613 synthetic silicate glass was used as an external calibration standard, and this glass was replicated on every run of the LAM-ICP-MS analysis (4 points out of 20 points per sample run). The concentration of Ni in the garnet samples is the most critical of the trace elements studied since much of the interpretation depends on Ni-in-garnet geothermometry. Therefore accurate Ni concentrations for the samples using the

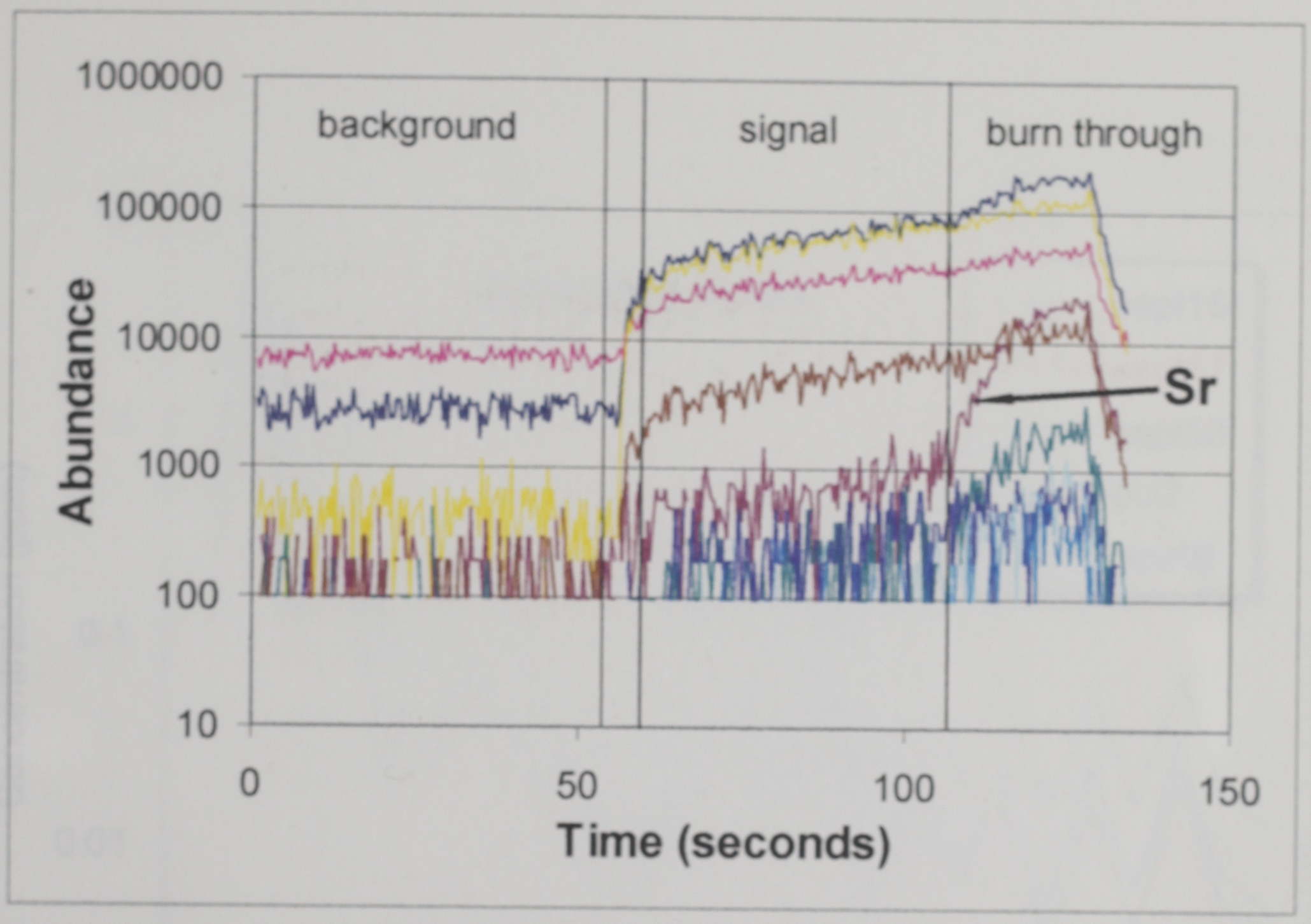

Figure G1. Sample output of element abundance against time from LAM ICP-MS. Background levels are collected for 60 seconds before the laser is fired and sample data is collected. Strontium (Sr) is useful for indicating when a sample has been penetrated, or a fracture encountered in the grain.

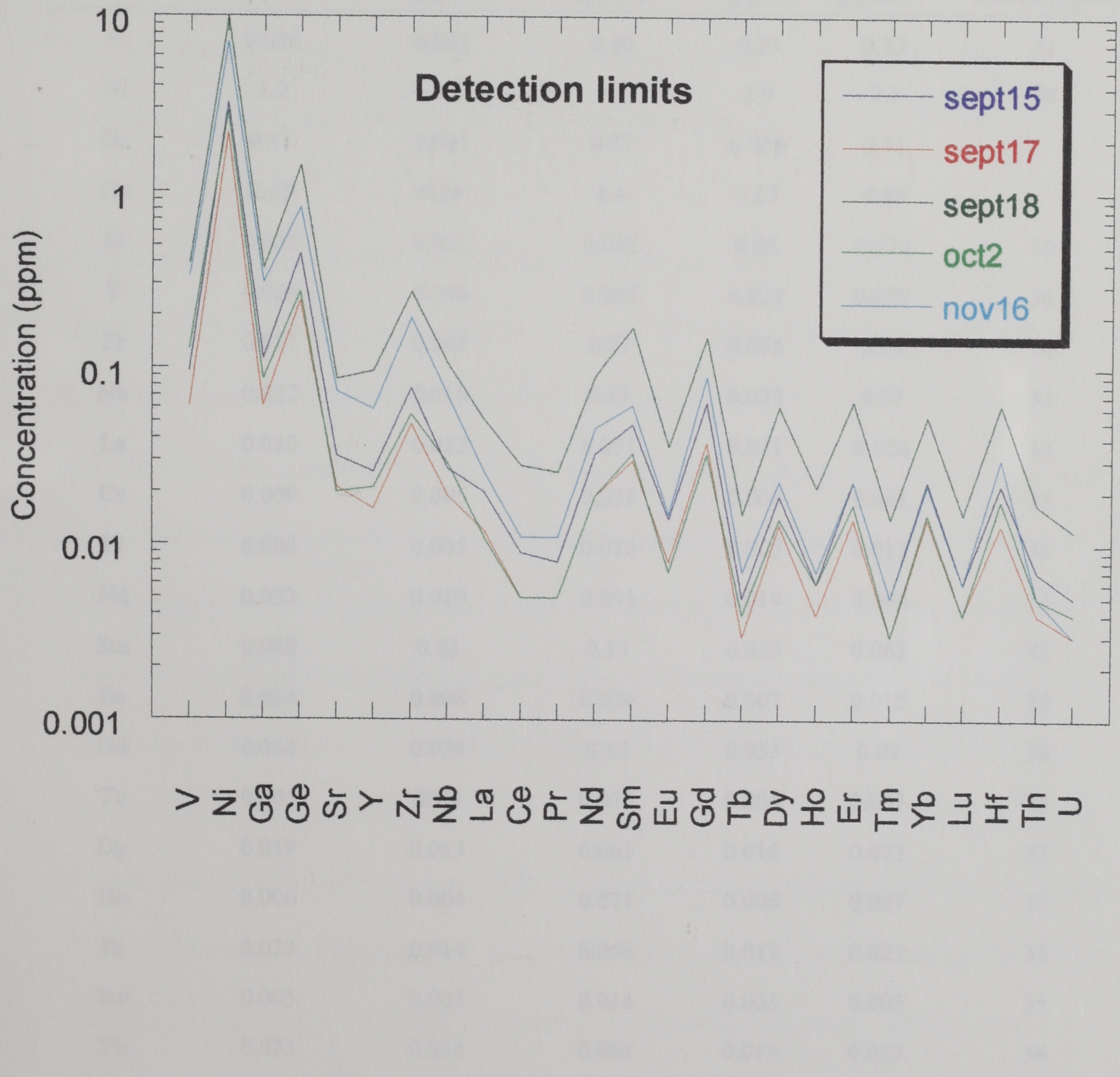

Figure G.2. Plot of detection limits for the LAM-ICP-MS on NIST 613 glass over five different sample runs. Detection limits vary for each sample run; high detection limits (i.e. high background levels) for Ni are seen because of the Ni cones used in the ICP-MS.

Table G.2. Typical detection limits for five different sample runs over a two month period for the NIST 613 glass standard. Also included are literature values for the NIST 613 after Longerich et al, 1996.

Element	Sept 15 (ppm)	Sept 17 (ppm)	Sept 18 (ppm)	Oct 2 (ppm)	Nov 16 (ppm)	Literature Value (ppm)
V	0.096	0.061	0.40	0.13	0.33	31
Ni	3.2	2.2	9.7	2.9	7.1	38
Ga	0.11	0.061	0.37	0.086	0.31	
Ge	0.45	0.24	1.4	0.27	0.82	
Sr	0.032	0.021	0.087	0.02	0.074	70
Y	0.026	0.016	0.097	0.021	0.059	36
Zr	0.077	0.048	0.27	0.055	0.19	38
Nb	0.027	0.019	0.11	0.029	0.07	33
La	0.020	0.012	0.051	0.011	0.026	33
Ce	0.009	0.005	0.028	0.005	0.011	35
Pr	0.008	0.005	0.026	0.005	0.011	35
Nd	0.033	0.019	0.091	0.019	0.046	33
Sm	0.048	0.03	0.17	0.033	0.062	35
Eu	0.014	0.008	0.036	0.007	0.015	33
Gd	0.064	0.038	0.15	0.033	0.09	36
Tb	0.005	0003	0.015	0.004	0.007	35
Dy	0.019	0.013	0.061	0.014	0.023	33
Ho	0.006	0.004	0.021	0.006	0.007	35
Er	0.023	0.014	0.066	0.017	0.023	35
Tm	0.005	0.003	0.014	0.003	0.005	35
Yb	0.023	0.014	0.054	0.015	0.022	36
Lu	0.006	0.004	0.015	0.004	0.006	34
Hf	0.022	0.013	0.063	0.018	0.031	35
Th	0.007	0.004	0.017	0.005	0.005	34
U	0.005	0.003	0.012	0.004	0.003	33

LAM-ICP-Ms are imperative. Measured values of Ni in the NIST 613 synthetic silicate glass were always within 5% of the known glass values for Ni, providing good precision and accuracy (Figure G.3). As well, a garnet sample with known Ni values from proton microprobe analysis (Sample 21-6, Kopylova et al, 1999) was used as an external check and analyzed for Ni on several occasions giving results within 10% of the known value (Figure G.2), showing further accuracy of the LAM-ICP-MS for Ni in garnet.

Furthermore, in order to demonstrate reproducibility over time for each sample run Figure G.4 shows the known values for the NIST 613 glass (Chen et al, 1997) plotted along with measured values for eight different sample runs. With the exception of V and Nb, all of the measured values for the trace elements analyzed are within a 10% of the Proton Microprobe values, with consistent results throughout the runs. Similar results have been produced on other work with the LAM-ICP-MS at the University of Victoria where differences between measured and literature values are less than 4% for most trace elements and 12.3%, 7.4%, 11.7% and 6.5% for V, Zr, Nb and Gd respectively (Chen, pers. comm.).

In order to correct for drift, matrix effect, changes in laser sampling yield and transport efficiency during the analysis, a naturally occurring major element is used as an internal standard. In this study Ca is used as an internal standard because its fractionation behaviour is similar to those of most of the analytes. Ca values were input from average values previously derived from the major element analysis on the EMP (CaO oxide wt%).

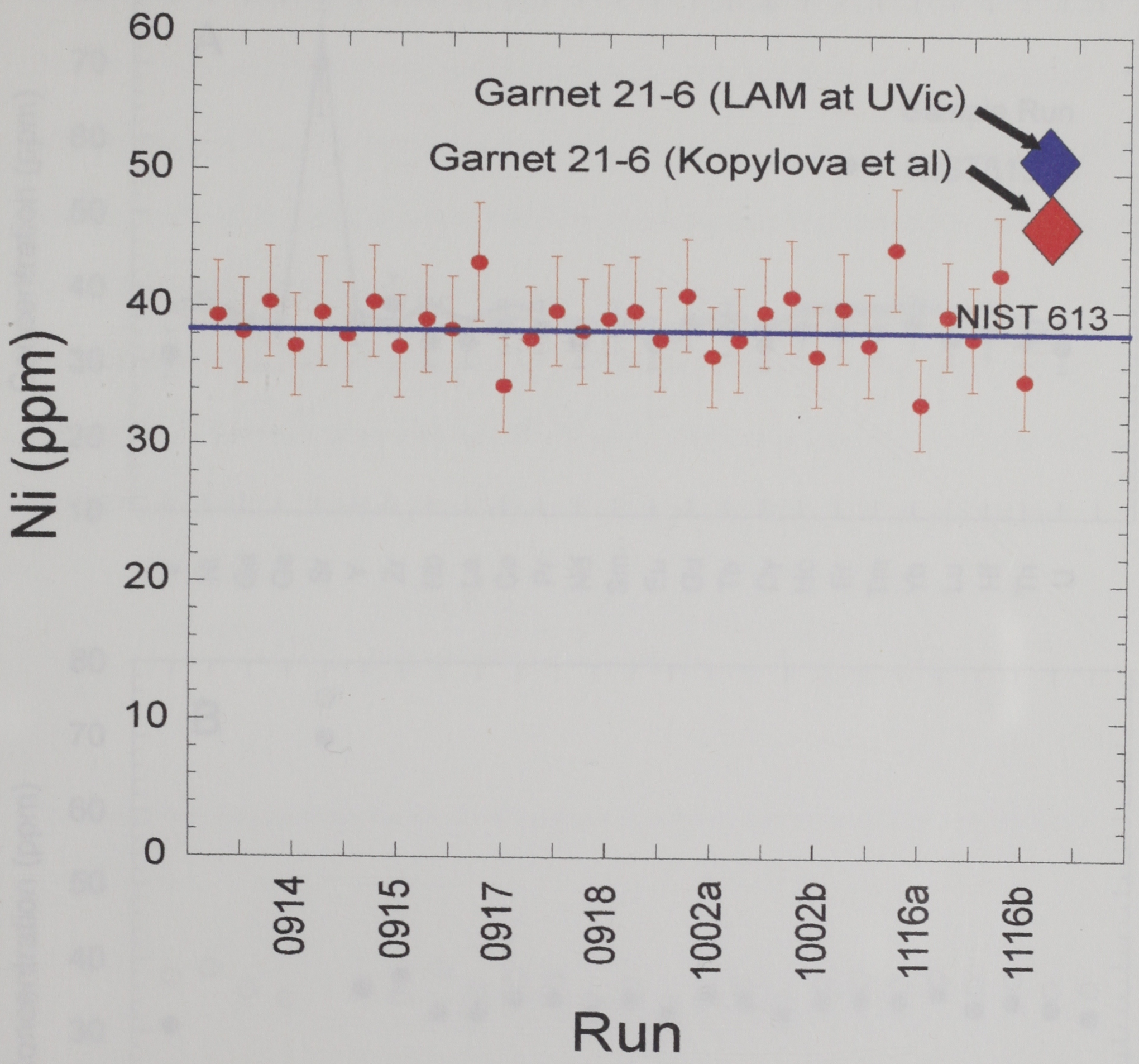

Figure G.3. Plot of Ni concentration against individual sample runs over a period of three months. The blue line is the known value for the glass standard NIST 613, and LAM values for the same glass standard collected twice per sample run are indicated in red. The LAM values for the glass show good precision for the sample runs. Also shown is a garnet sample (Kopylova et al, 1999) which was analyzed elsewhere and the results compared to the LAM facility at the University of Victoria. The results indicate good accuracy with known results for the outside standard as well.

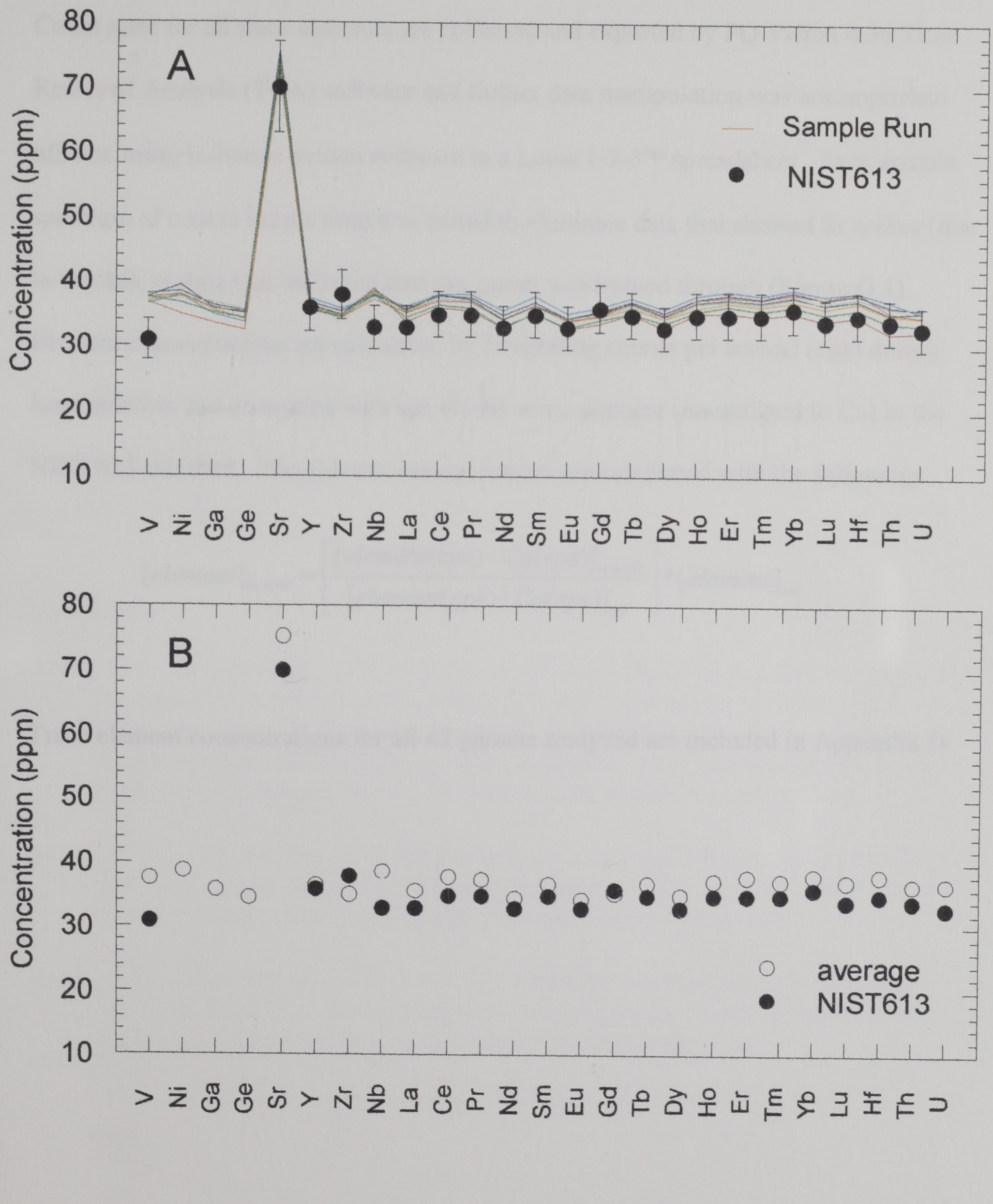

Figure G.4. Element concentrations measured for NIST 613 glass standard over eight sample runs using the LAM-ICP-MS. Plot **A** gives literature values for NIST 613 from *Chen et al, 1997* plotted against measured values for each run. Measured values are within 10% relative error (vertical bars) of the known values with the exception of V and Nb. Plot **B** shows known NIST 613 values against the average concentrations over all runs of the study.

Count rates for all trace elements are collected and exported by PQ Vision 4.36 Time Resolved Analysis (TRA) software and further data manipulation was accomplished off-line using in-house written software in a Lotus 1-2-3™ spreadsheet. Each sample spectrum of counts versus time was edited to eliminate data that showed Sr spikes (due to cracks), or data that indicated that the garnet was burned through (Figure G.1).

Element concentrations are calculated by integrating counts per second (cps) during laser ablation and compared with cps for the same element (normalized to Ca) in the NIST 613 standard. The element concentrations are calculated with the following:

$$[element]_{sample} = \left[\frac{[element(cps) / Ca(cps)]_{sample}}{[element(cps) / Ca(cps)]_{std}} \right] * [element]_{std}$$

Trace element concentrations for all 42 garnets analyzed are included in Appendix D.

VITA

Surname: Carbno **Given Names**: Gary Brent

Place of Birth: Mississauga, Ontario, Canada

Educational Institutions Attended:

Carleton University, Ottawa, Ontario	1990-1993
Concordia University, Montreal, Quebec	1994-1997
University of Victoria, Victoria, British Columbia	1997-2000

Degrees Awarded:

B.Sc. (With Distinction)	Concordia University	1997

Publications:

Carbno, G.B., and Canil, D., 1999, Mantle garnets from the Drybones Bay kimberlite and the nature of the on/off craton transition beneath the Slave Province, NWT. In: F Cook and P Erdmer (compilers), Slave - Northern Cordillera Lithospheric Evolution (SNORCLE) Transect and Cordilleran Tectonics Workshop Meeting (University of Calgary, 1999), LITHOPROBE Report No. 69, p 48-51.

Carbno, G.B., and Canil, D., 1999, Mantle garnets from the Drybones Bay kimberlite and the on/off craton transition of the Slave Province, NWT. In: GAC/MAC Joint Annual Meeting, Sudbury, Ontario, Abstract Volume 24, p 19-20.

Carbno, G.B., and Canil, D., 2000, Mantle Stratigraphy beneath the southwest Slave Province, Canada: Constraints from garnet geochemistry in the Drybones Bay kimberlite: Journal of Geophysical Research, submitted.

PARTIAL COPYRIGHT LICENSE

I hereby grant the right to lend my thesis to users of the University of Victoria Library, and to make single copies only for users or in response to a request from the library of another university, or similar institution, on its behalf or for one of its users. I further agree that permission for extensive copying of this thesis for scholarly purposes may be granted by me or a member of the University designated by me. It is understood that copying or publication of this thesis for financial gain shall not be allowed without my written permission.

Title of Thesis:

Geochemical and Petrological Interpretation of Mantle Structure Beneath the Southwest Slave Province, NWT

Author _____

Gary Brent Carbno

February 17, 2000